Bipropellant Engine Plume Contamination Program

Volume II
Chamber Measurements — Phase II

H. M. Powell, L. L. Price, and R. E. Alt
ARO, Inc.

November 1979

Final Report for Period September 25 — October 20, 1978

Approved for public release; distribution unlimited.

ARNOLD ENGINEERING DEVELOPMENT CENTER
ARNOLD AIR FORCE STATION, TENNESSEE
AIR FORCE SYSTEMS COMMAND
UNITED STATES AIR FORCE

NOTICES

When U. S. Government drawings, specifications, or other data are used for any purpose other than a definitely related Government procurement operation, the Government thereby incurs no responsibility nor any obligation whatsoever, and the fact that the Government may have formulated, furnished, or in any way supplied the said drawings, specifications, or other data, is not to be regarded by implication or otherwise, or in any manner licensing the holder or any other person or corporation, or conveying any rights or permission to manufacture, use, or sell any patented invention that may in any way be related thereto.

Qualified users may obtain copies of this report from the Defense Documentation Center.

References to named commerical products in this report are not to be considered in any sense as an indorsement of the product by the United States Air Force or the Government.

This report has been reviewed by the Information Office (OI) and is releasable to the National Technical Information Service (NTIS). At NTIS, it will be available to the general public; including foreign nations.

APPROVAL STATEMENT

This report has been reviewed and approved.

Larry F. Bowers

LARRY F. BOWERS, Captain, USAF
Test Director, VKF Division
Directorate of Test Operations

Approval for publication:

FOR THE COMMANDER

James D Sanders

JAMES D. SANDERS, Colonel, USAF
Deputy for Operations

REPORT DOCUMENTATION PAGE		READ INSTRUCTIONS BEFORE COMPLETING FORM
1 REPORT NUMBER AEDC-TR-79-28 Volume II	2 GOVT ACCESSION NO.	3 RECIPIENT'S CATALOG NUMBER
4 TITLE (and Subtitle) BIPROPELLANT ENGINE PLUME CONTAMINATION PROGRAM - VOLUME II CHAMBER MEASUREMENTS - PHASE II		5 TYPE OF REPORT & PERIOD COVERED Final Report - Sept 25 - Oct 20, 1978 6 PERFORMING ORG. REPORT NUMBER
7. AUTHOR(s) H. M. Powell, L. L. Price, and R. E. Alt, ARO, Inc., a Sverdrup Corporation Company		8 CONTRACT OR GRANT NUMBER(s)
9 PERFORMING ORGANIZATION NAME AND ADDRESS Arnold Engineering Development Center/DOOV Air Force Systems Command Arnold Air Force Station, Tennessee 37389		10 PROGRAM ELEMENT, PROJECT, TASK AREA & WORK UNIT NUMBERS Program Element 62302F/ 63411F
11 CONTROLLING OFFICE NAME AND ADDRESS Air Force Rocket Propulsion Laboratory/PACP Edwards Air Force Base, California 93523		12. REPORT DATE November 1979 13 NUMBER OF PAGES 113
14 MONITORING AGENCY NAME & ADDRESS(if different from Controlling Office)		15 SECURITY CLASS (of this report) UNCLASSIFIED 15a DECLASSIFICATION/DOWNGRADING SCHEDULE N/A
16 DISTRIBUTION STATEMENT (of this Report) Approved for public release; distribution unlimited.		
17 DISTRIBUTION STATEMENT (of the abstract entered in Block 20, if different from Report)		
18 SUPPLEMENTARY NOTES		
19 KEY WORDS (Continue on reverse side if necessary and identify by block number) rocket engines electron beams contamination plumes density (number) temperature (rotational) scattering (laser) flow visualization bipropellants		
20 ABSTRACT (Continue on reverse side if necessary and identify by block number) A bipropellant rocket engine plume contamination test program was conducted in the AEDC Aerospace Chamber (10V). A 5-lbf-thrust rocket engine, burning MMH as the fuel and N_2O_4 as the oxidizer, was operated over a range of engine operating parameters in a cryogenically pumped vacuum chamber where the background pressure was maintained below 1×10^{-5} torr. Using the electron beam		

DD FORM 1 JAN 73 1473 EDITION OF 1 NOV 65 IS OBSOLETE

20. ABSTRACT (Continued)

fluorescence technique, species number densities and rotational temperature were measured in both the forward- and back-flow regions of the plume exhaust. Additionally, Mie scattering measurements were performed for the forward-flow region of the plume exhaust.

AFSC
Arnold AFS Tenn

PREFACE

The work reported herein was conducted by the Arnold Engineering Development Center (AEDC), Air Force Systems Command (AFSC), for the Air Force Rocket Propulsion Laboratory (AFRPL/PACP), AFSC. The results of the tests were obtained by ARO, Inc., AEDC Division (a Sverdrup Corporation Company), operating contractor for the AEDC, AFSC, Arnold Air Force Station, Tennessee, under ARO Project No. V41Q-68. The AFRPL project monitor was Lt. Eric Lund, and Dr. H. E. Scott was the AEDC project manager. The data analysis was completed on May 25, 1979, and the manuscript was submitted for publication on June 18, 1979.

Additional authors and participants in the measurements include J. H. Jones, R. L. McGuire, J. W. L. Lewis, and B. P. Curry.

CONTENTS

ILLUSTRATIONS

Figure

Figure | Page

Figure | Page

Figure — Page

1.0 INTRODUCTION

The exhaust plume of a rocket engine operating at high altitude exhibits a complicated angular distribution of the flux of both gaseous and particulate plume constituents. The mass flux of the plume exhaust which is issued from the engine at large angles with respect to the flow centerline represents, potentially, a serious contamination problem for a variety of spacecraft systems. Unlike the inviscid, central core flow of the plume, the capability of prediction of the mass flux for large angles and back-flow regions (with respect to the flow centerline) is poor. The source of this difficulty of prediction varies with the type of engine as well as its operating conditions and nozzle characteristics. For example, the large exit area ratio nozzles can be expected to possess a significant boundary layer which can expand, because of an increased Prandtl-Mayer angle, into the back-flow region of the engine. Also, such a phenomenon will be modified depending on whether film cooling is used for the nozzle. Because of the computational uncertainty in predicting the exhaust plumes of rocket engines, a series of experimental studies was initiated by the Air Force Rocket Propulsion Laboratory (AFRPL) which had the primary goals of evaluating the distribution of the mass flux of the plume exhaust and the determination of the flow field, including the nozzle exit plane's species densities and temperatures.

The culmination of the most recent AFRPL series of experimental studies of plume contamination effects included measurements of the simulated high-altitude plumes of both monopropellant hydrazine (Refs. 1 and 2) and bipropellant thruster engines (Ref. 3). The work presented in this report describes the diagnostic measurement techniques used for the gaseous species densities and temperatures in both the forward and back-flow regions of a 5-lbf-(22 N)-thrust liquid bipropellant rocket engine. This is the same engine for which the mass flux measurements of Ref. 3 were made. Representative results of gaseous species density and temperature are presented. Additionally, laser Mie scattering was employed to monitor the temporal and spatial characteristics of particulate matter ejected from the engine, and measurement techniques and typical results are reported.

2.0 THEORY

2.1 ELECTRON BEAM EXCITATION

The interaction of a high-energy beam of electrons with atomic and molecular species produces excited neutral and ionized species, along the path of the electron beam, which subsequently fluoresce. The wavelengths of these fluorescent spectra are characteristic of the excited molecular species, and the fluorescent intensity of the individual spectral features is proportional to the number density of the species at the observed region of fluorescence.

Since the theoretical description of this technique has been presented in previous publications (Refs. 4 through 9), only a summary of the necessary equations will be given.

2.1.1 Number Density

For a gas mixture subjected to excitation by an electron beam of energy E_B and current I the photon emission rate S_α (ij) for the i→j transition of species α and for a length L of the cylindrical beam is (Ref. 4)

$$S_\alpha(ij)/I = \left(\frac{\Delta\Omega}{4\pi}\right) \cdot \frac{L\,C\left[\lambda_\alpha(ij)\right]\beta_\alpha(ij)\left[\sigma_\alpha(gi) - \sum_t \sigma_\alpha(gt)\,\beta_\alpha(ti)\right] n_\alpha(g)}{\left[1 + \sum_\mu k_{\alpha\mu}(i)\,\tau_\alpha(i)\,n_\mu(g)\right]} \tag{1}$$

where

σ_α (gi) = cross section of excitation from ground state g to excited state i

β_α (ti) = branching factor for the t→i transition of species α

n_α (g) = number density of ground state g of species α

and

τ_α (i) = lifetime of excited state i of species α

The wavelength for the i→j transition of species α is λ_α (ij) and the solid angle subtended by the detector at the point of observation is $\Delta\Omega$; C[λ_α (ij)] includes all wavelength-dependent transmission and detection processes. Further, $k_{\alpha\mu}$ (i) denotes the quenching rate coefficient of level i of species α as a result of collisions with species μ. The second term of the numerator of Eq. (1) accounts for radiative cascading effects and the denominator represents collisional quenching processes which reduce the intermolecular collision-free photon emission rate. Finally, collisional quenching of the cascading levels has been neglected.

Assuming that the radiative transitions have been selected to preclude cascading transitions and the total gas density is sufficiently low that collisional quenching is negligible, Eq. (1) becomes

$$S^o_\alpha(ij)/I = (\Delta\Omega/4\pi)\,L\,C\left[\lambda_\alpha(ij)\right]\beta_\alpha(ij)\,\sigma_\alpha(gi)\,n_\alpha(g) \tag{2}$$

In this limiting case S^o_α (ij)/I is directly proportional to the number density n_α (g). Consequently, with the aid of an in situ calibration, the local number density of each species of the gas mixture can be determined.

The existence of moderate collisional quenching effects is not contraindicatory for the use of electron beam diagnostics, but the sensitivity and accuracy of the technique decreases in this higher density regime. A further reduction of the sensitivity of the technique to collisional quenching effects is afforded by the use of the ratios of fluorescence signals

$$S_\alpha(ij)/S_\delta(kl) = \left\{ C\left[\lambda_\alpha(ij)\right] \Big/ C\left[\lambda_\delta(kl)\right] \right\} \times \left[\beta_\alpha(ij)\,\sigma_\alpha(gi) \Big/ \beta_\delta(kl)\,\sigma_\delta(gk)\right]$$

$$\times \left[n_\alpha(g)/n_\delta(g)\right] \times \left\{ \left[1 + \sum_\eta \bar{k}_{\delta\eta}(k)\,\tau_\delta(k)\,n_\eta(g)\right] \Big/ \left[1 + \sum_\mu k_{\alpha\mu}(i)\,\tau_\alpha(i)\,n_\mu(g)\right] \right\} \quad (3)$$

Consequently, even when significant quenching corrections are required for Eq. (1), if the quenching correction factors for the i^{th} and k^{th} levels of species α and δ, respectively, are approximately equal, Eq. (3) shows that $S_\alpha(ij)/S_\delta(kl)$ can provide a reasonable measure of the number density ratio $n_\alpha(g)/n_\delta(g)$.

Regarding the order of magnitude of the quenching correction, it should be noted that the species of interest are electronically excited neutral or ionic atoms and molecules, and the quenching cross sections can be comparable to or larger than gas kinetic cross sections (Refs. 8 and 10). Therefore, assuming typical gas kinetic rate coefficient values

$$k_{\alpha\mu}(i) \simeq 10^{-10} \text{ cc/sec/molecule and a typical lifetime } \tau_\alpha(i)$$

value of 10^{-7} sec,

$$\sum_\mu k_{\alpha\mu}(i)\,\tau_\alpha(i)\,n_\mu(g) \sim 10^{-17} \sum_\mu n_\mu(g) = 10^{-17}\,n_T,$$

where n_T is total number density.

Therefore, the quenching correction for Eq. (1) is on the order of ten percent if $n_T = 10^{16}$ cc^{-1} and approximately 30 percent at $n_T = 3 \times 10^{16}$ cc^{-1}, which corresponds to a pressure of approximately 1 torr at 300°K.

For gas mixtures containing H_2 and hydrogenous molecules, such as H_2O, the strongest visible fluorescence signals arise from the atomic hydrogen Balmer series produced by the excitation and emission reactions

$$H_2 + e^- \xrightarrow{\sigma} H^* + H + e^-$$

$$H_2O + e^- \xrightarrow{\sigma'} H^* + OH + e^-$$

$$H^+ = H(n\ell) \longrightarrow H(n',\ell'\pm1) + h\nu, \quad (4)$$

where n and ℓ represent the principal and orbital angular momentum quantum numbers, respectively, for the Balmer series $n' = 2$. Consequently, the photon emission rate for the transition $(n,\ell) = (2,\ell \pm 1)$ is given by

$$S(ij)/I = (\Delta\Omega/4\pi)\, L\, C \left[\lambda(ij)\right] \beta(ij) \left[\sigma_{H_2}(gi)\, n_{H_2}(g) + \sigma_{H_2O}(gi)\, n_{H_2O}(g)\right] \times \left[1 + \sum_{\mu} \bar{k}_{H,\mu}(i)\, r_H(i)\, n_\mu(g)\right]^{-1} \quad (5)$$

Unfortunately, accurate values of σ_{H_2} and σ_{H_2O} are not known for this energy range ($E_B \cong$ 30 - 40 keV). At best, one can only assume that chemical binding effects are not dominant effects in determining the excitation cross sections σ_{H_2} and σ_{H_2O}. The results presented in Ref. 7 for atomic nitrogen fluorescence produced by dissociative excitation of N_2 and NO give support to this assumption. Therefore, Eq. (5) is approximated by

$$S(ij)/I \simeq (\Delta\Omega/4\pi)\, L\, C \left[\lambda(ij)\right] \beta(ij)\, \sigma_{H_2}(gi) \frac{n_{H_2}(g) + n_{H_2O}(g)}{\left[1 + \sum_{\mu} \bar{k}_{H,\mu}(i)\, r_H(i)\, n_\mu(g)\right]} \quad (6)$$

so that the H Balmer line observed for the mixture containing H_2 and H_2O is an approximate measure of the sum of n_{H_2} and n_{H_2O}.

2.1.2 Rotational Temperature

Nitrogen rotational temperatures have been measured successfully at the Arnold Engineering Development Center (AEDC) in a variety of flows through the use of electron beam excitation. They have been determined in wind tunnel, hypersonic nozzle, and sonic orifice expansion flow fields (Refs. 11 through 14) and, most recently, in a monopropellant thruster exhaust (Ref. 1). The following electron-molecule impact occurs in which the nitrogen molecule is both ionized and electronically excited:

$$e^-_{py} + N_2\left(X^1\Sigma\right) \longrightarrow N_2^+\left(B^2\Sigma\right) + e^-_{py} + e^-_{sy} \quad (7)$$

where e^-_{py} are primary electrons and e^-_{sy} are secondary electrons, and emission is then from the decay

$$N_2^+\left(B^2\Sigma\right) \longrightarrow N_2^+\left(X^2\Sigma\right) + h\nu \text{ (First Negative System)} \quad (8)$$

Evidence is that the above excitation-emission process is direct. The energy of each photon of the First Negative System is determined by the particular initial and final rotational and vibrational energy levels of occupation. With the existence of an equilibrium, or Boltzmann, distribution of initial rotational states of the ambient nitrogen molecules a rotational temperature may be defined, and the spectral distribution of emitted radiation in a vibrational band of the relatively bright First Negative System is directly related to that temperature. The intense (0,0) and (0,1) bands appearing at approximately 3900 Å and 4270 Å, respectively, are the most commonly used. Each band is characterized by a P and an R branch which are spectrally separate under moderate resolution and at temperatures less than about 400°K. For a given resolution, the shape of each band profile is a unique function of the rotational temperature. Usually, one of two degrees of resolution is used. Under moderate resolution, all R branch lines, which are in reality closely spaced doublets, are spectrally resolved. A measurement of each line's integrated intensity or its peak height is then made, following which rotational temperature is calculated from the slope of a least squares fit to a Boltzmann plot. Under low resolution in which no lines are resolved, the ratio of intensities at two wavelengths, usually within the R branch, is formed. These two wavelengths are so chosen as to make the ratio a single-valued function of rotational temperature. At AEDC, computer programs TROT (Ref. 15) and VIBTEMP have been developed for the analyses of these resolved and unresolved spectra.

2.2 LASER MIE SCATTERING

The use of Mie scattering for studies of particulate properties such as particulate size and number density, is well established (Refs. 16 through 19). This technique is based on the fact that an incident beam of radiation is scattered to a degree determined by the particle size, its complex index of refraction, the number density of the scatterers as well as the shape of the scatterer, and the angle of observation. Shown in Fig. 1 is a representation of a spherical particle of diameter D and index of refraction η located at the origin of the coordinate system which scatters radiation from the incident beam of radiation of flux Φ_o, wavelength λ, and cross-sectional area A. The incident beam is along the + Z axis, and the scattered radiation at the spherical polar angle θ and azimuthal angle ϕ is shown. The differential cross section $d\sigma/d\Omega$ for this scattering process is given by

$$d\sigma/d\Omega = i_{1,2}(x, \theta, \eta)\left(\sin^2\phi;\ \cos^2\phi\right)\Big/K^2 \tag{9}$$

where the size parameter $x = 2\pi D/\lambda$ and the magnitude of the propagation vector $|\vec{K}| = K$ is given by $2\pi/\lambda$. The Mie scattering functions $i_{1,2}(x,\theta,\eta)$ (Ref. 20) for polarization perpendicular to and parallel to the scattering plane are denoted by the subscripts 1 and 2, respectively, and the ordering of the quantities within the parentheses corresponds to 1 and 2, respectively. The energy flux Φ_o which is scattered at (θ,ϕ) is given by

$$\Phi_{1,2}(\theta,\phi)/\Phi_o = \left(nL/K^2\right) \int_{\phi-\frac{\Delta\phi}{2}}^{\phi+\frac{\Delta\phi}{2}} \int_{\theta-\frac{\Delta\theta}{2}}^{\theta+\frac{\Delta\theta}{2}} i_{1,2}(x,\theta,\eta)\left(\sin^2\phi;\ \cos^2\phi\right) d\Omega \tag{10}$$

where n is the number density of scatterers, L is the length of the observed beam and $d\Omega = \sin\theta\, d\theta\, d\phi$, the solid angle subtended at the scattering volume by the elemental area of the detector. The integration limits are determined, of course, by the measure of the total solid angle subtended by the detector.

Consider the following definitions for Mie scattering functions integrated over the detector subtended angles:

$$\langle i_{1,2}(x,\theta_i,\eta)\rangle \equiv \int_{\theta_i-\frac{\Delta\theta_i}{2}}^{\theta_i+\frac{\Delta\theta_i}{2}} i_{1,2}(x,\theta,\eta)\sin\theta\, d\theta \tag{11}$$

and

$$\langle \sin^2\phi_i\rangle, \langle\cos^2\phi_i\rangle \equiv \int_{\phi_i-\frac{\Delta\phi_i}{2}}^{\phi_i+\frac{\Delta\phi_i}{2}} \left(\sin^2\phi;\ \cos^2\phi\right)\frac{d\phi}{\Delta\phi} \tag{12}$$

For a particular set of detector coordinates, θ_i, ϕ_i, Eq. (10) can then be written as

$$\Phi_{1,2}\left(\theta_i,\phi_i\right)/\Phi_o = \left(nL/K^2\right)\left[\langle i_1\left(x,\theta_i,\eta\right)\rangle \langle\sin^2\phi_i\rangle \Delta\phi_i,\right.$$

$$\left.\langle i_2\left(x,\theta_i,\eta\right)\rangle \langle\cos^2\phi_i\rangle \Delta\phi_i\right] \tag{13}$$

The size dependence of the functions $\langle i_{1,2}(x,\theta_i,\eta)\rangle$ is shown in Figs. 2 and 3 for liquid droplets with refractive index n = 1.335 and $\theta_i = \pi/2$. The detector subtended angle $\Delta\theta_i$ is 0.04 radian and the solid angle is 1.36×10^{-3} steradian. The azimuth ϕ_i is π and the factors $\langle\sin^2\phi_i\rangle$ and $\langle\cos^2\phi_i\rangle$ are, respectively, 1.8×10^{-4} and 0.9998.

One can see that these factors effectively suppress the perpendicularly polarized scattering signal (in comparison with the parallel polarized signal) except at very small

particle sizes. As the Rayleigh scattering limit is approached, the parallel component decays much more rapidly than the perpendicular component; consequently, any experimental observation that the two polarization components are comparable is unambiguous evidence for the existence of very small droplets.

In order to make use of this fact, let us introduce the degree of polarization of the scattered signal

$$P\left(\theta_i,\phi_i\right) = \frac{\bar{\Phi}_1\left(\theta_i,\phi_i\right) - \bar{\Phi}_2\left(\theta_i,\phi_i\right)}{\bar{\Phi}_1\left(\theta_i,\phi_i\right) + \bar{\Phi}_2\left(\theta_i,\phi_i\right)} \tag{14}$$

where the bar over the functions $\Phi_{1,2}(\theta_i,\phi_i)$ indicates scattering by a polydisperse sample of particles characterized by a size distribution function f (x), subject to the constraint

$$\int_0^\infty f(x)\,dx = 1.0 \tag{15}$$

The polydisperse form of Eq. (13) is, thus,

$$\bar{\Phi}_{1,2}\left(\theta_i,\phi_i\right)\Big/\Phi_o = \left(nL/K^2\right)\int_0^\infty f(x)\left[<i_1\left(x,\theta_i,\eta\right)><\sin^2\phi_i>,\right.$$

$$\left.<i_2\left(x,\theta_i,\eta\right)><\cos^2\phi_i>\right]dx\,\Delta\phi_i \tag{16}$$

Equation (16) shows that measurements of $\bar{\Phi}_{1,2}(\theta_i,\phi_i)$ at a single scattering angle yields a result which is proportional to the number of scatterers per unit volume (n), but which is also dependent on f (x). Thus, single-angle, single-wavelength scattering cannot provide definitive measurements of either n or f (x). However, a weighted average size $\bar{x}$ can be determined by combining measurements of $\bar{\Phi}_{1,2}(\theta_i,\phi_i)$ as shown in Eq. (14).

The theoretical form of Eq.(14) is

$$P\left(\theta_i,\phi_i,\bar{x}\right) = \frac{<i_1\left(\bar{x},\theta_i,\eta\right)><\sin^2\phi_i> - <i_2\left(\bar{x},\theta_i,\eta\right)><\cos^2\phi_i>}{<i_1\left(\bar{x},\theta_i,\eta\right)><\sin^2\phi_i> + <i_2\left(\bar{x},\theta_i,\eta\right)><\cos^2\phi_i>} \tag{17}$$

3.0 APPARATUS

3.1 TEST UNIT - AEROSPACE CHAMBER (10V)

The Bipropellant Engine Plume Contamination Program was conducted in the AEDC Aerospace Chamber (10V). The chamber and its performance capability are described in general in Ref. 21 and in detail, as related to this test program, in Ref. 3. The chamber is designed for testing small rocket engines under space vacuum conditions. The stainless steel chamber is 10 ft in diameter and 20 ft long. The chamber is equipped with an internal cryogenic system designed for high efficiency vacuum pumping of rocket exhaust products.

The Chamber 10V pumpdown is accomplished with mechanical vacuum pumps and a 20-in. diffusion pump. The free expansion of the rocket plume is made possible by the high capture rate (pumping speed) of the exhaust gases on the chamber cryogenically cooled surfaces. The chamber cryogenic system consists of a liquid nitrogen (LN_2)-cooled (77°K) chamber liner, a radial finned gaseous helium (GHe)-cooled (20°K) cryopump, and a liquid helium (LHe)-cooled (4.2°K) cryopump. The chamber configuration for the program is shown in Fig. 4.

The rocket engine was located at the front of the chamber and was fired axially along the chamber horizontal centerline. The engine was installed in this position through an antechamber attached to the front of Chamber 10V. The rocket engine nozzle was positioned nominally about twelve inches in front of the antechamber valve. It was translated axially and vertically about this position in order to make the electron beam and laser diagnostics measurements. The engine was retracted into the antechamber during nonactive testing periods, while the chamber was at altitude, for ease of engine temperature control.

3.2 5-LBF-THRUST ENGINE AND PROPELLANT SYSTEM

The 5-lbf-thrust bipropellant engine was developed by the Aerojet Liquid Rocket Company. The engine is designed to operate on nitrogen tetroxide (N_2O_4) oxidizer and monomethylhydrazine (MMH) ($CH_3N_2H_3$) fuel at a mixture ratio of 1.6 with propellant supply temperatures between 20°F and 120°F. The designated baseline (BL) engine configuration for the Phase II Biprop Program was optimized for maximum performance with a pressure-regulated propellant feed system and an uninsulated thrust chamber (combustion chamber-nozzle) (Ref. 22). This engine incorporates a six-element splash plate injector (45-deg element orientation) and a 2-in.-long combustion chamber of cylindrical configuration with a 100:1 expansion ratio nozzle. This engine has no operating or duty

cycle limitations at combustion chamber pressures to 110 psia (4-lbf thrust) and will operate over a wide range of duty cycles at combustion chamber pressures up to 150 psia. During the engine development program (Ref. 22) the design goal specific impulse of 300 sec had been demonstrated for this engine configuration when operated in a steady-state mode. The Bipropellant Engine Specifications follow.

Thrust (vacuum), lbf	5-lbf thrust at P_c = 140 psia
Propellants, O/F	N_2O_4/MMH
Mixture Ratio, O/F	1.4 - 1.8 (1.6 design)
Chamber Length, in.	2.0
Chamber Pressure, psia	60 - 140
Area Throat, $in.^2$	0.0186
Nozzle Area Ratio, A_e/A_t	100:1, contoured
Injector	Six-Element Splash Plate (45 deg)
Propellant Flow Rate, lb/sec	0.0167 lb/sec (P_c = 150 psia)
Inlet Pressure Oxidizer, psia	100 - 300
Inlet Pressure Fuel, psia	100 - 300
Dribble Volume, $in.^3$	0.0006
Nozzle/Chamber Material	Silicide-Coated Columbium Alloy
Application	Space Propulsion/RCS
	Free to Radiate
Minimum Pulse Duration	10 msec
Maximum Pulse Rate	25/sec

As previously noted, the bipropellant engine was mounted on a traversing mechanism located in an antechamber attached to Chamber 10V. The fuel and oxidizer run tanks, feedlines, and pressure and flow-rate measurement instrumentation were located along with the engine in the antechamber. An isolation valve between the antechamber and Chamber 10V interior allowed access to the engine while Chamber 10V was maintained at test conditions.

Flexible tubing was provided for the fuel and oxidizer supply and drain lines and the GN_2 pressurization lines to the run tanks to allow the propellant feed system to move with the engine when the engine was traversed into firing position. Manual isolation valves were located in the supply and drain lines just exterior to the antechamber wall. The propellant run tanks were filled from 240-$in.^3$ supply tanks located in propellant consoles near the chamber. Approximately 20 $in.^3$ of propellant was transferred from the supply tanks to the run tanks initially and as the run tanks became depleted during testing. Figure 5 is a

schematic of the propellant system. The propellant supply system from the run tanks to the engine conformed to the recommendations of Ref. 22 on feedline length and size and also pressure and flow-rate measurement instrumentation. The engine operation was controlled by a millisecond (msec) sequencer which was programmed for bipropellant valve electrical pulse widths and intervals between 1 and 9,999 msec. Engine combustion chamber pressure (P_c), fuel and oxidizer flow rates, and feedline pressures were recorded on a CRT visicorder oscillograph, along with the bipropellant valve voltage pulse.

The engine was positioned axially in the chamber by means of a worm gear drive system in the antechamber. Axial position was indicated by means of an 18-in. scale, readable to ±0.10 in., attached to the engine mount sting. The engine was primarily aligned to fire horizontally along the chamber centerline. All engine positioning was relative to the location determined for the electron beam nozzle profile number density measurements (approximately 12 in. from the antechamber door). Nozzle movement required from this location was retraction toward the antechamber of up to 8 in. for electron beam axial profile number density measurements and extension of up to 4 in. and vertical translation of 1.5 in. for electron beam back-flow region number density measurements.

3.3 ELECTRON BEAM AND LIGHT SCATTERING DIAGNOSTIC SYSTEM

The measurement technique and the composite instrument system were designed to fulfill the requirements for both gas and liquid drop phase diagnostics. A spatial map of gas species densities and N_2 temperatures in the forward flow and N_2 densities and temperatures only in the back-flow region were to be measured, and the presence of liquid drops in the forward flow was to be assessed. The low exit plane density values of the 100:1 area ratio nozzle dictated that the forward flow field, as well as the back-flow region diagnostics, be performed using the electron beam fluorescence technique. Laser-augmented droplet photography was originally recommended for use for the study of the liquid-phase effluent utilizing a high power Ar^+ laser. A photographic system including a framing camera was to be preceded in the optics train by a low-gain image intensifier. An alternate approach using a vidicon detector arrangement was substituted as a preferred technique. The alternate approach was chosen because: (1) the same devices used for the electron beam measurements could be used for the droplet/particle measurements with improved sensitivity, (2) the viewport required for the camera installation would be available for a viewing dump which was required for the electron beam measurements, (3) a relative quantitative assessment of the droplet/particle effects could readily be made such that changes in the test matrix as related to important engine parameters could be made, and (4) synchronization of the data acquisition time and duration relative to the thruster burn time could be implemented.

A description of the electron beam technique as used previously in Chamber 10V is noted in Ref. 12. Shown in Fig. 6 is the experimental arrangement. Both forward- and back-flow measurements were made with the installation as shown. Two electron beam collectors were required. The beam was directed vertically for forward-flow measurements with the engine on centerline. Shown in Figs. 7 and 8 are photographs of the electron beam source and collectors and assemblies. Back-flow measurements required pitching the electron beam to clear the nozzle and adjusting the engine elevation to provide for a radial scan. In each case the optics were focused at the centerline elevation of the electron beam.

Since the electron beam spread as it traversed the chamber from source to collector, it was determined that the electron beam must be swept across the slit image to ensure that the detectors see all of the beam fluorescence. This ensured that measurements in the rarefied portions of the plume (back flow) were in proper relation to the exit plane measurements where, potentially, the beam spreading problems could give reduced signal levels. Figure 9 illustrates how the beam sweep was implemented with respect to the nozzle position and the spectrometer slit. The electron beam was swept across the image of the spectrometer slit which was located on the flow centerline and aligned perpendicular to the flow direction, i.e., the slit width was parallel to the plume axis and the slit height normal to the axis. Beam sweeping minimized the effects of electron beam spreading, attributed to both elastic and inelastic electron-molecule collisions, on the species densities.

Shown in Fig. 10 is the experimental arrangement for the laser scattering measurements. The axis of the laser beam was made to coincide with the axis of the electron beam so that the same detector system could be used for both measurements. Collector assemblies for the respective beams were positioned using rotary feed-throughs. Since only forward-flow laser scattering data were required, only a single energy receiver was used. Off-axis measurements again were possible using elevation changes in the thruster. Different axial positions were obtained as noted earlier. Photographs of the laser scattering components and installation are presented in Figs. 11 and 12.

The integrated diagnostic system included a high-energy (30 kv) electron beam source, synchronized electron beam sweep system, an electron beam collector assembly, pulsed ruby laser (conventional mode) assembly and beam injection optics, laser beam receiver (energy dump), collection optics assembly, spectrometer, photomultiplier tube (PMT), intensifier-vidicon and readout-control devices, PDP-8 computer system, and an assortment of other control and data readout devices. In addition, a sonic orifice gas source was provided for calibration purposes. The subject devices were interconnected to the thruster control system to synchronize the measurements with the engine firing sequence. These and other system components are shown in Figs. 13 and 14.

The measurements used a double spectrometer for spectral analysis of the fluorescence and the scattered laser light. A PMT was used to map the back-flow region and selected profiles, both radially and axially in the forward-flow region. The volume of the gas sample being viewed by the system was 3 mm wide, 6 mm high, and 5 mm in depth, and the output of the PMT was a measure of the integrated emission over that volume. The data were obtained using a photon counter and read by the computer to permanent storage along with other appropriate parameters. The spatial profiles were obtained by moving the thruster to each desired position. At each location the data were taken by synchronizing the beam sweep and counter gate with a selected portion of the engine burn time. The ratio technique for determining rotational temperatures was chosen; in this mode, the spectrometer was required to move to a second wavelength selection for continued data acquisition at each location. The fluorescent intensity at one of these wavelengths was used to determine the species density.

The intensifier-vidicon device was coupled to the spectrometer as the forward-flow detector system. This system, entitled VICS (vidicon-intensifier coupled spectrometer), was chosen because of its potential to obtain more data at a faster rate. With the appropriate optical collection system, the light could be collected according to a position in the flow field corresponding discretely to a position on the vidicon detector; thus, spatial measurements could be made with individual data acquisition sequences. The VICS output for a particular axial location is sketched in Fig. 15. To display the full nozzle exit diameter (1.47 in.) on the 0.5-in.-diam face of the intensifier, a 0.3 optical magnification factor was used. The horizontal dimension or abscissa of the intensifier corresponds to wavelength; for a given radial position a horizontal intensifier read scan was performed to determine either the rotational temperature (T_R) of N_2 or the species densities of N_2, CO, CO_2, and H_2 - H_2O.

3.4 DIAGNOSTIC INSTRUMENTATION AND CONTROL SYSTEM

A block diagram of the instrument system is shown in Fig. 16. Figures 17 and 18 are variations of the basic system required to accommodate the back-flow and the light scattering measurements, respectively. Because each phase used common devices, the component units were assembled and programmed as a composite system, applicable to the desired measurement. Shown in Fig. 19 is a timing diagram of the data acquisition functions. The data delay, gate, and beam sweep function were obtained from a storage oscilloscope which was also used to monitor collector current or PMT output.

Referring to Figs. 16 through 19 and the timing diagram in particular (Fig. 19), consider the following description of the functional sequence for the VICS data. Before data could be retained on the vidicon target, it was erased to remove dark current accumulation. This interval is noted as vidicon preparation in Fig. 19 and was under computer control. Upon

completion of the target erasure, the computer tested the fuel/oxidizer system to determine if a permissive selection had been made. If this test were unsuccessful, an abort was implemented and a new test sequence was set up. If a permissive were selected, the fuel system was supplied a five-volt pulse from the computer. As long as this control pulse was applied, the thruster continued to pulse according to the on-off selections programmed on the fuel console. A pulse was also supplied to the display oscilloscope from the fuel/oxidizer system which corresponded exactly to the timing features of the electrical pulse supplied to the engine propellant valve. The leading edge of this pulse triggered the sweep circuit in the oscilloscope. The computer subsequently counted oscilloscope gate pulses; after a preassigned number of engine firings, the firing pulse supplied by the computer was removed. Immediately after this pulse was terminated, the computer read the vidicon data for transfer to floppy disk. Usually only a single engine pulse was used when in the VICS mode in order to limit the effect of dark current.

Multiple functions were performed with the display oscilloscope. The pulse counting function in conjunction with the computer was noted above. In addition, the oscilloscope was used to gate the intensifier on during the actual interval of data recording on the vidicon target. When the PMT was used, it also gated on the photon counters. The sweep output from the oscilloscope was used as a control function for the electron beam sweep drive circuits. The adjustable delay feature of the oscilloscope was used to delay the data gate with respect to the leading edge of the engine fire pulse. The electron beam collector current and the analog output from the photon counter ratemeter were inputs to the signal channels. Alignment of these signals when making PMT measurements assured that the beam axis and the spectrometer slit were in optical alignment.

In reference to the timing diagram of Fig. 19, the delay in the initiation of the data gate from the display oscilloscope was selected according to application of the system. For example, during the light scattering measurements this delay was varied to monitor contamination effects throughout the thrust profile and after engine shutdown. Consider the following timing sequence. When the propellant valve was electronically activiated, the leading edge triggered a delay — when terminated, initiated the gate. This gate turned on the intensifier for 5 msec. A delay was inserted from the leading edge of this gate which in turn generated a laser fire pulse after 2-msec duration. The laser had a nominal 750-μsec energy pulse reaching threshold in about 250 μsec with peak intensity occuring at 500 μsec. Thus, data acquisition could be considered to occur at approximately the sum of 2.5 msec and the manually selected delay from propellant valve activation. When the oscilloscope gate interval was completed, the computer was subsequently flagged to begin a vidicon read sequence after engine shutdown had been accomplished.

When the system was in the electron beam and PMT mode, a similar sequence was in effect. The principal difference was that the laser functions were not involved, and the data gate generated by the oscilloscope and applied to the counter was lengthened in order to be on during most of the burn profile (see Fig. 17). The delay of 15 msec was selected to ensure engine stabilization before beam sweeping and data gating were initiated. A gate width of 200 msec was selected for both the forward- and back-flow measurements. An engine pulse time of 250 msec was selected to ensure that data acquisition did not occur during engine shutdown because of possible error in both the delay and the fuel system timing circuits.

The vidicon target was divided into an array containing 256 rows and 256 columns of storage elements called pixels. The amount of charge in each pixel was proportional to the amplitude of the incident light on that pixel. The charge was read out by the vidicon computer interface which integrated the charge to produce a voltage proportional to the amount of charge in the pixel. Each pixel was located for readout according to its row and column addresses. The resultant output voltage was converted by the interface into a digital equivalent and sent to the computer for storage on floppy disk.

The computer controlled all operations of the interface and the reading of the data from the target. The computer sent commands to or accepted data from the interface by means of 12-bit input/output buffers. The output of commands was accomplished by a strobe which signaled the interface to accept the command from the output buffer. The need for a transfer of data was accomplished by a flag that was monitored by the computer as an indication of when to input data from the interface. The interface controlled erasure of the vidicon target and the reading of data from the target. Data were read by rows with the interface providing automatic data conversion and stepping between pixels.

Data were read from the target in rectangular patterns of pixels called fields. There were 13 fields and each consisted of four adjacent rows of pixels. Each row was configured to contain 248 pixels starting with the eighth pixel in that row on the target. The fields were spaced symmetrically about one field, which was in the middle of the target, and the spacing between fields was 16 rows. This setup allowed monitoring of 13 positions in the flow field spread over a length of approximately 1.5 inches.

The data obtained from the target-reading process were assembled by the computer into a file for storage in the floppy disk. During the data sequence, two files were created — a data file and a background file. During data reduction, the data in the background file were

subtracted from the data file values to give background-corrected data. Background-corrected data from each row were averaged with the data from the other rows in the field. This averaging was performed for all rows in the same field of several different runs to reduce the effects of random noise.

These spectra were printed on the system line printer in tabular form or displayed on an oscilloscope in analog form by means of the vidicon computer interface. The oscilloscope was also used to monitor the setup and adjustment of the vidicon system.

4.0 TEST DESCRIPTION

4.1 TEST UNIT AND ENGINE OPERATING CONDITIONS

4.1.1 Test Conditions

The Chamber 10V background pressure was monitored during all engine operations with a nude ionization gage located between the chamber wall and cryopanels. Other gages, located in the test volume just behind the engine, were only operated periodically since their operation added a significant heat load to the small LHe cryopump in the front of the chamber. The base pressure achieved in Chamber 10V before the start of engine firings was less than 1×10^{-6} torr. This base pressure was reached with or without the LHe pump filled. The pressure excursion experienced during pulse firing sequences ranged from the chamber base pressure to 1×10^{-5} torr, when the LHe pump was operating, for combinations of pulse widths of 200 msec or less, duty cycles of ten percent or less, and all mixture ratio and P_c variations. The chamber background pressure rose to approximately 1×10^{-4} torr during the 1-sec engine firings. Much of the data acquired at the exit plane and on axis in the forward-flow region were acquired during engine firings made without the LHe pump operating. During these firings, the chamber background pressure rose to near 1×10^{-3} torr. However, these measurements were made within the plume core where the plume expansion was not affected by the higher background pressure.

4.1.2. Data Acquisition and Measurement Uncertainty

The proper engine performance, P_c and O/F ratio, was established with 1-sec engine performance firings made periodically as operating parameter changes dictated. Engine P_c transducer and fuel and oxidizer flowmeter responses were recorded, along with the bipropellant valve operational voltage pulse, for every firing on a CRT visicorder oscillograph (Fig. 20).

The initial feedline pressure settings resulted in an engine P_c within two percent of the desired steady-state level. Measured fuel and oxidizer flow rates were usually five to ten percent below the calculated steady-state levels. Minor adjustment to the feedline pressures were made based on the engine P_c and measured flow rates to obtain the desired P_c on subsequent firings. Reported P_c and O/F ratio are based on steady-state engine conditions. It must be recognized that for short pulse lengths neither P_c nor O/F were necessarily the levels reported, i.e., for a 10-msec pulse length with a desired P_c of 100 psia, the actual maximum P_c measured may be 65 psia, whereas the fuel and oxidizer flow rates could not be measured. The actual pressure response trace for the shortest pulses must be examined for the true pulse pressure history. The frequency response of the turbine flowmeter signal conditioners required that pulses of greater than one second be made in order to adequately measure flow rate.

4.2 DIAGNOSTIC MEASUREMENTS

The electron beam and laser scattering installation were interchangeable during the entire test sequence. The electron beam measurements were undertaken first, followed by the laser scattering measurements. Generally, all data were taken at 1.4, 1.6, and 1.8 O/F ratios at P_c = 100 psia. The additional case of a 1.4 O/F ratio at 75 psi was taken as an example of a "dirty" combustion process. For a given type of measurement, a prescribed pulse duration was used. Since it was desirable for the thruster pulse to remain fixed, all intensity variations were handled by adjustment of the intensifier gain, the number of engine pulses, or with the use of optical filters in the case of the laser scattering measurements.

A detailed alignment of all components was performed before the chamber pumpdown. Finer adjustments were made after the chamber was at test conditions. The latter was accomplished by adjustment of the lens assemblies both internal and external to the chamber. Pre-pumpdown adjustments included alignment of the electron beam and laser axes along the vertical centerline of the thruster nozzle. The laser beam injection scheme is shown in Fig. 21. The collection optics alignment was made by focusing on an illuminated point on a plumb bob at the thruster centerline reference position. Alignment for the back-flow measurements was implemented in a similar fashion using instead a string between the "B" collector and the electron beam injection orifice (Fig. 6). Adjustments in the "B" collector position were provided to assure that interception of the electron beam by the nozzle (including beam spreading effects) was eliminated. Included in pretest procedures was the alignment of the sonic orifice relative to the electron beam. The positioning mechanism included provision for making axial surveys of the orifice flow field.

The absolute measurements of number density and temperature made with the electron beam required the use of a heated sonic orifice for calibration purposes. The sonic orifice expansion is very well understood (Ref. 23) for given source conditions (pressure, temperature, and orifice diameter); therefore, density and temperature of the calibration gases were analytically determined. Appropriate calibration measurements were made intermittently during the course of the test.

Only relative measurements were possible with the laser scattering system. However, a partial calibration was run in air at atmospheric conditions for an assessment of the Rayleigh component in the event particulate and droplet intensity levels were near background levels. These measurements were also used for the purpose of determining spatial sensitivity factors across the vertical dimension of the VICS detector system.

Two input data sequences were required for all measurements. Data were taken initially with the engine on and either the electron or laser beam on followed by a background measurement taken with the beam off but engine on. During data reduction these were subtracted before application of other required numerical processes, the results being the contribution caused by beam excitation without a contribution caused by engine emission or detector dark count. Additional measurements utilized during the light scattering experiments were beam on with the engine extended and retracted, and beam on and off with engine retracted. These provided a measure of scattered light from sources other than the flow and, in effect, proved inconsequential compared to gas and particulate scattering levels.

4.2.1 Electron Beam Temperature and Density Measurement

The electron beam conditions were always established at 30-kv and 1-ma total current. After the beam system stabilized, a preferred focusing was obtained by selecting a balance between orifice current and beam spreading at the collector. After the beam was established in the appropriate collector (A or B, depending upon whether forward- or back-flow measurements were to be made), the sonic orifice flow was established. The optical alignment was then further refined; this generally involved only lateral and vertical adjustments in the external lens.

As noted earlier, beam sweeping was used so that the beam spreading effects could be minimized. To avoid unnecessary nozzle heating and to minimize the risk of nozzle damage, the sweep direction was in the direction of the nozzle. Sweep angle adjustments were thus required and selected to ensure that all the fluorescence swept across the slit image. The angle size was minimized to avoid unnecessary nozzle impingement. The proximity of the

exit plane measurements to the nozzle was limited by the beam sweeping technique and quenching effects. The final adjustments in alignment were made by monitoring collector current and signal intensity simultaneously on the display oscilloscope while adjusting both to ensure coincidence of the respective peaks during beam sweeps.

All measurements of position for both the thruster and sonic orifice were taken with respect to the line taken between the beam injection orifice and the collector cup. These measurements failed to hold after pumpdown, apparently because of the movement of the chamber systems attributed to thermal and mechanical loading effects caused by the cryogenics and vacuum, respectively. Both the VICS and PMT sonic orifice measurements indicated that the sonic orifice had, upon chamber evacuation and cooling, shifted position relative to the electron beam in both the axial and transverse directions of the horizontal plane. In addition, the electron beam had shifted with respect to the optical line of sight. A good PMT calibration was obtained, however, by performing an axial scan of the orifice and fitting the results to the known slope of the sonic orifice density expansion. That is, the experimental count rates were shifted in axial distance until the two slopes matched, thereby establishing the correct axial distances (Fig. 22). The typical departure from a good fit of experimental points to the calculated slope at low x/D is attributed to effects of quenching, alignment, and sharpness of radial peak profile. With the sonic orifice data and the calculated density expansion ratio at x/D = 18.70, a calibration factor was established. This number was assumed valid for all three days of the PMT back- and forward-flow measurement.

The sonic orifice calibrations included measurements on N_2, CO_2, CO, and H_2. The intensity measurements, at known P_o and T_o, provided the means whereby the density of the respective components in the exhaust plume was determined.

4.2.1.1 Back-Flow PMT Measurements

Only nitrogen data were acquired with a PMT as the detector in the back-flow region. As previously discussed, fluorescence from the N_2^+ First Negative System's (0,0) vibration-rotation band was chosen for analysis of N_2 rotational temperature and number density. Preliminary calculations of the band profile as functions of vibrational and rotational temperature were accomplished with program VIBTEMP. Inputs of great importance to this program were the spectrometer's reciprocal dispersion and slit widths; the former was carefully established as a function of wavelength in previous work. In order to obtain the maximum sensitivity wide slit widths were chosen, and the low resolution or spectrally unresolved mode of operation in which the ratio technique for rotational temperature must be used was the result. Three wavelengths were selected from the computer results for

adequate coverage of the expected rotational temperatures: 3912.00 Å, 3905.25 Å, and 3899.00 Å. The relative intensity at 3912.00 Å as a function of rotational temperature is shown in Fig. 23; nitrogen density was obtained at this wavelength. Ratios of the intensities at these three wavelengths as a function of rotational temperature are shown in Figs. 24 through 26. All three experimental ratios were always calculated in order to remove any doubt caused by the double-valued function of Figs. 25 and 26. Calibration of the spectrometer's wave-number dial was accomplished in sonic orifice flow by scanning the (0,0) band's rotational lines of accurately known wavelengths with narrow slits.

A spectrometer slit height of 2 mm was selected, corresponding to 6 mm in the flow field. This back-flow configuration used the "B" collector; the thruster was translated vertically and axially for position selection. The spatial variations in the density and temperature measurements were accomplished with these two engine movements, corrected for the pitch in the electron beam.

The pulse time for PMT data acquisition was chosen as 0.25 sec in order to keep the test chamber pressure as low as possible. Subsequently, for the very low density cases, multiple firings were used. Each pulse was separated by a 10-sec interval. A delay of 15 msec to ensure engine stabilization was applied before initiating the 0.2-sec sweep. The beam on-off sequence was also used for back-flow PMT measurement. The 0.25-sec engine pulse length was chosen to be slightly longer than the 0.2 sec noted above to ensure that data acquisition was completed before engine shutdown.

Scans were taken at fixed engine elevations a point at a time, with variations chosen in horizontal directions. The engine was moved forward at 0.25-in. intervals. Subsequent data were taken at intermediate points where large gradients existed. The extreme limits included those positions where there appeared to be a constant background density. The computer program was written such that the three predetermined wavelengths and a background wavelength at 3922.00 Å were automatically selected and it was possible to obtain both temperature and density data at a given location on the same data run.

4.2.1.2 Forward-Flow PMT Measurements

Precisely the same procedure for data acquisition was followed in the forward-flow PMT measurements as was used in the back-flow, except that a fixed axial position was chosen with variations in vertical direction (radial) in 0.125-in. steps. The near exit plane position was initially chosen with the same criterion as discussed in Section 4.2.1 pertaining to nozzle impingement and quenching. Off-axis measurements were also pursued to complement the back-flow data around the nozzle and farther downstream for rarefied boundaries of the plume.

4.2.1.3. Forward-Flow VICS Measurements

One-second sweep times were used for these measurements. The engine pulse time was slightly longer than one second to ensure that the beam sweep was completed before engine shutdown. Two engine pulses were required for each data point in a beam-on, beam-off sequence. The latter was subtracted from the former during data reduction to remove the background component from the data.

At a specific O/F ratio, all data required for determining the spatial variation of the densities and temperatures were taken. At fixed axial positions, all data for each species were taken. This required specific wavelength selection for each species of interest. In addition to the N_2^+ (1-) (0,0) band and H_β Balmer line, bands of the CO^+ ($A^2\Pi$ - $X^2\Sigma$) Comet-Tail System and the CO_2^+ ($A^2\Pi$ - $X^2\Pi$) Fox, Duffendack and Barker System were monitored for CO and CO_2, respectively. Where potential spectral interference problems existed with bands of CO and CO_2, several wavelength selections were used. In addition, multiple runs for N_2 were made using both resolved and unresolved spectra. This was done to verify the temperature measurements using the unresolved spectra. Data were taken at axial locations out to 8 in. downstream from the nozzle.

Sensitivity adjustments were made as required by intensifier gain selection. Usually a beam on-off sequence at test conditions would be taken for the purpose of establishing signal levels. A rapid recall capability was provided for data readout on an oscilloscope display. In the event readjustments were required, a new intensifier voltage was selected. Multiple data input sequences were taken depending upon the signal levels relative to the noise component. The data reduction program had a provision for coadding spectra directly from the disk used for data storage.

4.2.2 Laser Light Scattering Measurements

The system used for these measurements was essentially that utilized for the electron beam forward-flow measurements, except that the electron beam was replaced with a laser beam along the original beam axis. A laser energy receiver, which was positioned by means of a rotary feedthrough, was moved over the E beam source. The beam collector assembly was similarly rotated out of position to allow injection of the laser beam into the nozzle test region. The laser injection optics were arranged such that the laser beam just filled the projected slit image (Fig. 21). External optics adjustments were required to optimize light collection. The spectrometer wavelength was set to 6943 Å. Signal sensitivity was selected by way of the intensifier gain.

The hardware arrangement provided for the capability of moving the data acquistion time anywhere within the thrust profile relative to the leading edge of the electrical pulse activating the thruster valve (Figs. 16 and 19). In addition, the data could be obtained after engine shutdown. The intensifier was turned on for 5 msec after the inserted delay and the laser triggered 2 msec after the intensifier gate. The laser pulse was typically 750 μsec in length for the energy levels involved after a 250-μsec threshold delay. The laser energy was chosen at a value large enough to ensure stability of energy and threshold delay. Thus, 2.5 msec was chosen as the point where the data were taken after the inserted delay time.

An engine on-off sequence was followed for the data and background measurements, such that the difference would take into account any scattered laser light from system components. Measurements were also made with the engine on and laser off to ensure that background emission from the engine was inconsequential. Pretest and posttest data included measurements in air to take into account molecular scattering effects.

The relative measurements of scattered light intensity made during the combustion profile required a reference level. This reference measurement was chosen as the data point immediately before shutdown for a 100-msec pulse at 1.6 O/F ratio and 100-psia chamber pressure. The assumption was that with an extended pulse length, engine stabilization was established and thus would represent a minimum contamination condition.

5.0 DISCUSSION OF RESULTS

5.1 ELECTRON BEAM MEASUREMENTS

5.1.1 Discussion of PMT Back-Flow Data

Measured engine count rates were corrected for detector system dead time, τ_{DT}, by assuming the dead time value of 25 nsec which had been measured previously in a similar system. The true count rate C″ is $C'' = C'/(1-C'\tau_{DT})$ where C′ is the measured count rate. After subtracting background count rates, the count rate ratios of the three wavelengths were computed and compared with the computer-calculated values of Figs. 24 through 26 to obtain rotational temperature. The resultant averaged values for the back-flow region are shown in Fig. 27.

To obtain nonquench corrected number densities, n_{NQ}, the corrected count rates at 3912.00 Å were multiplied by the temperature-dependent bandshape factor B and the sonic orifice calibration factor C_{so}:

$$n_{NQ} = C'' B C_{SO} \tag{18}$$

where

$$B = B_{cal}/B_{T_R}$$

B_{cal} is the relative intensity value of Fig. 23 for the sonic orifice calibration flow's rotational temperature and B_{T_R} is that value for the thruster's measured rotational temperature. C_{SO} is the sonic orifice flow true count rate at the calibration point divided by the number density at that point. Then, to correct for quenching, the final true number density, n, is

$$n = n_{NQ}/\left[1 - \left(n_{NQ}\,\overline{k\tau}\,/0.3075\right)\right] \tag{19}$$

where $\overline{k\tau}$ is the quenching factor of 2×10^{-17} cc/molecule (Ref. 10) and the theoretical mole fraction of N_2 in the exhaust is 0.3075.

The back-flow results are shown in Fig. 28. The indicated engine axial coordinate has been shifted 0.35 in. over that measured when the chamber was warm and at atmospheric conditions. This amount of shift is subject to interpretation, and the justification for that used was the direction and position of the lines of constant number density. The radial coordinate is also subject to errors of the same cause but is shown unchanged.

5.1.2. Discussion of PMT Forward-Flow Data

Evaluation of the nitrogen data near the exit plane indicated the existence of a shock. Therefore, an axial centerline measurement was made to help characterize the shock structure. The axial scan indicated peaks of both number density and rotational temperature 2 in. downstream, and a radial survey was then taken at this location. Off-axis measurements were also recorded to complement the back-flow data around the nozzle and farther downstream for rarefied boundaries of the plume. Axial and radial profiles of rotational temperature and number density are shown in Figs. 29 through 32. The axial coordinate was shifted by the same 0.35 in. mentioned before.

5.1.3 Discussion of VICS Electron Beam Nitrogen Rotational Temperature Measurements

Near-exit-plane nitrogen rotational temperatures were measured in the spectrally resolved mode on three separate testing days. In this case narrow entrance slit widths (70 to 100 μm) were set such that, except for the first several lines of the N_2^+ (1-) (0,0) R branch, the rotational lines were spectrally resolved and each line's peak height was unaffected by its two neighbor lines. An example spectrum from each test day is presented in Fig. 33; each is

the result of averaging multiple runs. These spectra have been magnified by the indicated factors to facilitate their measurement, and thus the P branch has been blown off scale. It was easily seen that a background of large amplitude underlay the R branch, especially upon comparison with the computer-calculated spectrum of Fig. 34. The bandhead of the (1,1) band should appear at 3884.3 Å. This background's amplitude distribution was determined by using the natural two-to-one amplitude alternation between odd and even numbered rotational lines. After determining the peak heights, a background point was plotted underneath an even numbered line by averaging the higher two neighboring odd numbered peak heights and subtracting the distance between the average and the even numbered peak height from the even numbered peak height. A similar procedure was done for each odd numbered line. The general shape of the background became clear after several spectra were analyzed in this manner and the results for the sample spectra are shown in Fig. 33. Each spectrum's background was established in this laborious manner. The final peak heights were input to program TROT after it was modified to accept any particular lines chosen. Boltzmann plots for the three sample spectra are shown in Fig. 35.

The rotational temperature results are presented in Fig. 36. Not all radial positions were calculable because of low signal levels. The indicated error bars represent one standard deviation and are indicative of the randomness of peak height amplitudes. Each temperature determination is also subject to error caused by inaccurate computation of the spectral background, and this is estimated to be in the order of ± 5 percent.

No N_2 rotational temperatures were calculable from the unresolved N_2^+(1-) (0,0) band, three of which are shown in Fig. 37, because of the presence of the high background. No way exists to remove that background for comparison to computer-calculated band profiles, one of which is presented in Fig. 38. Attempts were made to correlate several bandshape parameters of unresolved spectra with rotational temperatures obtained from corresponding resolved spectra taken immediately preceding or following the unresolved and at the same conditions, all without success. Those temperature-dependent parameters of the unresolved band were spectral location of the R branch peak, ratios of R branch amplitudes at two wavelengths, and ratios of P and R integrated branches, all of which included the interfering background.

5.1.4 Discussion of VICS Electron Beam Nitrogen Number Density Measurements

Upon examination of the sonic orifice calibrations for the intensifier-vidicon measurements and with the knowledge of the orifices' spatial shifts caused by chamber cryogenic pumping which were learned in the PMT measurements, it became necessary to

reject the calibration data. The probable shift to a small, not well-known sonic orifice X/D where the axial density gradient is large, and the usage of high reservior pressure led to the calibration data having been recorded in a flow region of high number density where radiation quenching effects are strong and not well known. As a result, all VICS nitrogen number density measurements reported herein are relative.

Assuming the anomalous background to be proportional to the actual number density, the latter was obtained by summing the P and R branch integrated intensities. This sum is independent of rotational temperature. Correction factors caused by various intensifier high voltages and intensifier field number sensitivities were applied to the sums. The high-voltage factor was determined by measuring the integrated N_2^+ band intensities in sonic orifice flow fields as the reservoir pressure was varied along with the high voltage, and the result is presented in Fig. 39. Values from a least squares fit of laser scattering data of intensifier field sensitivities were employed for the second calibration factor; the data are shown in Fig. 40.

Two independent axial centerline forward-flow profiles of the engines' N_2 number density are shown in Fig. 41; each one is relative within itself only. High voltages of from 1,750 to 1,830 volts and from 1,720 to 1,780 volts, respectively, were used for these profiles. Radial profiles of relative N_2 number density corresponding to the axial positions of Fig. 41b are presented in Fig. 42. The validity of the field sensitivity correction factor is exemplified by the manner in which the profile at x = 6.35 in. was leveled. To observe the flow field at increased radial distances, the engine was raised 1.19 in. and profiles recorded at four of the same axial positions. These data, the results of which are shown in Fig. 43, were recorded with high voltages of from 1,800 to 1,850 volts. Comparison of Figs. 42 and 43 in the overlapping region shows a poor match of the relative densities between r = -0.45 and -0.70 in. This could have been caused by the differing high voltages and engine spatial positioning error. However, the overlay from r = -0.73 to -1.92 in. is generally good. Also, at large radii the data are consistent in that relative densities increase with increasing axial distance. Figure 44 is an additional density profile from resolved data which agrees well with the unresolved data profile at the same axial position.

Three spectral profiles of the atomic hydrogen H_β line, Fig. 45, are shown magnified by various factors. Both H_2 and H_2O, when impacted by the electron beam, contribute to the population of this line, and on the basis of this single spectral measurement the relative concentration of each cannot be determined. After integration of the H_β line, its signal strength was ratioed to that of N_2 for each corresponding field, and then plotted with the minimum ratio set to 1.0. These results are presented in Figs. 46 through 48 for three O/F ratios. Off-axis enhancement of the ratio is clear in all cases. Relative to O/F = 1.6, the

standard condition, no enhancement of H_2 - H_2O for the O/F = 1.4 and 1.8 cases was evident, as shown in Fig. 49. These data were derived from the ratios of Figs. 46b, 47, and 48. The average of all H_2 - H_2O/N_2 ratios for O/F = 1.4 is 1.00, and for O/F = 1.8 is 1.01.

Order of magnitude estimates of H_2, CO, and CO_2 absolute number densities were made by ignoring the sonic orifice spatial shift uncertainties discussed previously. Pure H_2, CO, and CO_2 gas spectra were measured with the VICS system. Assuming all the H_β radiation was from H_2, the H_2 density at the centerline of the exit plane was approximately 10^{16} cc^{-1}. Only the merest hint of CO and CO_2 radiation was recorded; the maximum estimated CO and CO_2 number densities were 10^{15} cc^{-1} and 10^{14} cc^{-1}.

5.1.5 Discussion of Correlation Between PMT and VICS Nitrogen Results

The shock structure observed in the radial surveys of the PMT data does not match the central peak character of the VICS data either in rotational temperature or number density. Compare Figs. 31 and 32 with Figs. 36 and 42. Additionally, axial profiles of temperature and density do not match; no axial downstream peaks are observed in the VICS data. Compare Figs. 30 and 41. In the unreported exploratory electron beam measurements of Phase I in which narrow band pass filters were used, solid evidence for the existence of the shock structure and downstream density peak exists. Therefore, the ability of the VICS system to spatially resolve the features becomes questionable. That is, poor optical focusing throughout the coupled system could have led to image smearing, and the final signal upon a particular field would be the sum of signals from adjacent radial positions. There was fair agreement of the average radial temperatures as determined by the PMT and VICS techniques. The lack of axial downstream peaks in the VICS data can be explained under this supposition. For instance, with much smearing, the average radial PMT rotational temperature at x = 0.60 in., Fig. 31, may be equal to or greater than that at x = 2.35 in., whereas the centerline temperature is considerably less at x = 0.60 inch.

Uncertainties of ± 15 percent or more in the PMT back-flow rotational temperatures are indicated in Fig. 27; the minimum uncertainty for the remainder of the determinations is ± 8 percent. A systematic error of ± 3 percent is a result of wavelength positioning errors, and random errors in count accumulations as a result of fluctuating flow densities account for the balance of error. The PMT forward-flow rotational temperature uncertainties are somewhat less, as evidenced by the smoothness of the profiles in Figs. 29 and 31, and are a result of high counting rates in the higher density regime. As previously discussed, total uncertainties in the VICS rotational temperatures ranged from ± 10 to ± 17 percent.

PMT absolute N_2 number density uncertainties are large; the principal contribution was attributed to the sonic orifice spatial shifts. These systematic errors are estimated to be ±25 percent. Additional random errors, again, are a result of fluctuating flow densities and increase with decreasing flow-field density. Summing these, the total uncertainties are from ±30 to ±40 percent. Overlap of the VICS relative N_2 number density radial profiles revealed errors in the order of 20 percent; this is thought to be caused by the different high voltages employed, even though measured sensitivity factors were employed.

5.2 LASER LIGHT SCATTERING RESULTS

Since the VICS system was used exclusively to obtain the light scattering data, and because of the relative ease in obtaining data, the available test results are too voluminous to be presented in their entirety in this report. Consequently, only the data that show effects and trends will be presented for discussion purposes. Because the physical processes that are involved are not understood, at least on the part of the authors, these effects will be presented without extensive comment and thereby left to the reader to draw his own conclusions as to the significance of the results presented.

Typical data as actually retrieved from the vidicon target appear in Fig. 50. These data are actually three out of thirteen possible spectral profiles taken around the 6943-Å laser line and spatially represent data from the engine centerline to the nozzle lip. The intensity across this radial variation decreases toward the extreme nozzle edges. The data presented is actually the average of four of 256 vidicon lines. The data reduction program performs this average as the data are retrieved from disk and also integrates under the spectral profile over an assigned wavelength range. Corrections in zero offset are incorporated as required. Experiments were run to ensure that the observed intensities represent particle scattering processes rather than molecular or mechanical reflections. Using the predicted concentrations of gas species from the electron beam data, and the scattering intensities at atmospheric conditions, the contribution caused by Rayleigh scattering is insignificant when compared to even the weakest encounter caused by Mie scattering. Radial intensity profiles derived from the spectral profiles as shown in Fig. 50 are presented and discussed briefly in subsequent sections.

5.2.1 Single 100-msec Pulse Performance

5.2.1.1 Intrapulse Data

As noted elsewhere, the reference data were chosen to be a long engine pulse (100 msec) taken immediately before engine shutdown and at design operating conditions (1.6 O/F

ratio and 100-psi chamber pressure). This was done to ensure engine stability and probably minimum contamination. A radial profile for this condition is shown in Fig. 51. It should be observed that this data is slightly different from the actual reference value. The actual reference value was chosen as the average over several days when the specific test point was run as a pretest and posttest checkpoint. The individual values could vary from day to day because of laser performance, alignment in collection and/or injection optics, and variations in chamber and/or engine operating conditions. Any of these conditions could be in effect for the results of Fig. 51.

Data for specific instances of time during the 100-msec reference profile were taken and the results are shown in Fig. 52 for the centerline and r = 0.1225 positions. Of particular interest are startup effects which are not obvious from the results shown and include the time over which the startup transients occur. The first value occurs at 7 msec and is 45 percent of the reference value. A measurement at 6.5 msec was just discernible at high gain selections and does not appear in Fig. 52. The scattered light intensity, therefore, went from zero to half amplitude in 0.5 msec. Transient effects of a resolution less than 0.5 msec were impossible because of the commensurate time of the laser pulse duration. Recall that the time measurements are referenced to the leading edge of the electrical pulse operating the propellant valve. Shown in Figs. 53a and b are the radial profiles for the first two data selections at 7.0 and 12.5 msec, respectively (0.5 and 5.5 msec after valve begins opening). The shape of the radial profiles are significant in that these results indicate the light scattering sites are concentrated around the axial centerline. Intrapulse characteristic include:

Time, msec	Location of Maximum Value (Field No.)	Value	Half-Amplitude Width, in.
7	7	0.454	0.73
12.5	6	1.086	1.21
92.5	6	1.108	1.23

5.2.1.2 Postpulse Data

Shown in Figs. 54a through e are time plots for relative scattered light intensities. Figures 54a and b data are for near centerline positions and 54 c through e are for near nozzle lip positions. The values at t = 0 were taken immediately before shutdown and are plotted for comparison purposes. Other values occur after shutdown. Because of valve response time, combustion evidently continues for several milliseconds after shutdown. Apparently maximums in scattered intensities occur around two instances, 12 to 18 msec and 45 msec. Radial profiles taken at engine shutdown and near the peak values are shown in Figs. 55a through f. Postpulse characteristics include:

Time, msec	Location of Maximum Value (Field No.)	Value	Half-Amplitude Width, in.
0(-7.5)	6	1.01	1.18
2.5	6	0.99	1.18
7.5	6	1.02	1.04
12.5	6	8.92	0.85
47.5	7	15.59	0.68
52.5	7	12.38	0.58

Consistent with startup performance, the shutdown according to the radial distributions tend to shift position and become narrow.

5.2.2 20-msec Postpulse Performance

Shown in Fig. 56 are typical results for a 20-msec engine pulse. This time was chosen as a standard test pulse for these studies. These results do not appear significantly different from a 100-msec pulse time. The time variations for the 20-msec case indicate valley depth between the maximums, which also occured at 18 and 40 to 45 msec, to be somewhat better defined when compared with the 100-msec case. Figures 57a through c show for extreme off-center positions even more peak contrast near the nozzle lips. Radial profile characteristics are noted below.

Time, msec	Location of Maximum Value (Field No.)	Value	Half-Peak Width, in.
0(-0.5)	6	1.09	1.24
18	7	10.98	0.748
38	8	18.23	1.09
40	7	23.49	1.07

Similar data were also taken after two 20-msec pulses, separated by a 30-msec interval. Postpulse data are shown in Fig. 58. These data, unlike a single 20-msec pulse, do not show as large a contrast between the peak and valley value. In fact, a double 20-msec pulse appears more like a 100-msec pulse in this regard (see Fig. 54). Similarly, the half-amplitude radial profile widths were also more narrow when compared with the 20-msec pulses. For example, these widths were 0.91 and 0.53 in. at 17.5 and 27.5 msec, respectively.

Shown in Fig. 59 are data for the 1.4 O/F ratio and 100-psi engine pulse. Again, these results are similar to the 100-msec data. Also, the half-amplitude width was 1.19 in. before engine shutdown and decreased to 0.67 in. at 20.5 msec after shutdown. It may be observed for this case that the intensity increases sooner and terminates earlier after engine shutdown when compared with the 1.6 O/F ratio data. Data in Fig. 60 are similar 1.4 O/F ratio and 75-psi data. These data also show intensities increasing earlier, but observable for a period of time comparable to that of the 1.6 O/F ratio cases.

Data for the 1.8 O/F ratio case are shown in Fig. 61. The location of peak intensity relative to engine shutdown is essentially as it was for other O/F ratios. By this result, it can be concluded that any difference in times for the peak scattering intensity are experimentally indiscernible with O/F ratio. However, in contrast to other cases, the scattered intensities before shutdown are smaller for the 1.8 O/F ratio case. The following results summarize those observations.

	O/F Ratio - Pressure, psi	Pulse Length, msec	Relative Intensity
1.	1.4 - 75	20	1.20
2.	1.4 - 100	20	1.19
3.	1.6 - 100	100	1.01
4.	1.6 - 100	20	1.10
5.	1.6 - 100	2 - 20	1.4
6.	1.8 - 100	20	0.79

Errors in timing between the delay and the fuel system time bases may account for the results of item 6 above, such that the results at t = o actually occured after shutdown (see Fig. 58). Discounting this discrepancy, the scattering intensities vary in an inverse way with O/F ratio.

5.3 PARTICLE SIZING ESTIMATES

Some theoretical considerations were presented in Section 2.0 which made it possible to estimate the size range of particles in the exhaust plume. These considerations were based on polarized intensity measurements at a 90-deg scattering angle. Data at two instances of time were used — immediately before shutdown and during a period of intense light scattering, respectively, for an engine condition of 20-msec pulse, 1.6 O/F ratio, 100 psi, at centerline, and 1.1-in. engine position.

The degree of polarization computed from Eq. (17) for the configuration previously described and the index n = 1.335 is shown in Figs. 62 and 63 with superimposed experimental imprecision bands of ±5 percent in the measurements of $\bar{\Phi}_{1,2}(\pi/2,\pi)$. Calculations have been carried out for a range of refractive indices whose real part varies from 1.2 to 1.5 and an imaginary (absorptive) index of 0.1. The degree of polarization is insensitive to the imaginary part of the index, but the uncertainties introduced by the range of the real part of the index are greater than those introduced by measurement imprecision, even for imprecision bands on $\bar{\Phi}_{1,2}$ as large as ±10 percent. Computerized analysis of this type indicates that (for the refractive index range considered) the data taken on centerline at 19.5 msec correspond to particles 0.25- to 0.45-μm in diameter. In contrast, the data taken at 42.5 msec after shutdown correspond to diameters of 0 to 0.15 μm. It is unlikely that the droplets have real refractive index greater than 1.5 (as such is usually appropriate only to dense,

viscious liquids or solid aerosols). Consequently, these data do not indicate the likely existence of supermicron particles at any time during the run.

6.0 SUMMARY

The principal results from the gaseous species temperature and density and particulate matter diagnostic measurements in the plume and back-flow region of the 5-lbf-(22N)-thrust bipropellant rocket engine are summarized below.

1. Near-exit-plane gaseous number density was 1-2 x 10^{-16} cc^{-1} with N_2 being the most prominent constituent. Estimates of CO, CO_2 and H_2/H_2O number densities were made and varied from 10^{13} to 10^{15} cc^{-1}. Temperatures varied from 350°K to 500°K depending upon position. Density (10^{13} cc^{-1}) appeared to become constant in the extended back-flow region with significant gradients near the nozzle lip. These measurements were made with electron beam techniques described herein. A PMT and an image intensifer-vidicon spectrometer coupled system were used as complementary detection techniques for making the required spectral intensity measurements.

2. Uncertainties of the PMT determined rotational temperatures are as high as ±8 percent in the forward-flow region and up to ±18 percent in the back-flow region. Temperature uncertainties from the image intensifier-vidicon system ranged from ±10 to ±17 percent in both regions. Number density total uncertainties were from ±30 to ±40 percent in both regions. An apparent shock structure observed in the radial surveys of the PMT data was not apparent in the vidicon data either in rotational temperature or number density. Also, axial profiles shapes of temperature and density did not match; no axial downstream peaks were observed in the vidicon data. Poor optical focusing throughout the intensifier-vidicon coupled system may have led to image smearing thereby causing the indicated profile differences. The PMT data are adequate for profile definition.

3. Average particle sizes on the centerline during firing and shutdown were 0.35 and 0.1 μm, respectively, for the 100-psia chamber pressure, 1.6 O/F ratio, 20 msec-firing. The measurements were made using laser-Mie scattering techniques described herein. Furthermore, the following observations were characteristic of all the firings.
   a. Particulates or droplets were more apparent after shutdown as indicated by the scattered light intensity which became as much as 25 times greater than during firing. Since the particles actually decreased in size, the postfiring

number density of small particles was on the order of 1,000 – 10,000 greater than the number density observed before shutdown.

b. The particulate concentration (combined liquid droplets and solid particles) appeared highest near the centerline, and the distribution became even more peaked at the centerline after shutdown.

c. The particulate concentration appeared most intense in two "spikes" at approximately 18 and 42 msec after shutdown.

d. The occurrence of these "spikes" was independent of O/F ratio, although the intensity and shape were dependent on O/F ratio.

e. Before shutdown, the intensity of the particulate concentration indicated by the number-size effect varied inversely with O/F ratio.

4. The greatest uncertainty in particle size determination must be attributed to lack of knowledge of the particles' refractive index. For a physically reasonable range of real refractive indices (1.2 to 1.5) the average particle sizes have been estimated within an uncertainty of about ± 30 percent; however, the above range of indices is greater than the range usually associated with liquid aerosols (1.3 to 1.4); hence, the actual uncertainty in size is probably less than the above quoted value.

REFERENCES

1. Williams, W. D., McCay, T. D., Powell, H. M., Weaver, D. P., et al. "Experimental Study of the Plume Characteristics of an Aged Monopropellant Hydrazine Thruster." AEDC-TR-79-2 (ADA068326), April 1979.

2. Williams, W. D., McCay, T. D., Powell, H. M., and Lewis, J. W. L. "Experimental Study of the Plume Characteristics of a New Monopropellant Hydrazine Thruster." AEDC-TR-79-54.

3. Alt, R. E., et al. "Bipropellant Engine Plume Contamination Program, Vol. 1." AEDC-TR-79-28.

4. Lewis, J. W. L. and Williams, W. D. "Electron Beam Fluorescence Diagnostics of a Ternary Gas Mixture." AEDC-TR-73-96 (AD762930), July 1973.

5. Williams, W. D., Hornkohl, J. O., and Lewis, J. W. L. "Electron Beam Probe for a Low Density Hypersonic Wind Tunnel." AEDC-TR-71-61 (AD727004), July 1971.

6. Norman, Wendell, Kinslow, Max, and Lewis, J. W. L. "Experimental Study of Simulated High Altitude Rocket Exhaust Plumes." AEDC-TR-71-25 (AD726555), July 1971.

7. Gilbert, J. R. and Lewis, J. W. L. "Excitation of NII Lines from Dissociation of N_2 and NO by Electron Collision." AEDC-TR-75-77 (ADA012903), July 1975.

8. Lewis, J. W. L. and Williams, W. D. "Collisional Deactivation of Atomic and Molecular Hydrogen." *Journal of Quantitative Spectroscopy and Radiative Transfer,* Vol. 16, No. 11, November 1976, pp. 939-946.

9. Lewis, J. W. L., Price, L. L., and Powell, H. M. "Electron Excitation Cross Sections of N_2^+ $B^2\Sigma_u^+$, NI, and NII States and Their Temperature Dependence." *Physical Review A*, Vol. II, No. 4, April 1975, pp. 1214-1222.

10. Price, L. L. and Lewis, J. W. L. "Collisional Quenching of Atomic and Molecular Nitrogen: I. Experimental Results." AEDC-TR-75-151 (ADA018780), December 1975.

11. Cunningham, J. W., Fisher, C. H., and Price, L. L. "Density and Temperature in Wind Tunnels Using Electron Beams." *IEEE Transactions on Aerospace and Electronic Systems*, Vol. ~~AES-3~~ AES-3, No. 2, March ~~1976~~ 1966, pp. 269-284.

12. Price, L. L., Powell, H. M., and Moskalik, R. S. "Species Number Density Measurements in Plume Interactions with Free Stream Using an Electron Beam Technique." AEDC-TR-71-226 (AD889131L), November 1971.

13. Lewis, J. W. L., Williams, W. D., Price, L. L., and Powell, H. M. "Nitrogen Condensation in a Sonic Orifice Expansion Flow." AEDC-TR-74-36 (AD783254), July 1974.

14. Lewis, J. W. L., Price, L. L., and Kinslow, Max "Rotational Relaxation of N_2 in Heated Expansion Flow Fields." Proceedings of Ninth International Rarefied Gas Dynamics Symposium, Edited by M. Becker and M. Fiebig, Vol. I, DFVLR Press, Porz Wahn, Germany, 1974, pp. B.17-1 - B.17-9.

15. Williams, W. D. "Laboratory Verification Studies of Rotational and Vibrational Temperature Measurements by the Electron Beam Technique." AEDC-TR-68-265 (AD683001), February 1969.

16. Lewis, J. W. L., Curry, B. P., and Weaver, D. P. "Determination of the Size Distribution Function of Particles in a Hypersonic Flow Field." AEDC-TR-77-101 (ADA056923), July 1978.

17. Kerker, M. *The Scattering of Light and Other Electromagnetic Radiation.* Academic Press, New York, 1969, pp. 255-306.

18. Barber, P. and Yeh, C. "Scattering of Electromagnetic Waves by Arbitrary Shaped Dielectric Bodies." *Applied Optics*, Vol. 14, 1975, pp. 2864-2872.

19. Dave, J. V. "Subroutines for Computing the Parameters of the Electromagnetic Radiation Scattered by a Sphere." Report No. 320 3237, IBM Scientific Center, Palo Alto, California, May 1968.

20. Born, M. and Wolf, E. *Principles of Optics*. Pergamon Press, New York, 1970, pp. 633-656.

21. *Test Facilities Handbook* (Tenth Edition). "Von Kármán Gas Dynamics Facility, Vol. 3." Arnold Engineering Development Center, May 1974.

22. Schoenman, L. and Schindler, R. C. "Five-Pound Bipropellant Engine." AFRPL-TR-74-51, 1974.

23. Ashkenas, H. and Sherman, F. S. *Rarefied Gas Dynamics*, Fourth Symposium, Vol. II. Edited by J. H. deLeeuw, Academic Press, New York, 1966, pp. 84-105.

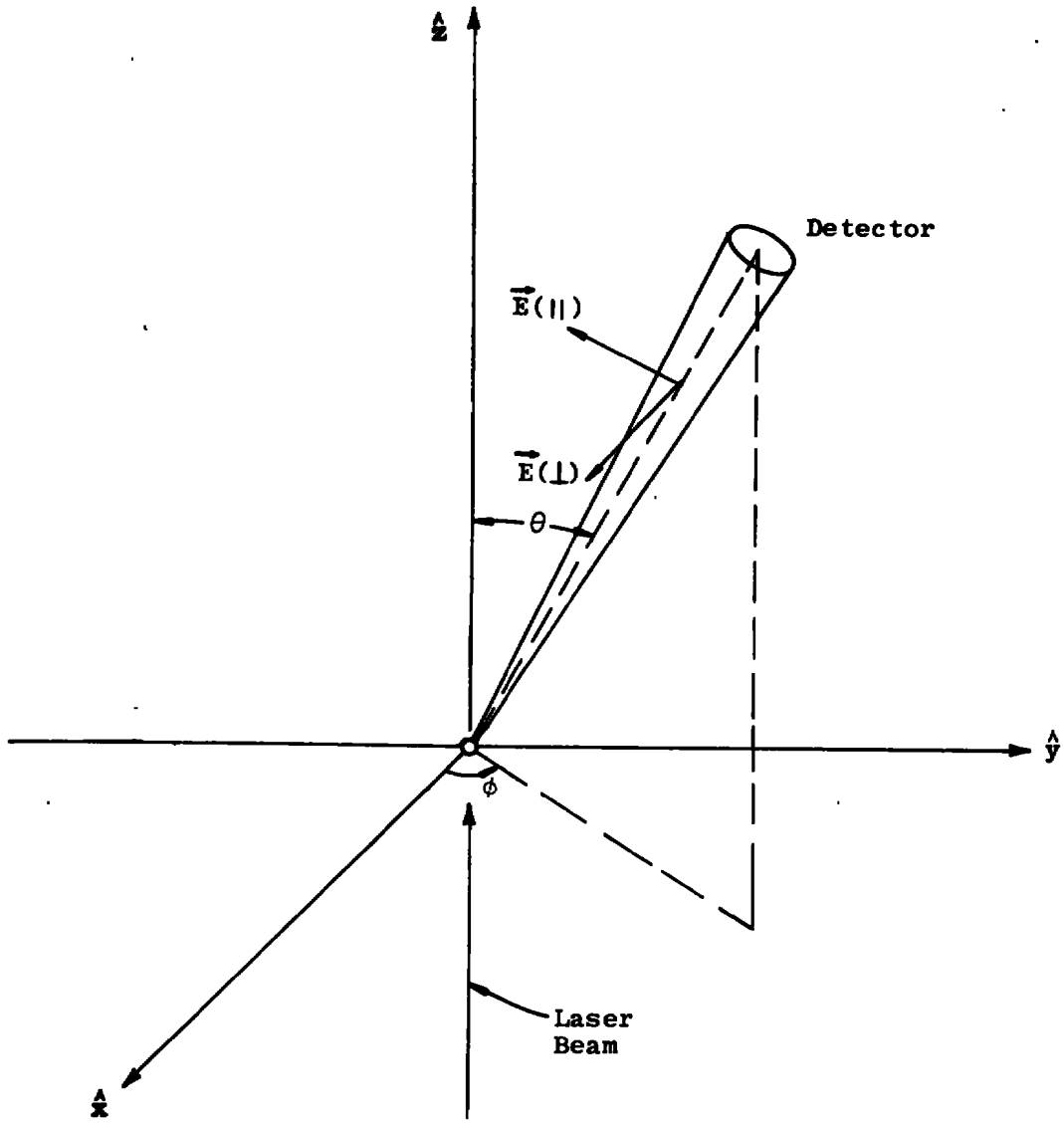

Figure 1. Mie scattering configuration.

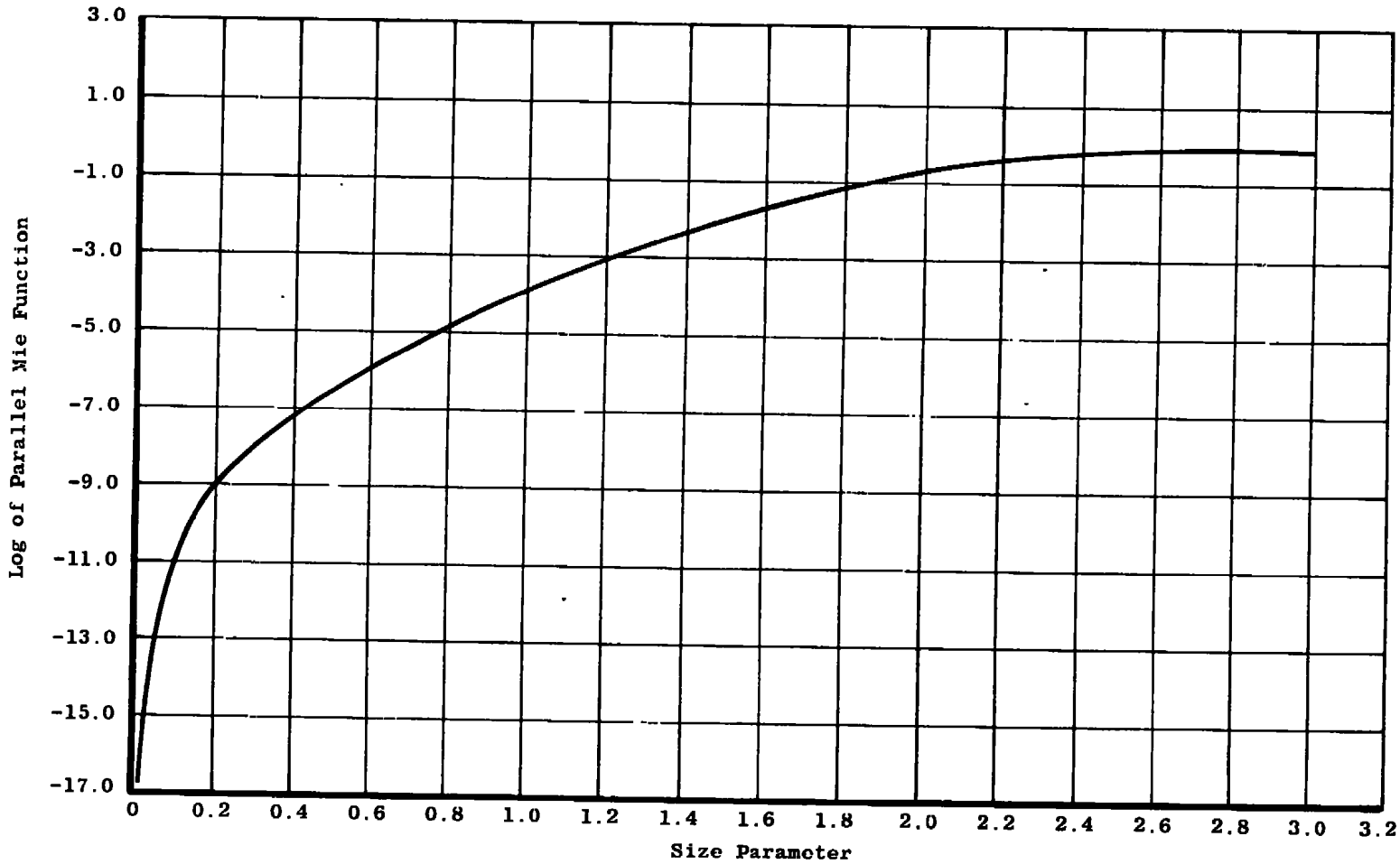

Figure 2. Size dependence of perpendicularly polarized Mie intensity functions for 90-deg scattering angle and integrated over detector subtended angle.

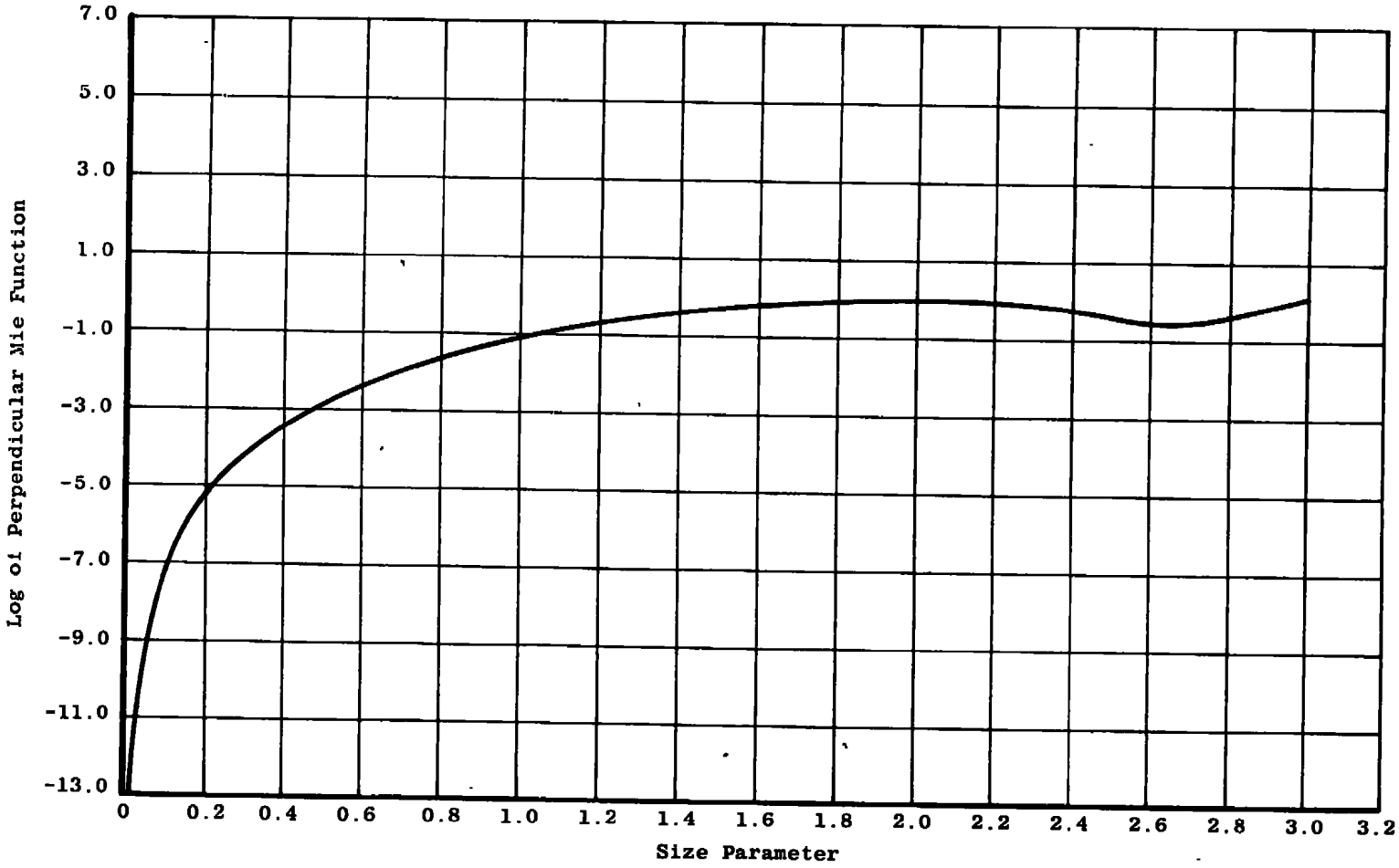

Figure 3. Size dependence of parallel polarized Mie intensity functions for 90-deg scattering angle and integrated over detector subtended angle.

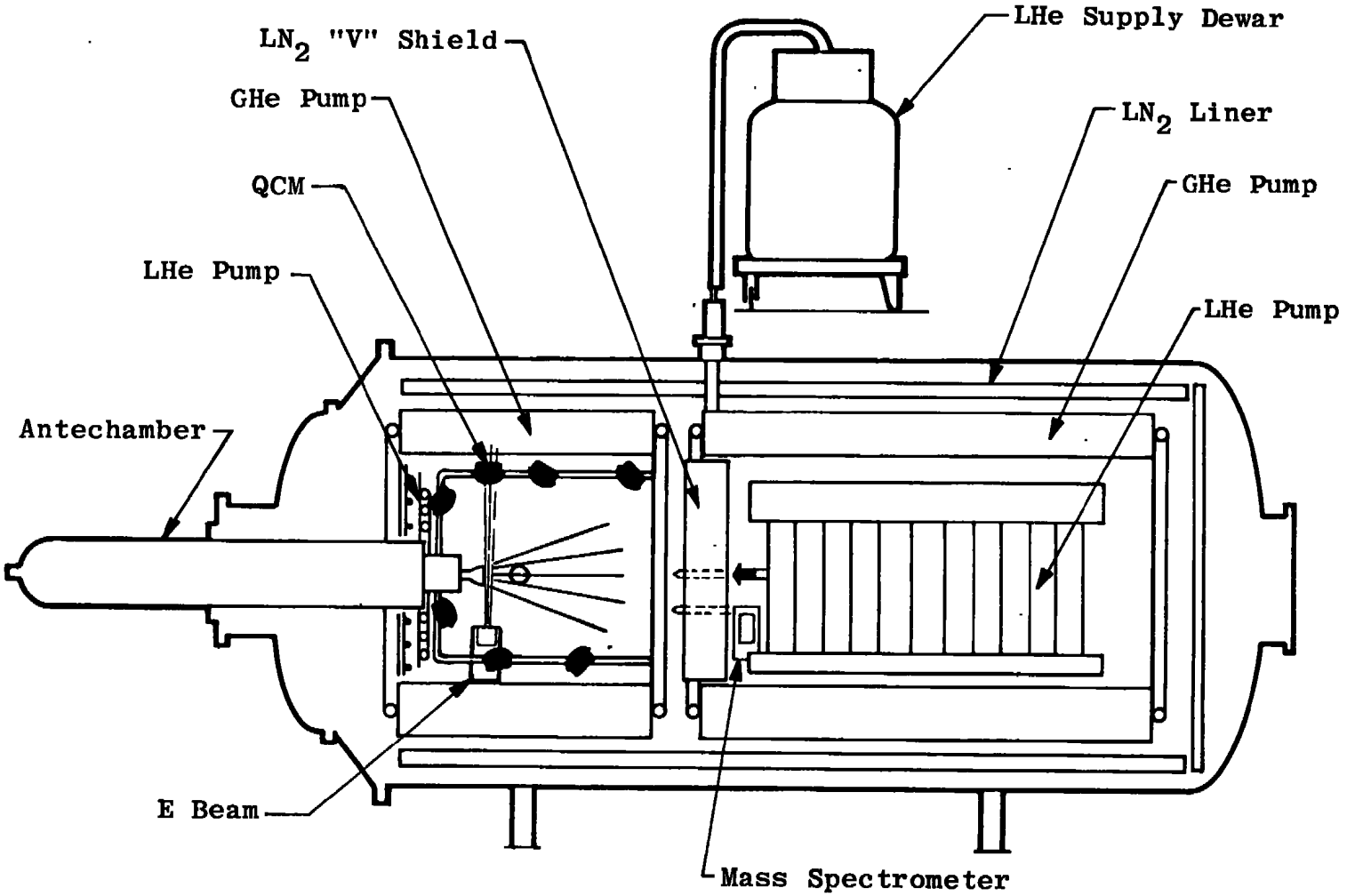

Figure 4. Aerospace Chamber (10V).

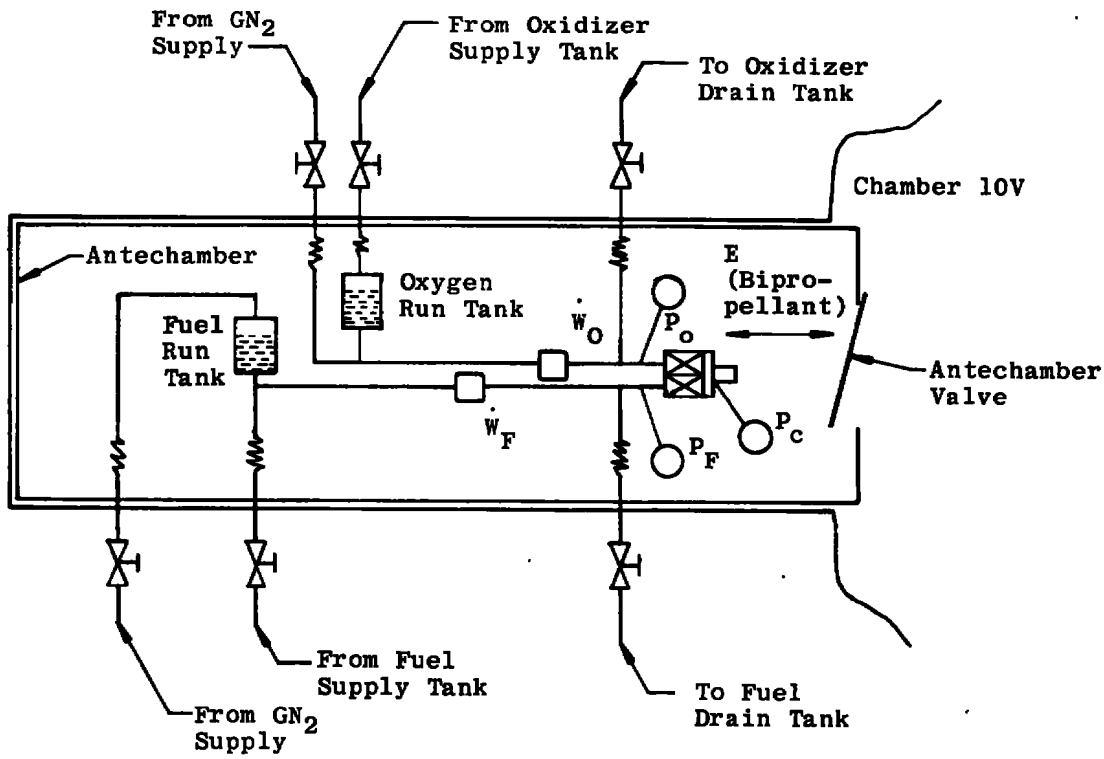

Notes: 1. Run Tank Capacity - 40 $in.^3$
2. Fuel Feedline Length - 60 in.
3. Oxidizer Feedline Length - 33 in.

P_C	Combustion Chamber Pressure	Taber 2210	0 to 200 psia
P_O	Oxidizer Feedline Pressure	Taber 2210	0 to 1,000 psia
P_F	Fuel Feedline Pressure	Taber 2210	0 to 500 psia
$\dot{W}_O$	Oxidizer Flow Rate, gpm	Flow Technology	0 to 0.05 gpm
$\dot{W}_F$	Fuel Flow Rate, gpm	Flow Technology	0 to 0.05 gpm
E	Bipropellant Valve Voltage		0 to 28 vdc

Recorder: Honeywell Model 1858 CRT Visicorder

Figure 5. Schematic of the propellant system.

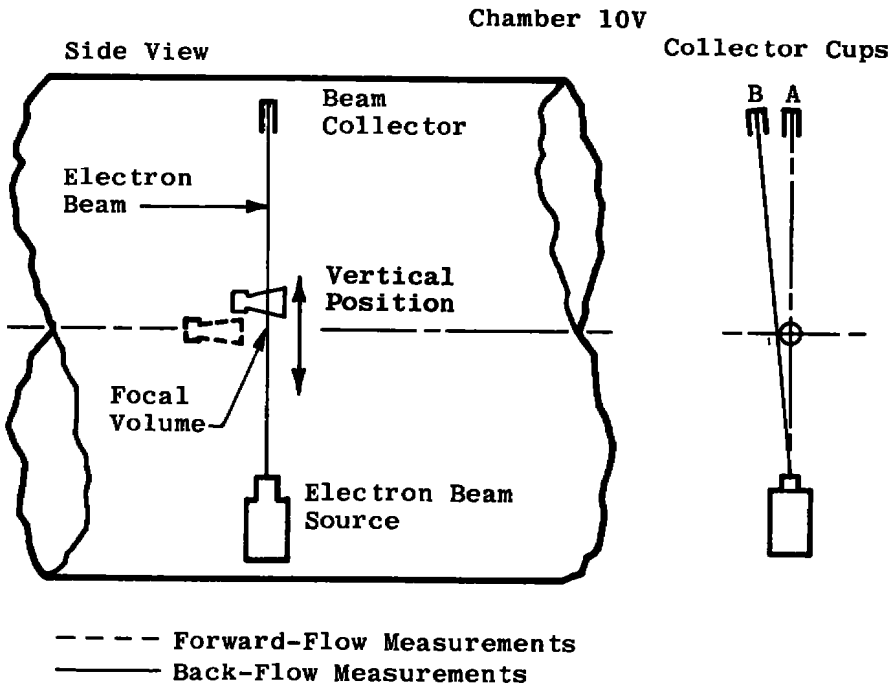

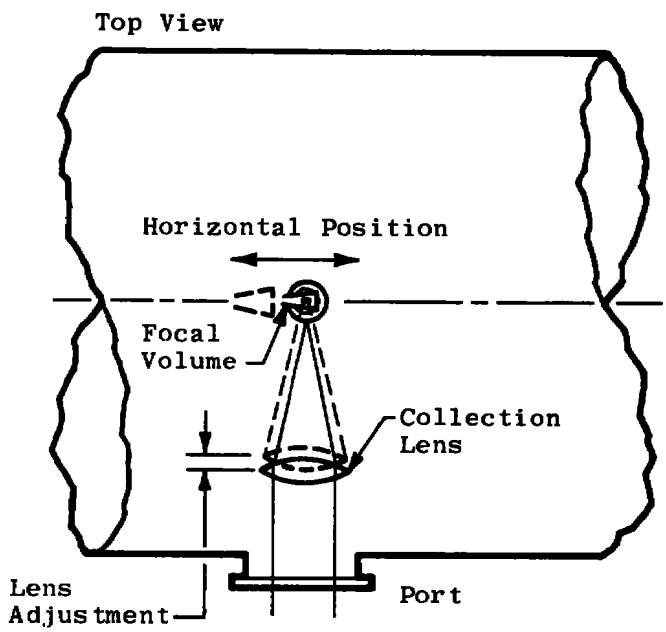

Figure 6. Chamber 10V electron beam measurements for back-flow and forward-flow studies.

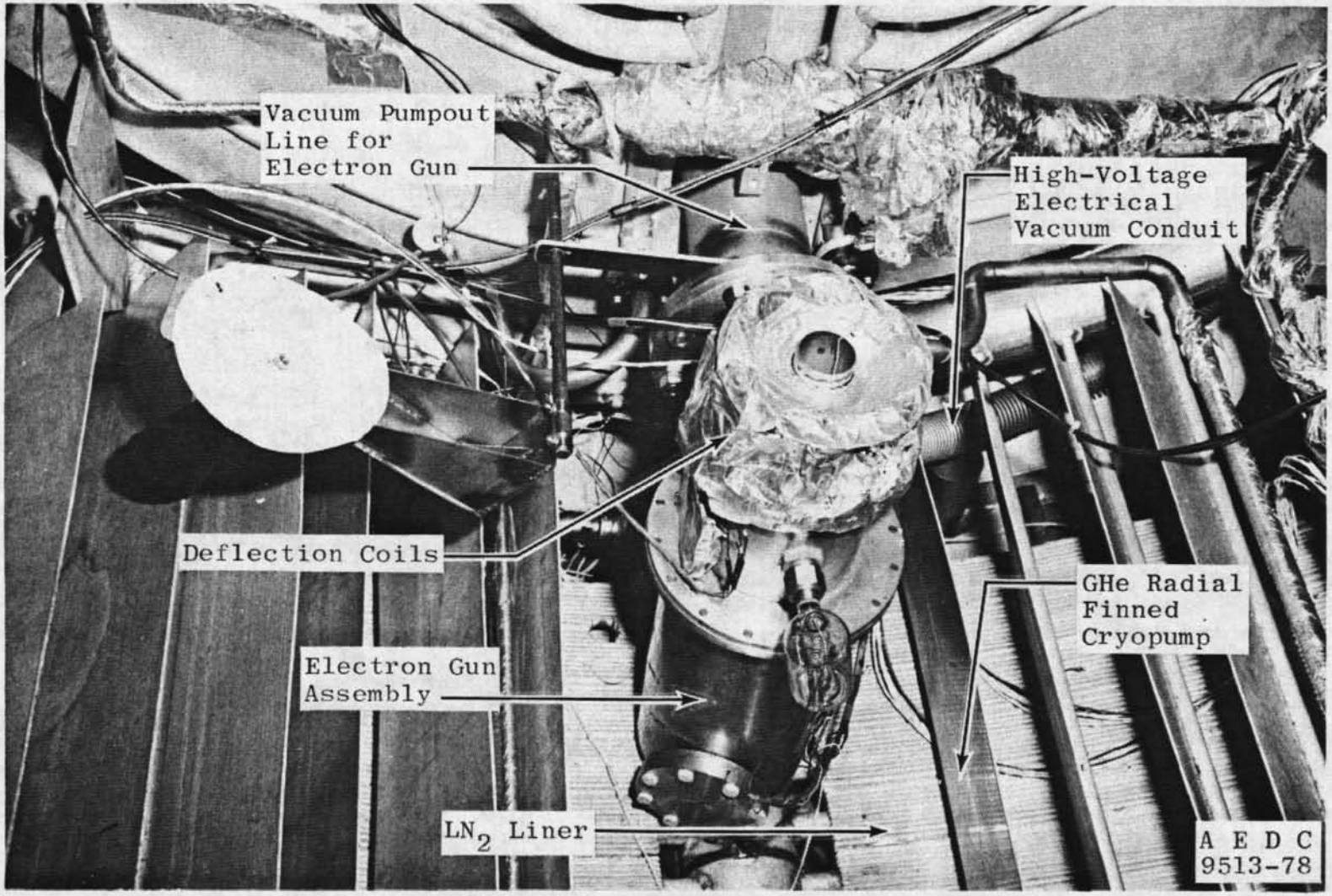

Figure 7. Photograph of electron beam source.

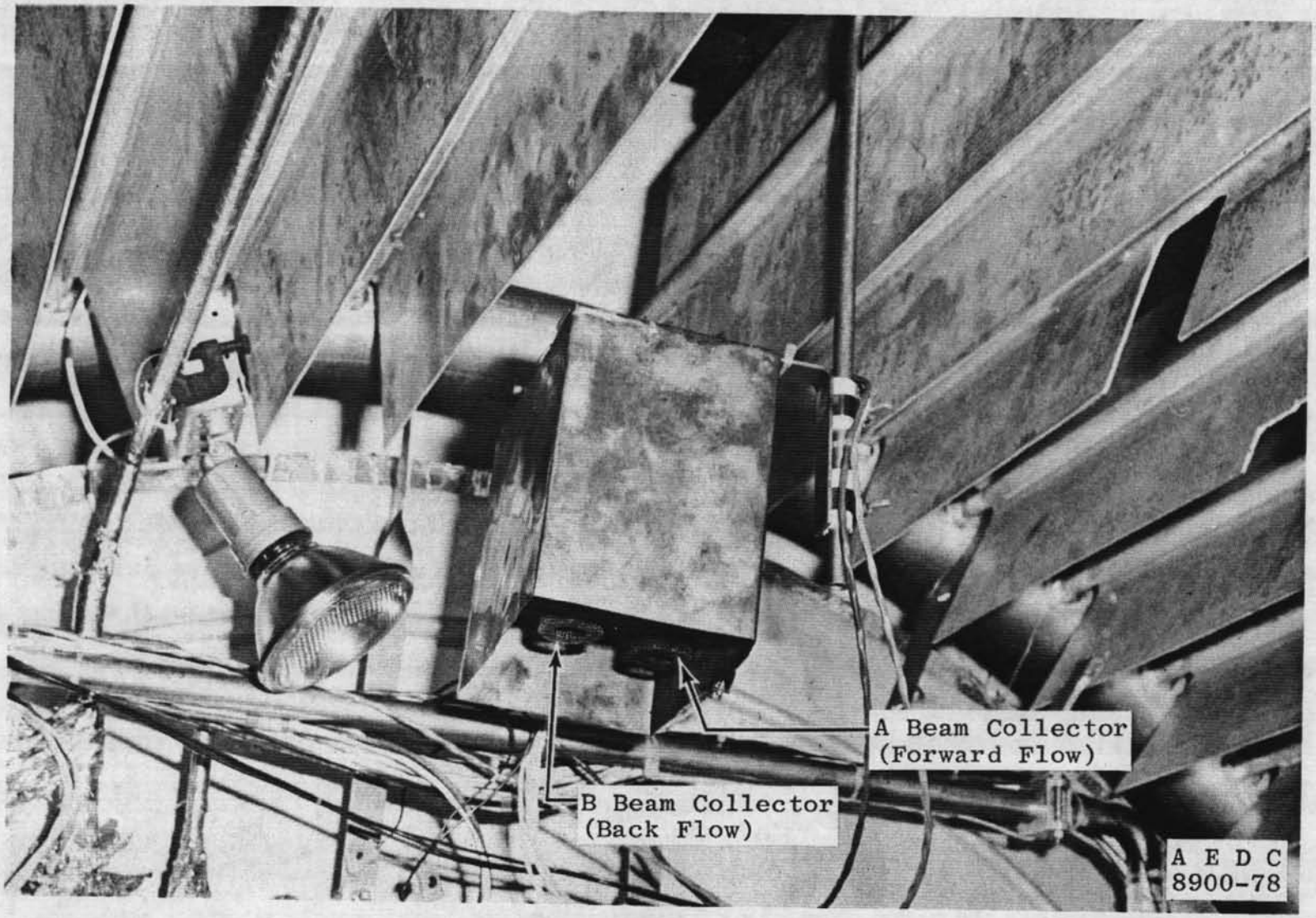

Figure 8. Photograph of electron beam collectors.

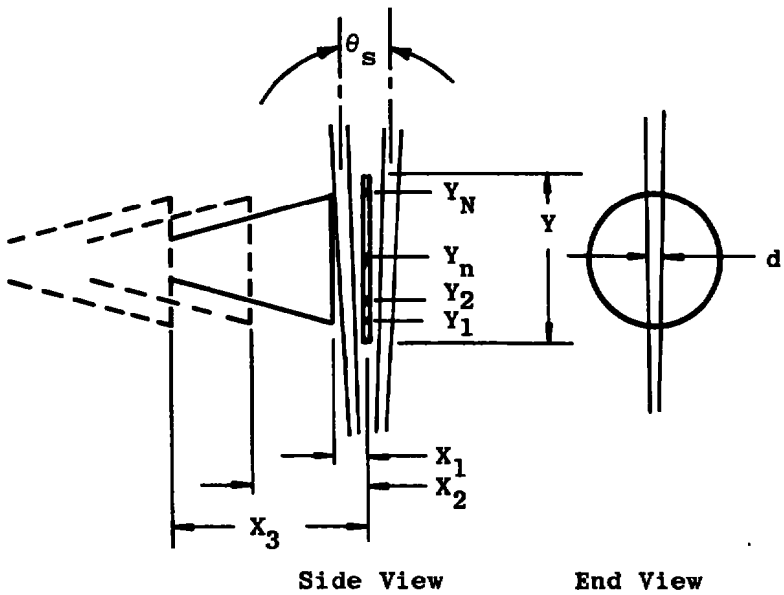

a. Forward-flow region

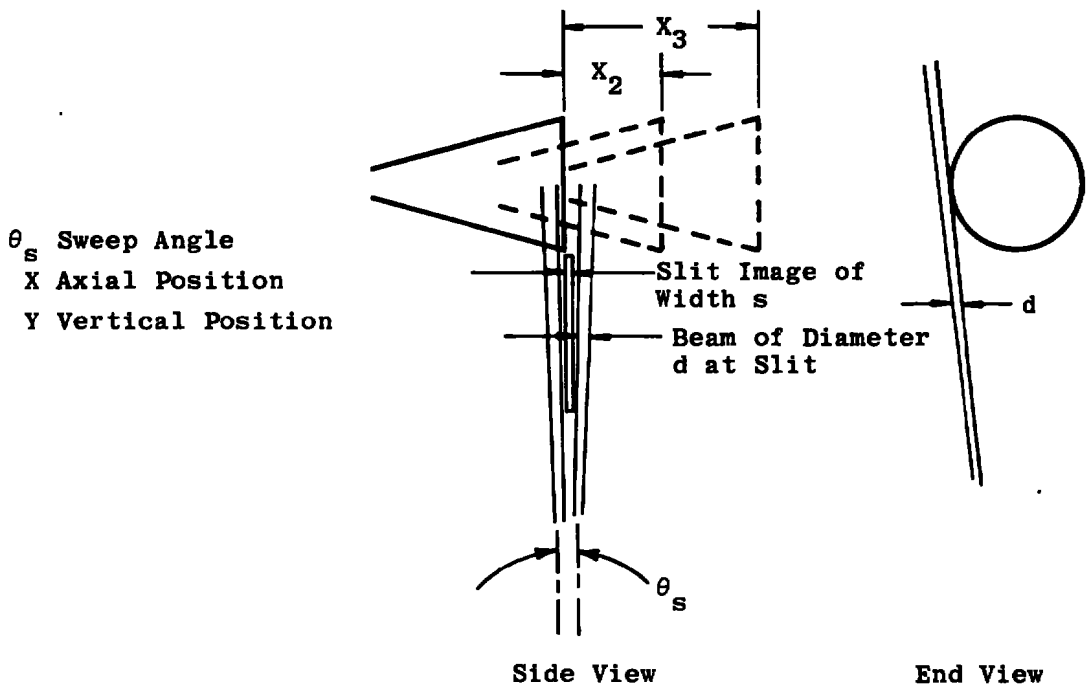

b. Back-flow region

Figure 9. Flow-field mapping technique.

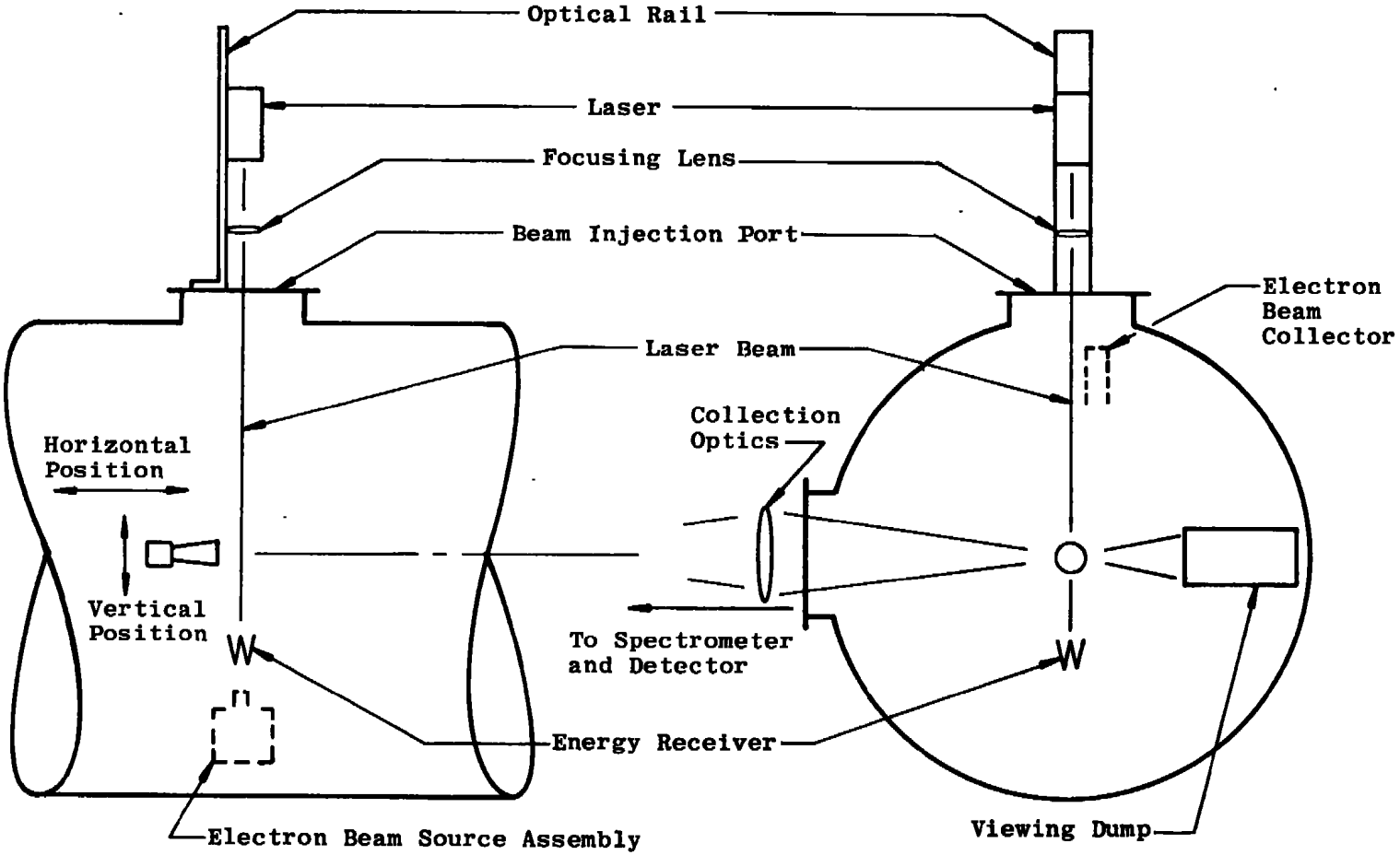

Figure 10. Experimental arrangement for laser scattering measurements.

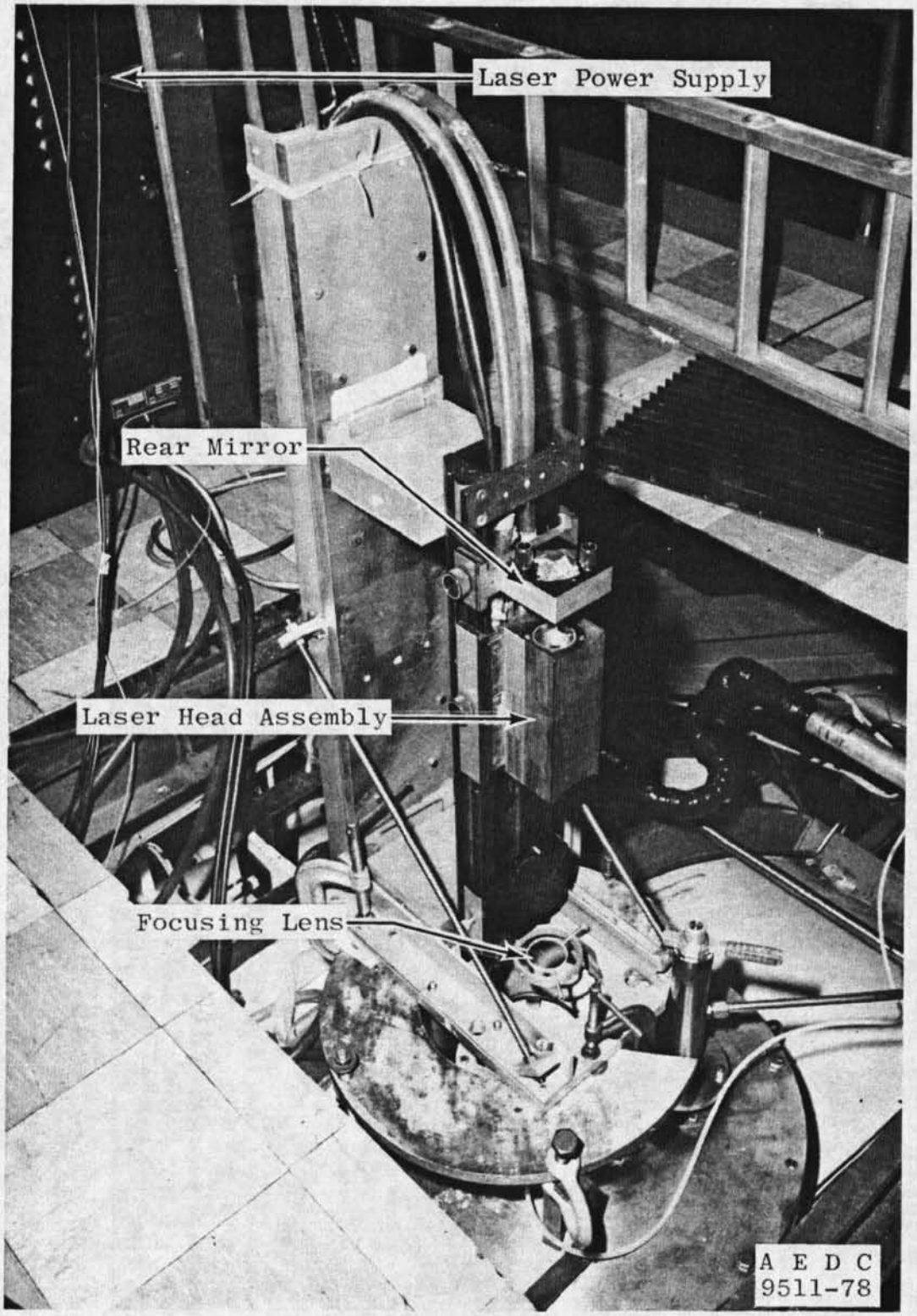

Figure 11. Photograph of ruby laser.

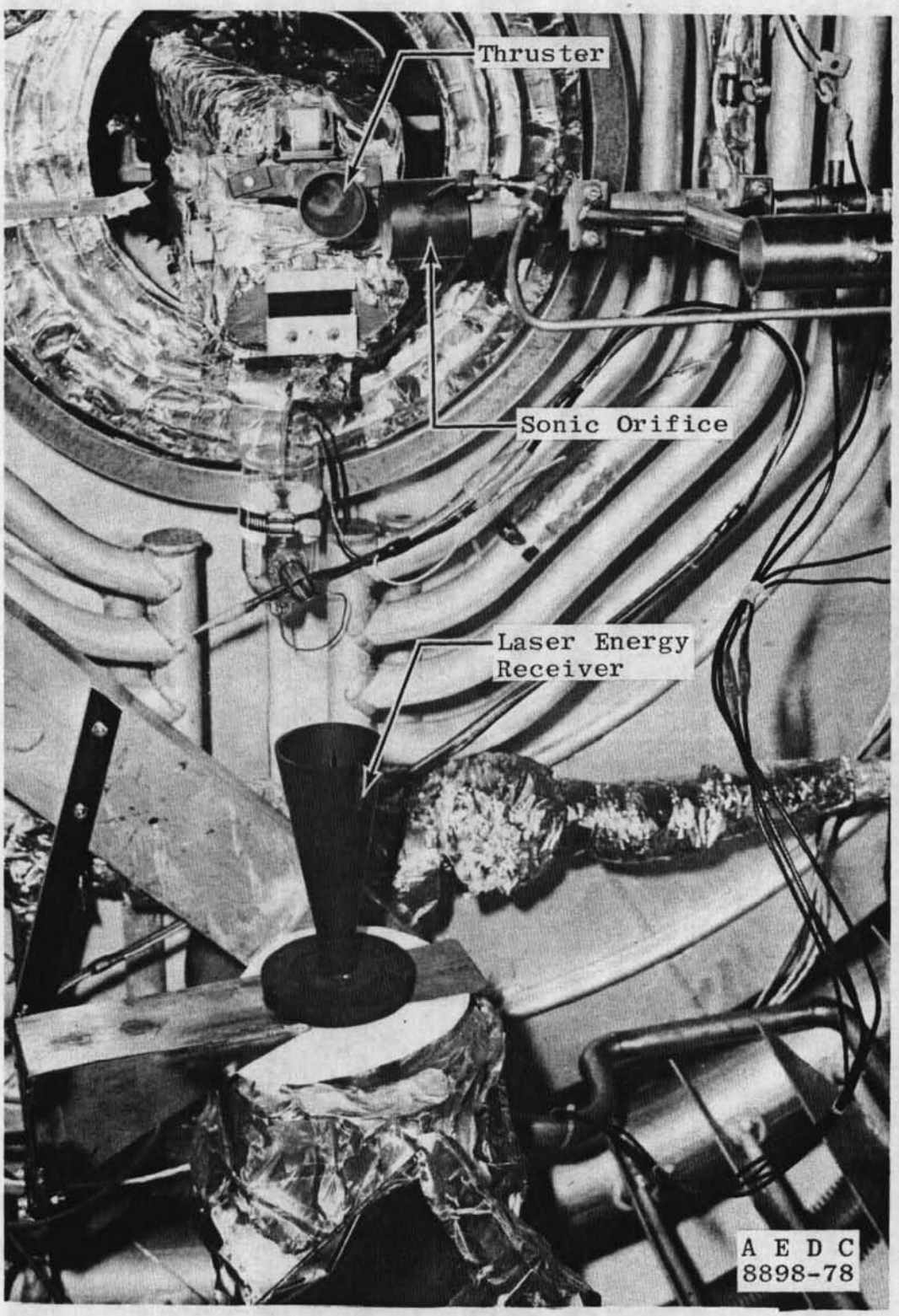

Figure 12. Photograph of laser beam receiver.

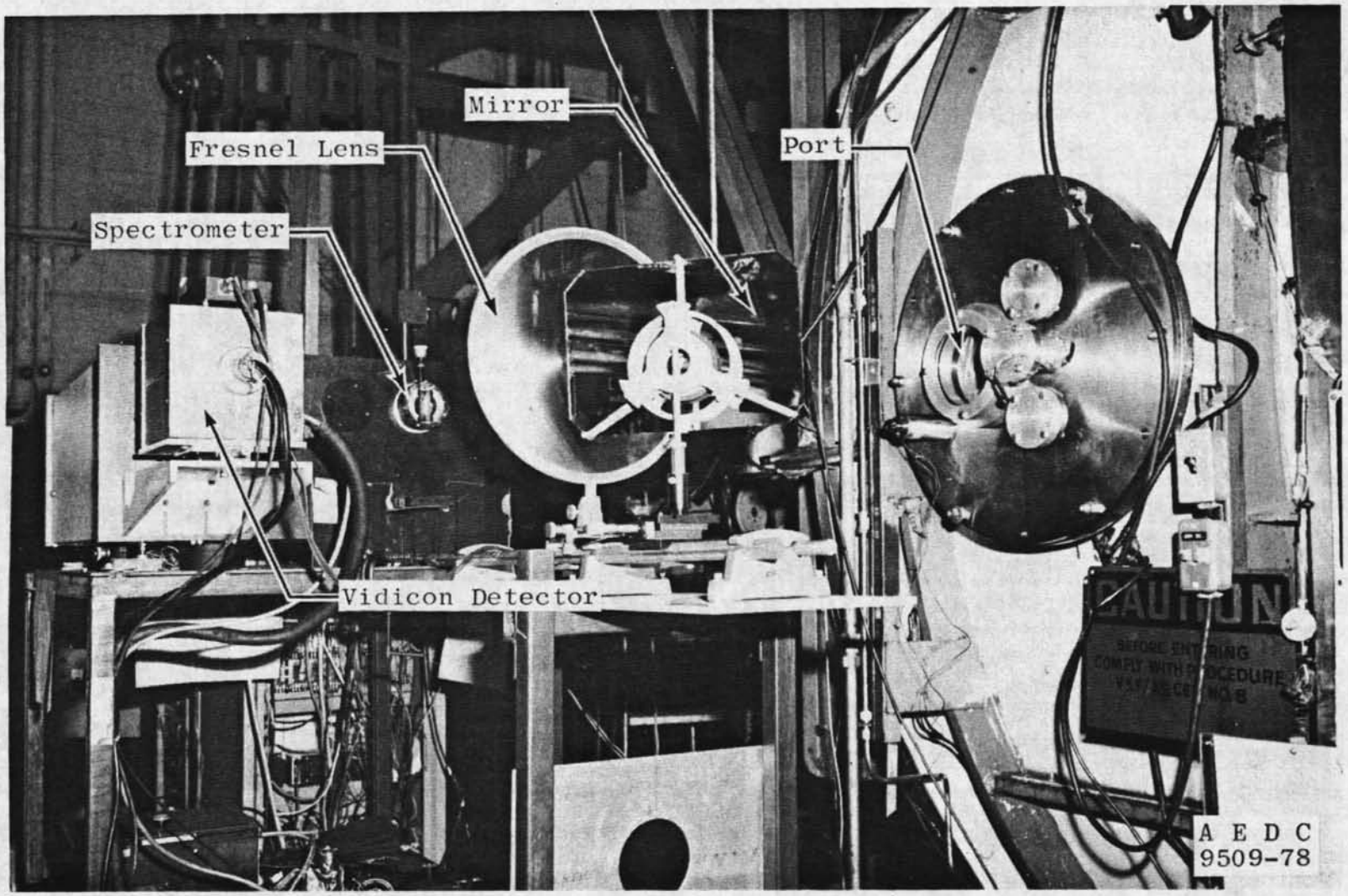

Figure 13. Photograph of collection optics and spectrometer.

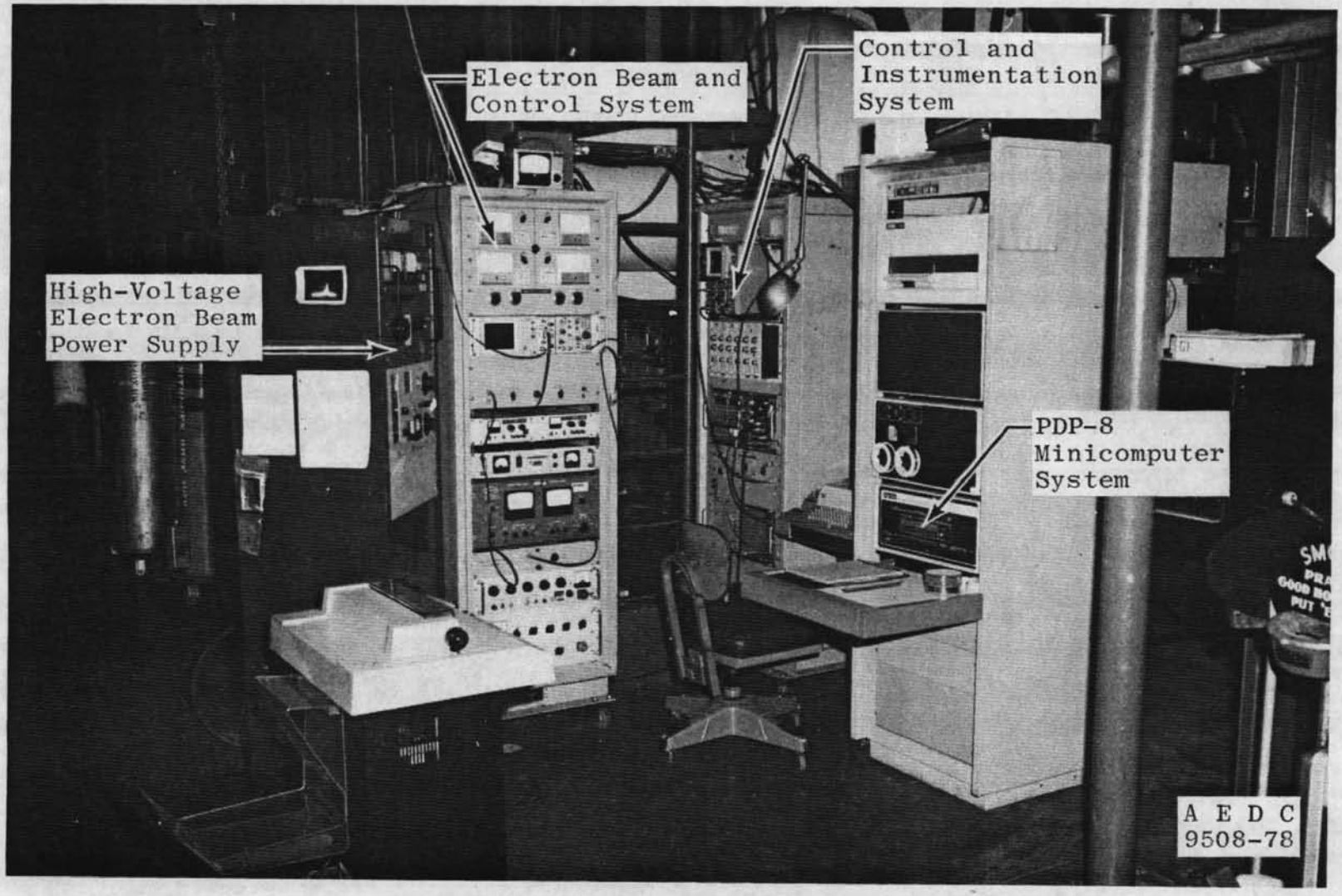

Figure 14. Photograph of electron beam controls and computer system.

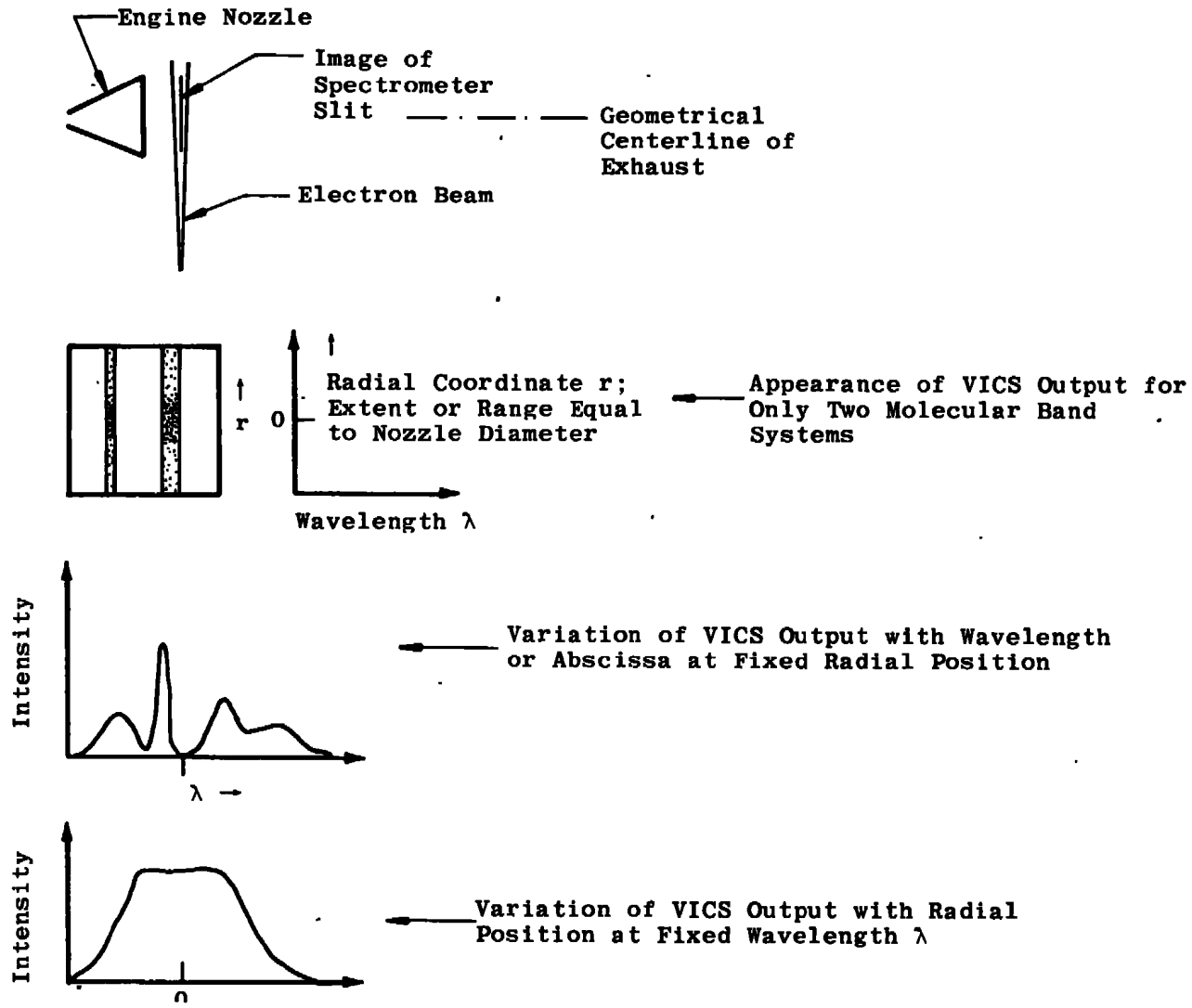

Figure 15. VICS output at one axial location.

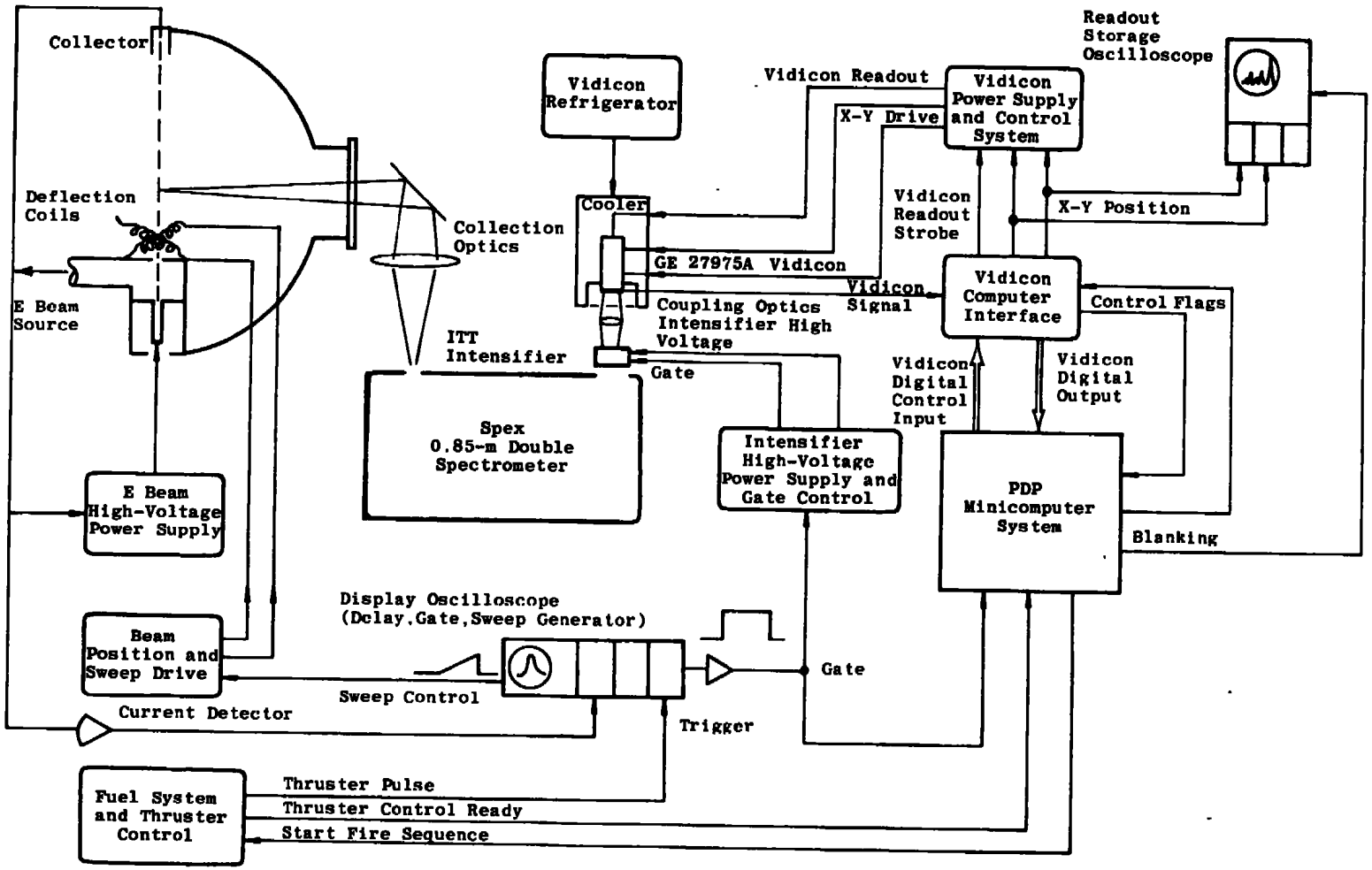

Figure 16. Block diagram of the basic instrument system for the electron beam forward-flow measurements.

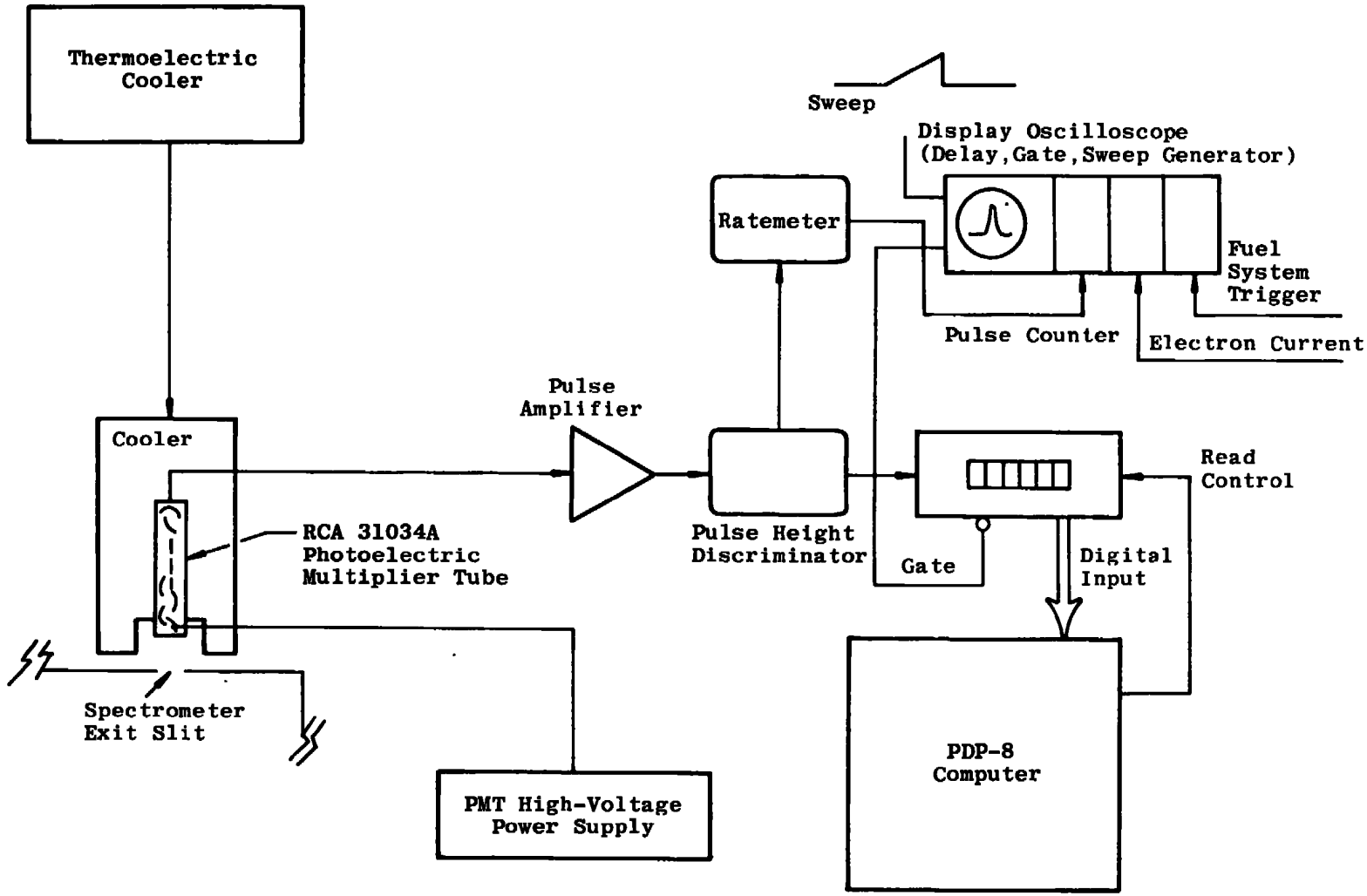

Figure 17. Block diagram of spectrometer detector system for electron beam PMT measurements.

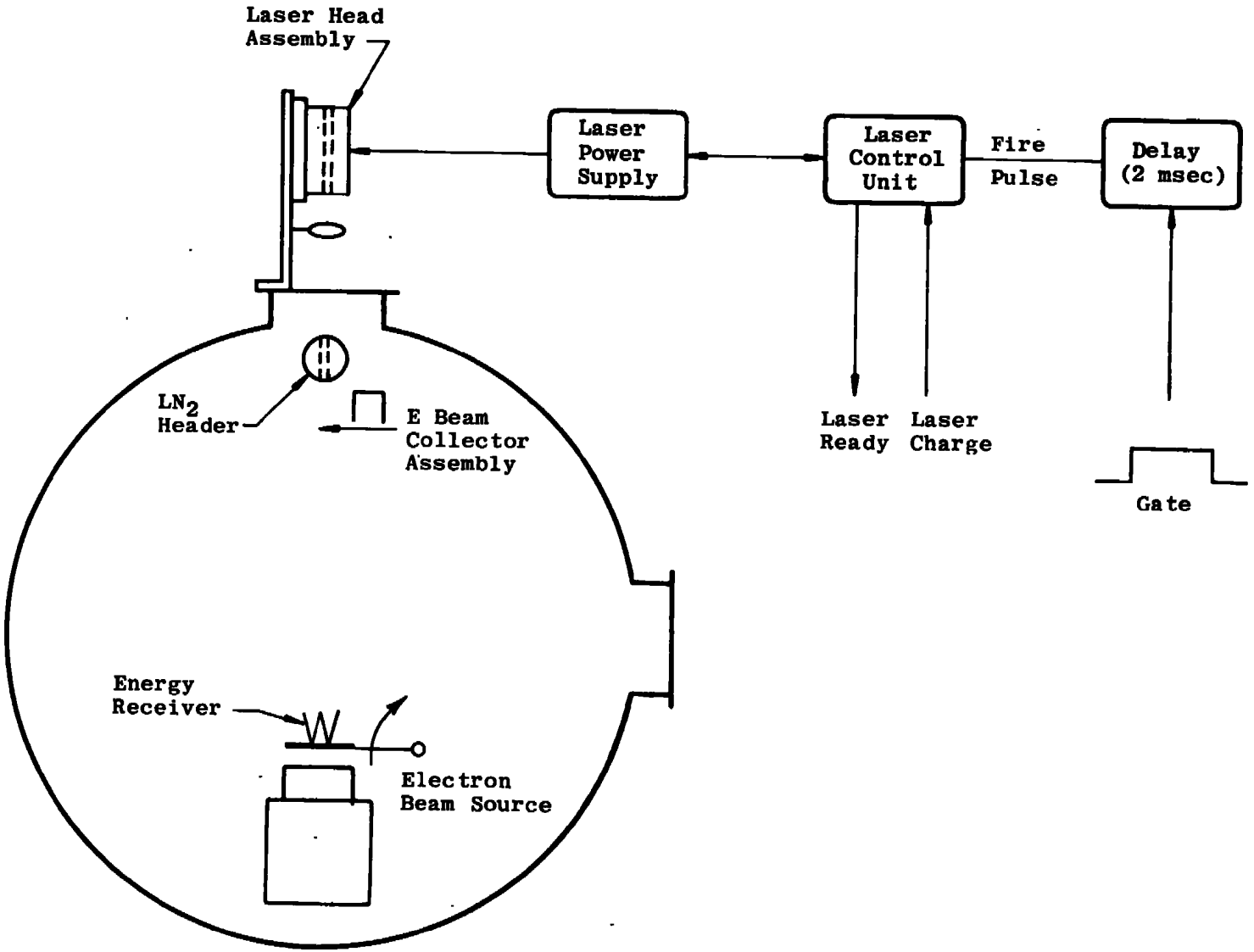

Figure 18. Block diagram of laser and associated components for light scattering measurements.

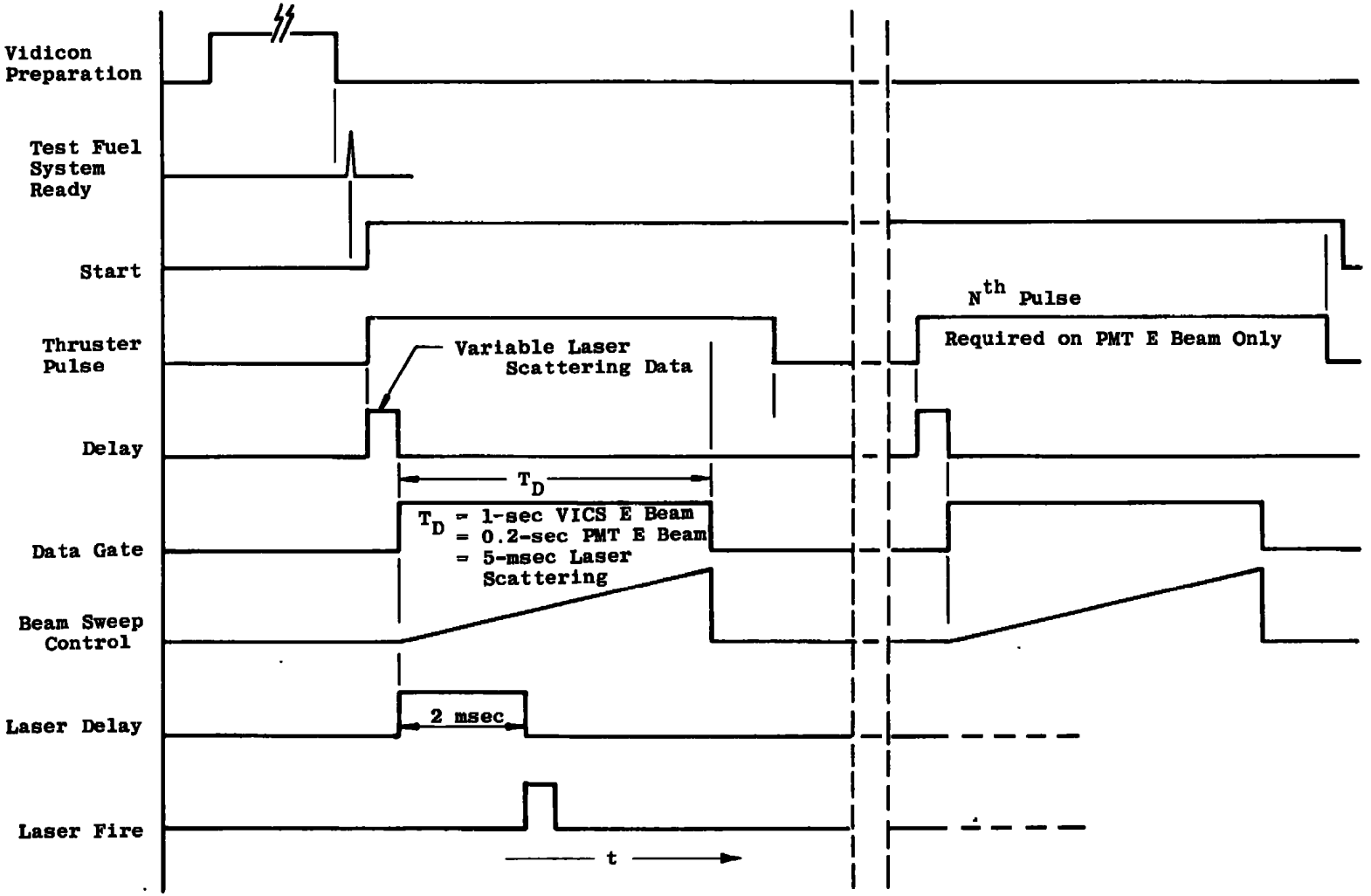

Figure 19. Timing diagram for data acquisition sequence.

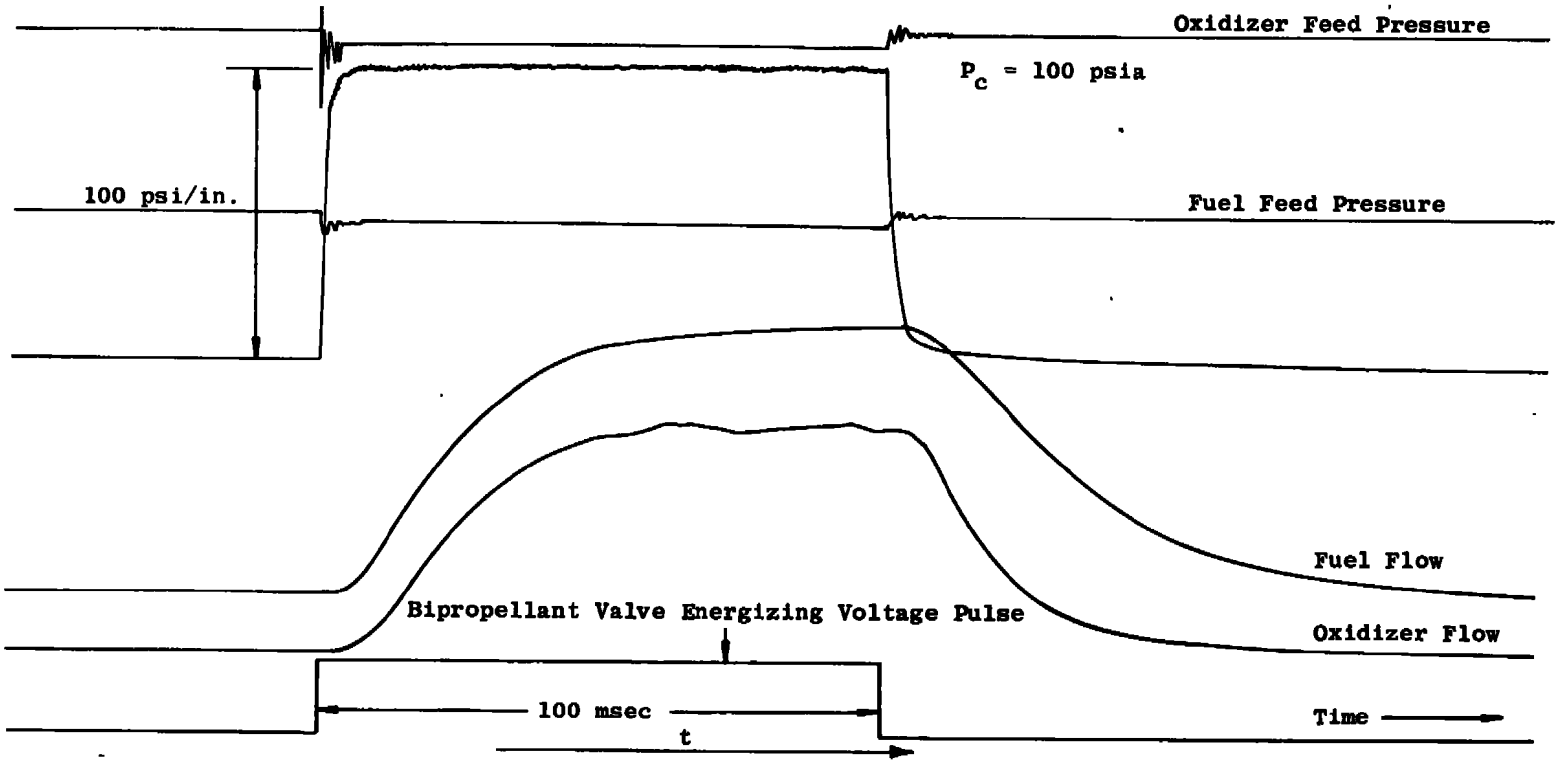

Figure 20. Typical engine firing trace.

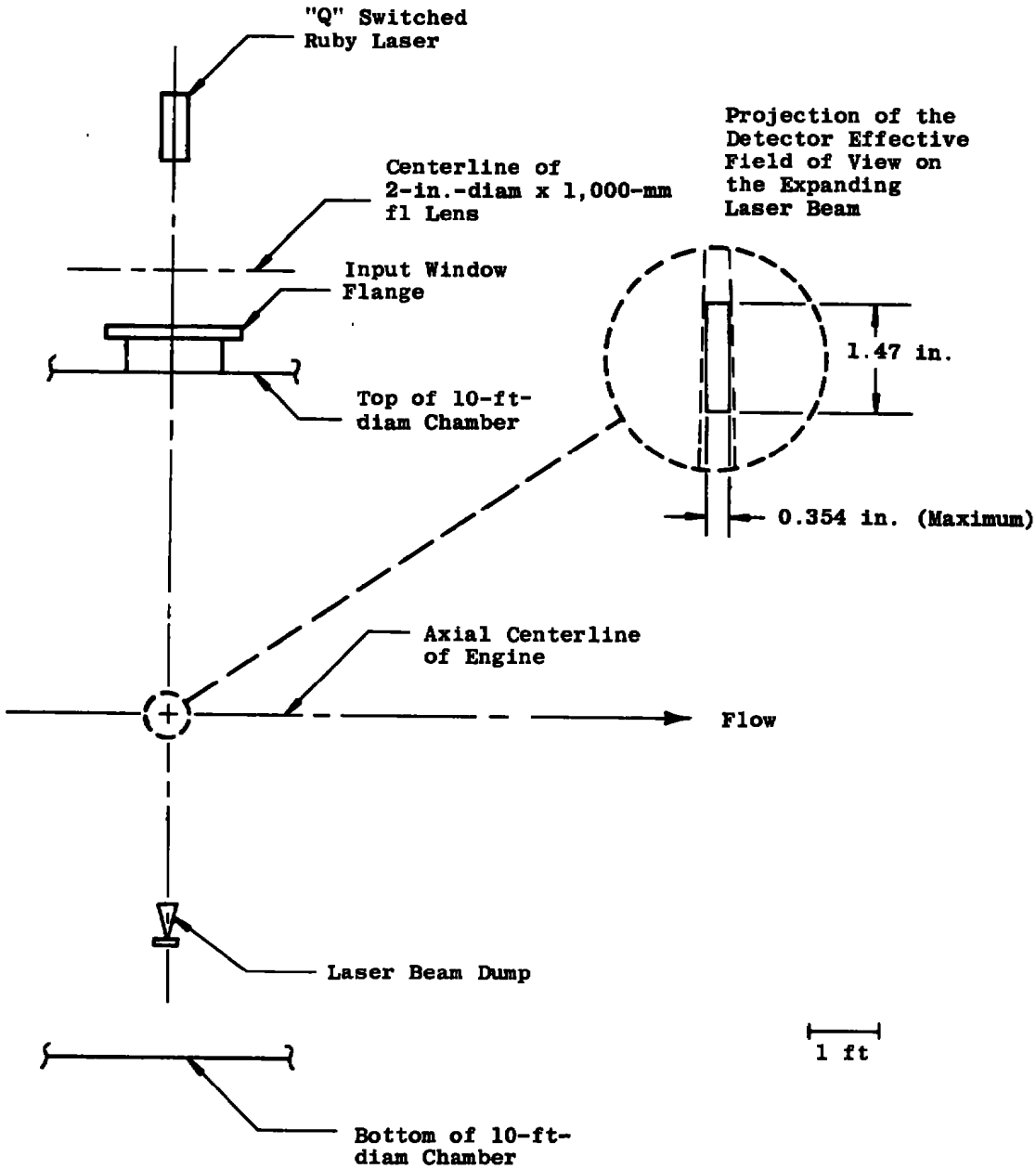

Figure 21. Schematic diagram of laser beam injection scheme.

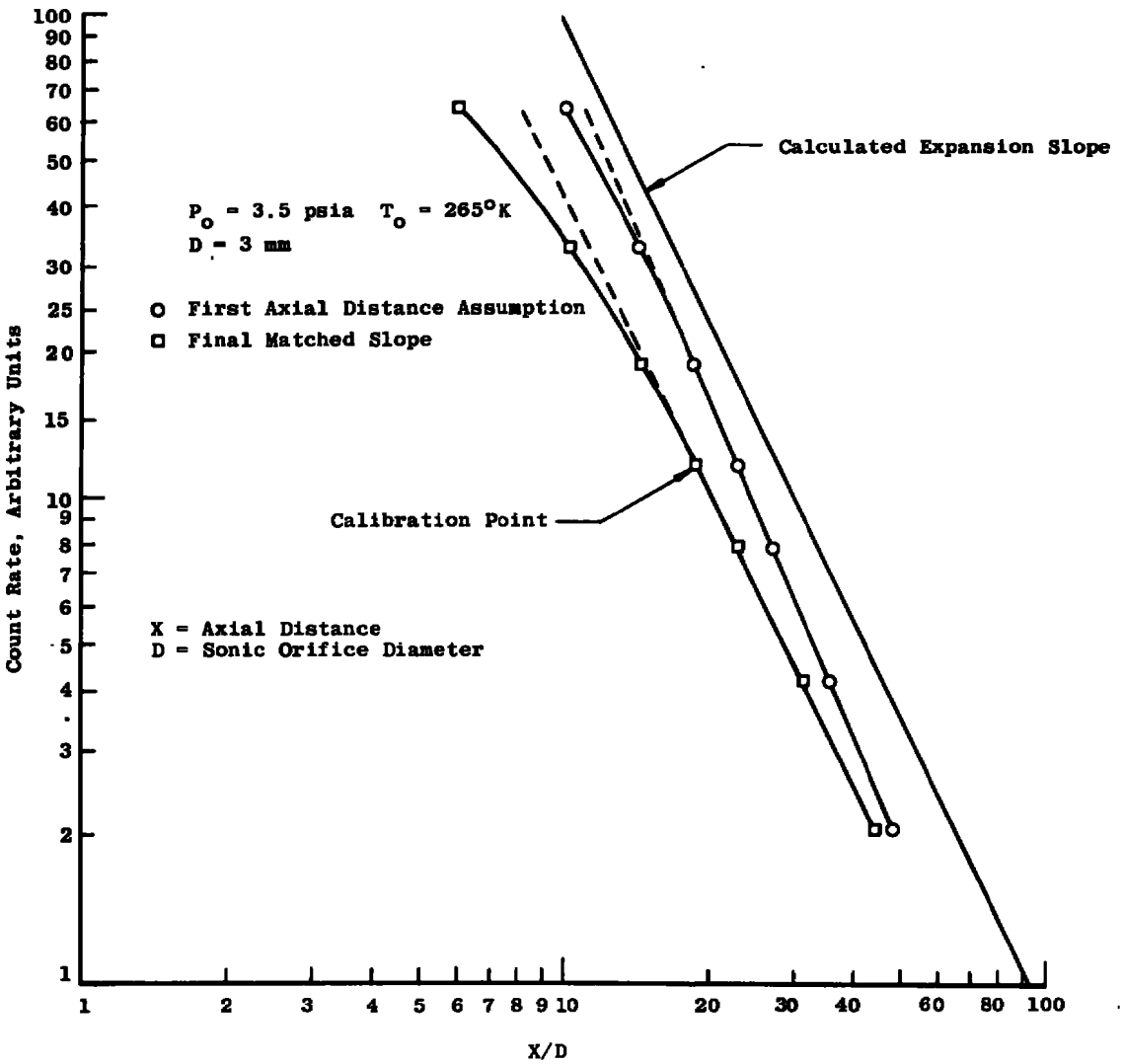

Figure 22. Sonic orifice axial scan.

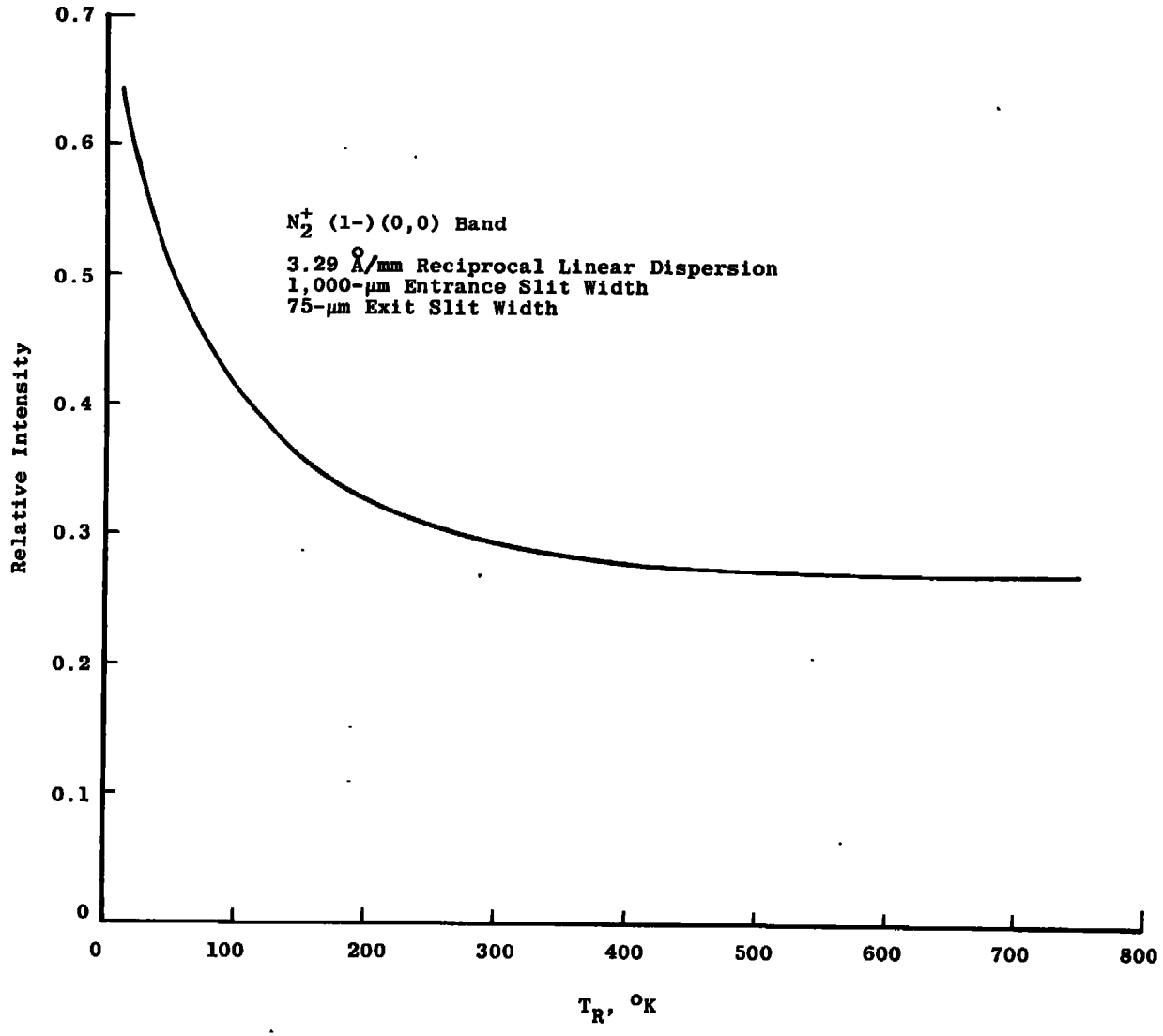

Figure 23. Relative intensity of N_2^+ (1-) (0,0) band at 3912.00 Å versus rotational temperature.

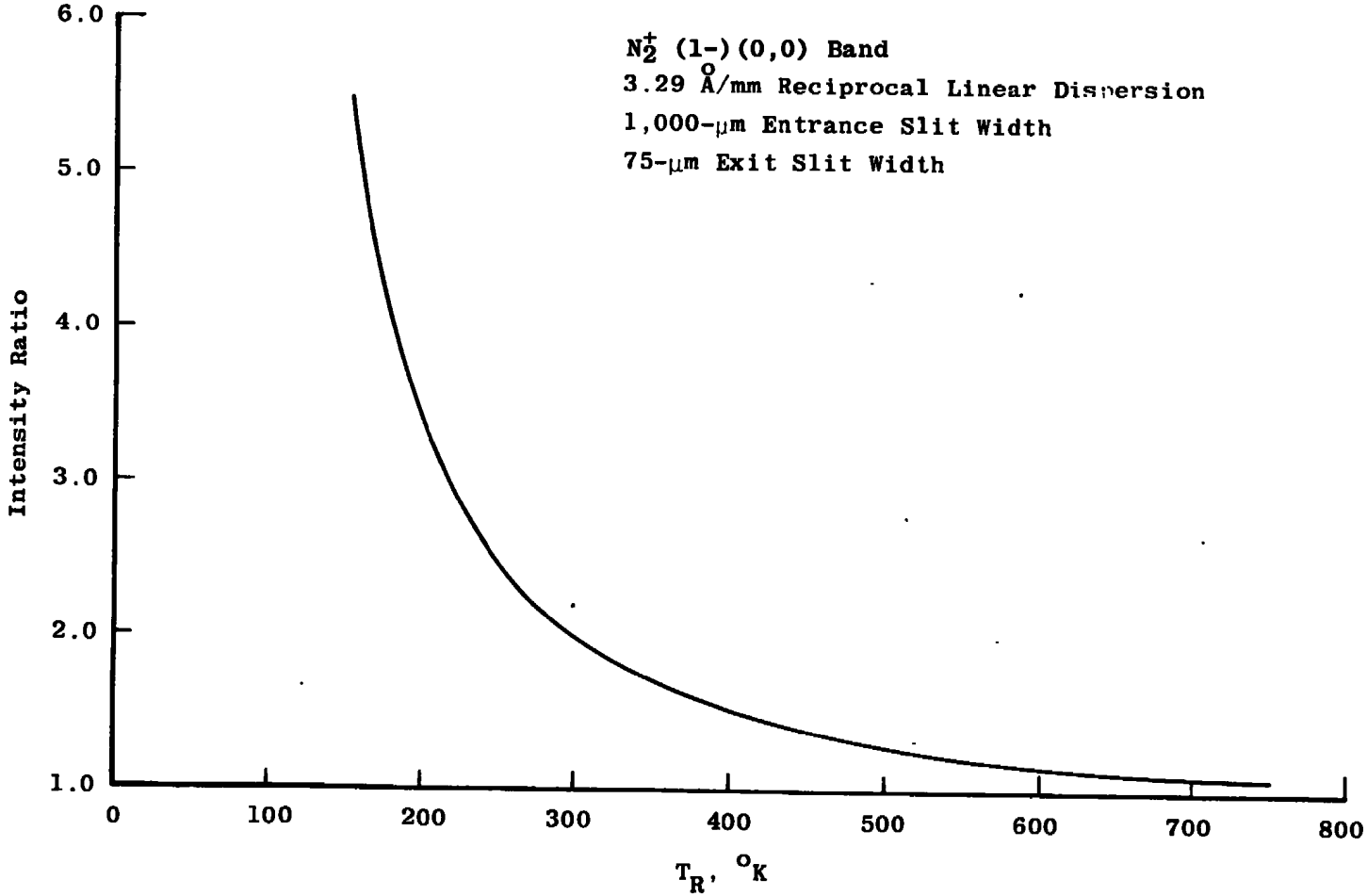

Figure 24. Ratio of intensities at 3905.25 Å and 3899.00 Å versus rotational temperature.

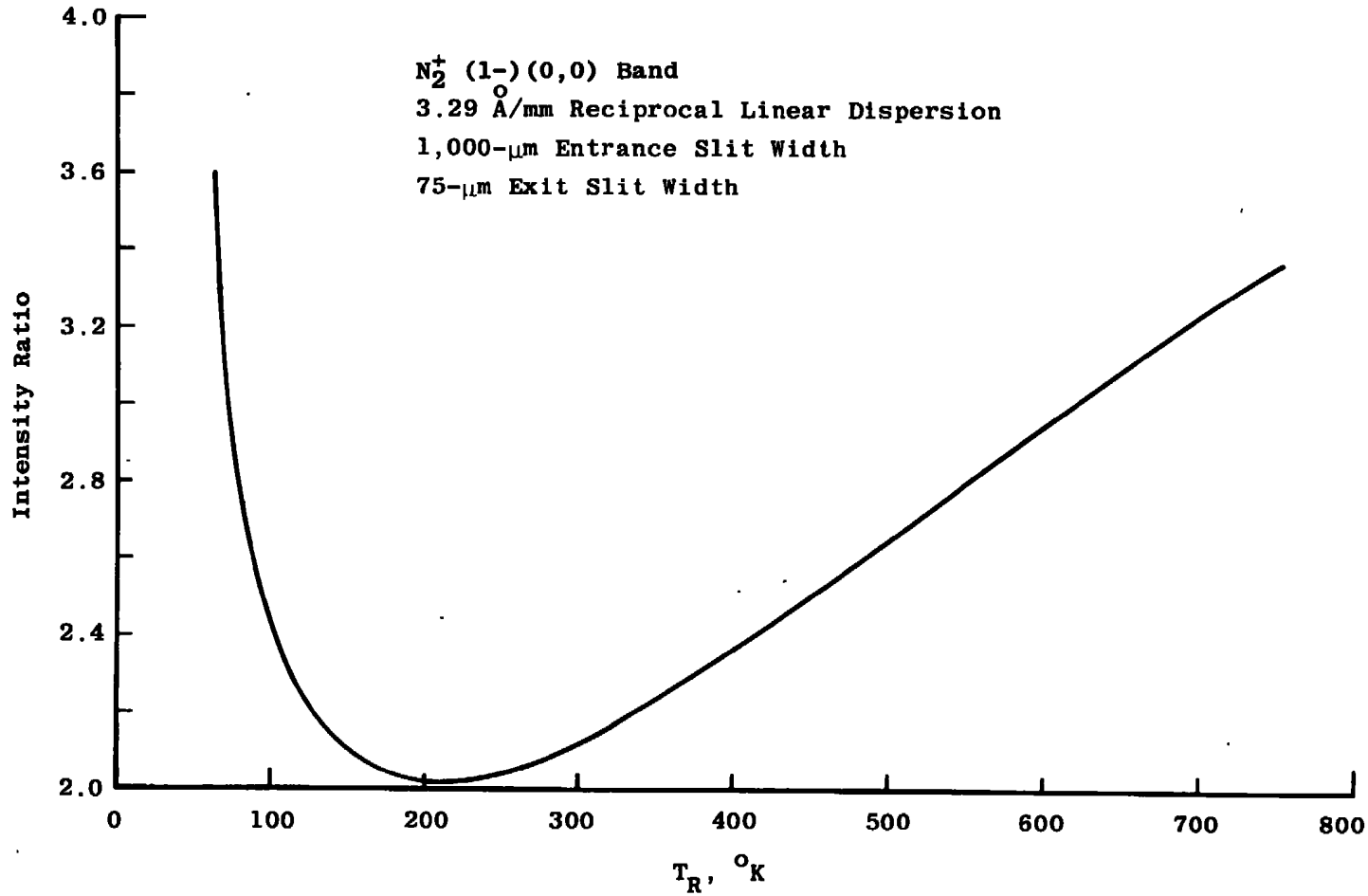

Figure 25. Ratio of intensities at 3912.00 Å and 3905.25 Å versus rotational temperature.

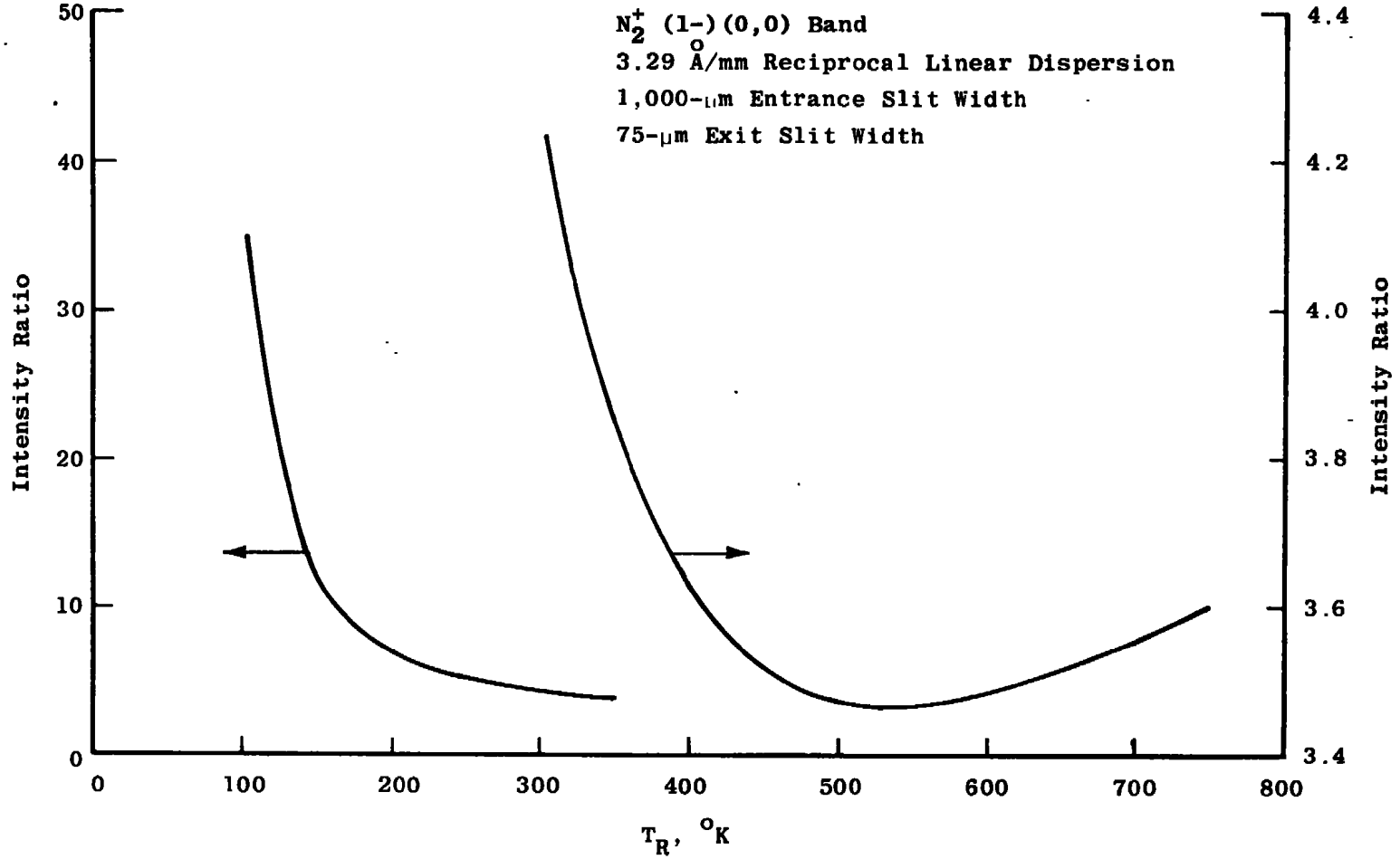

Figure 26. Ratio of intensities at 3912.00 Å and 3899.00 Å versus rotational temperature.

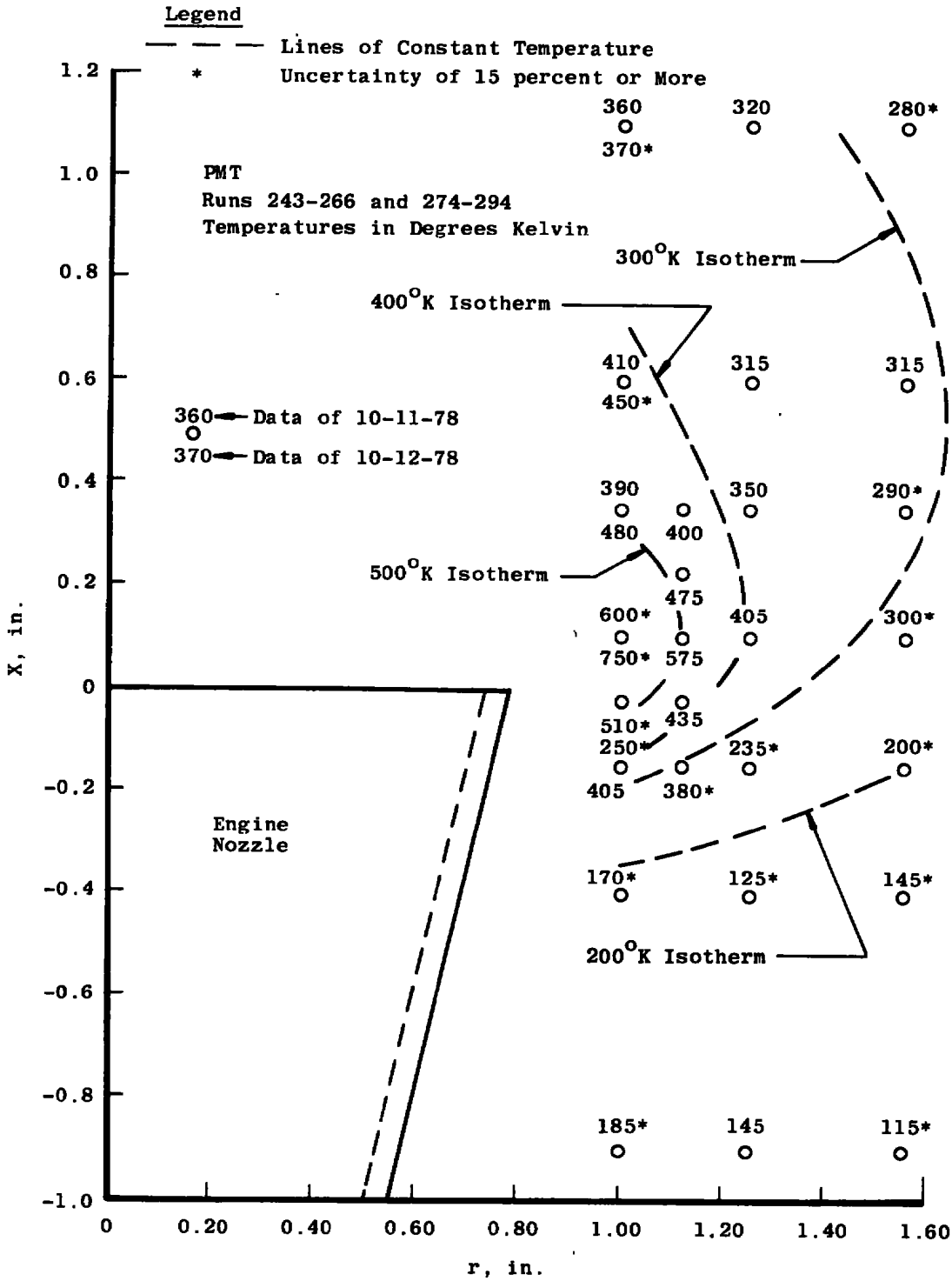

Figure 27. PMT rotational temperature in back-flow region.

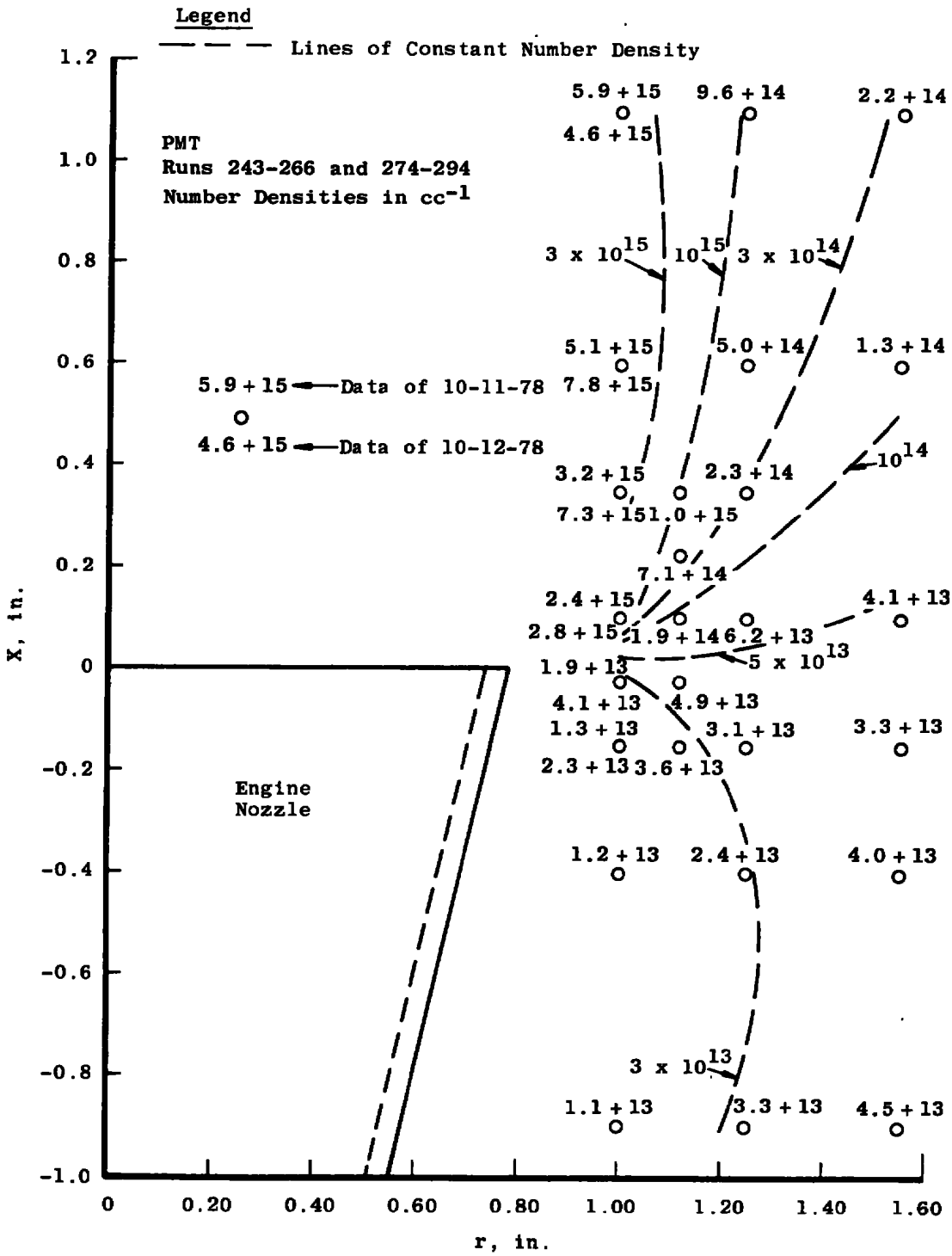

Figure 28. PMT nitrogen number densities in back-flow region.

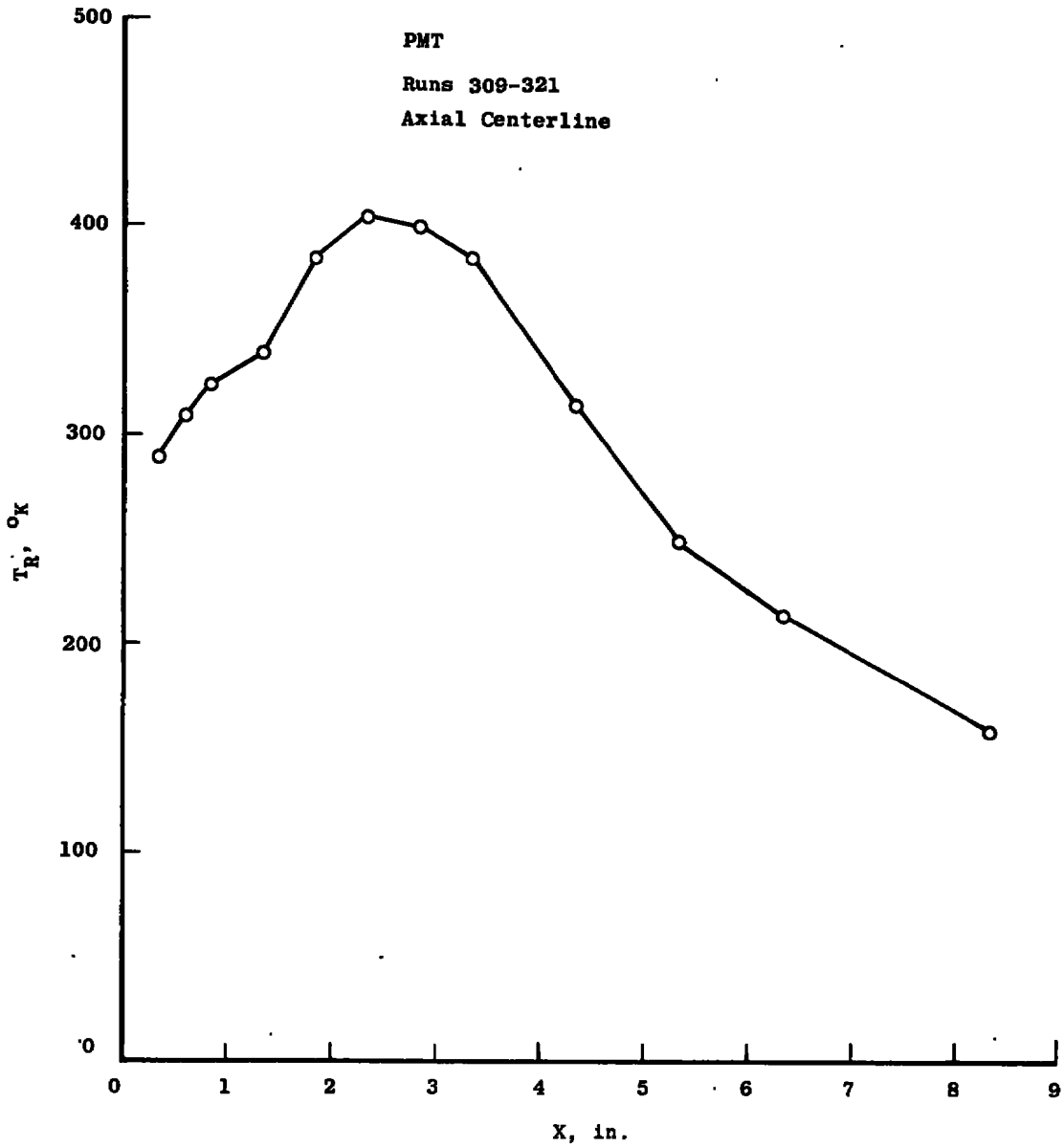

Figure 29. PMT axial centerline rotational temperatures in forward-flow region.

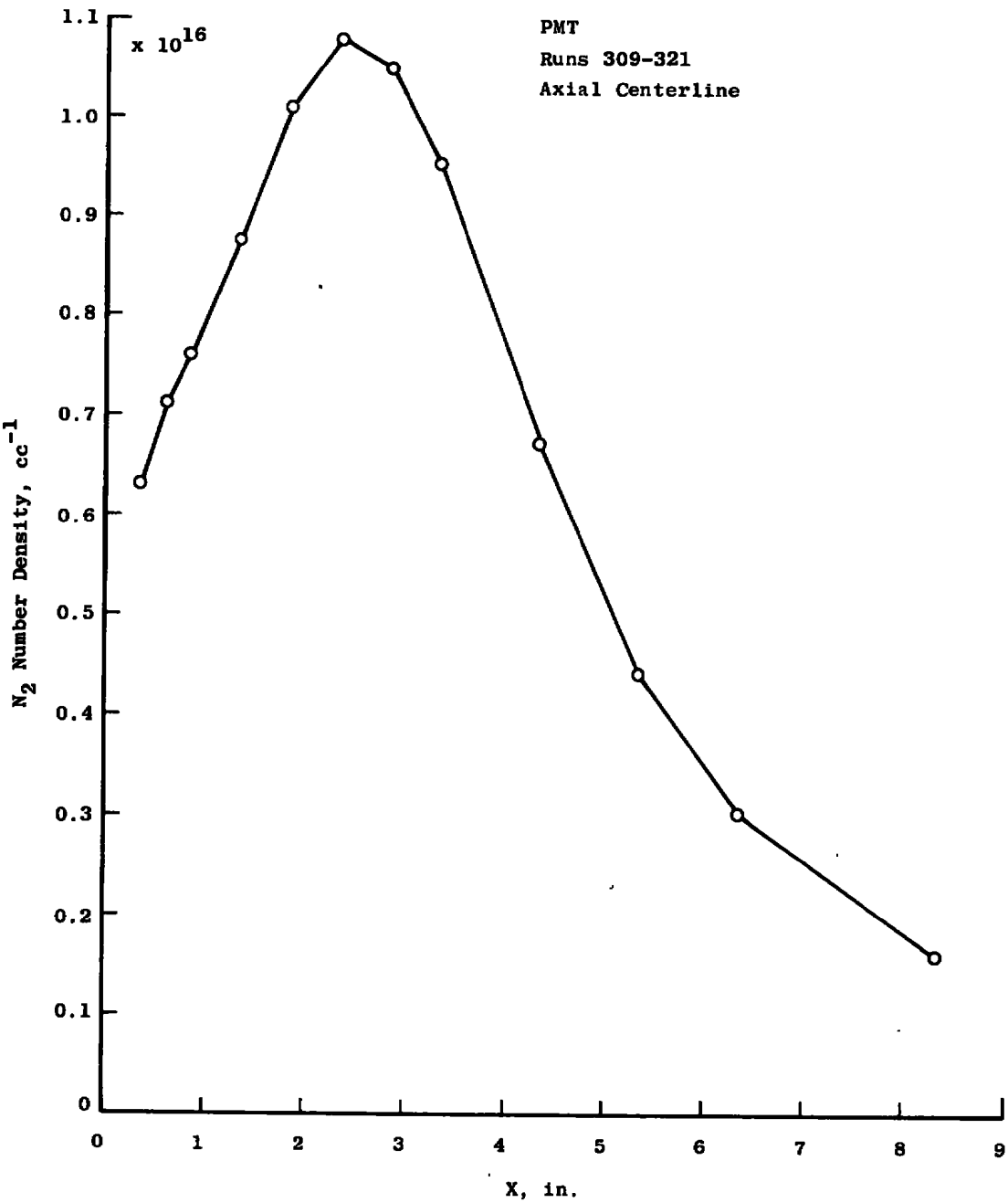

Figure 30. PMT axial centerline nitrogen number densities in forward-flow region.

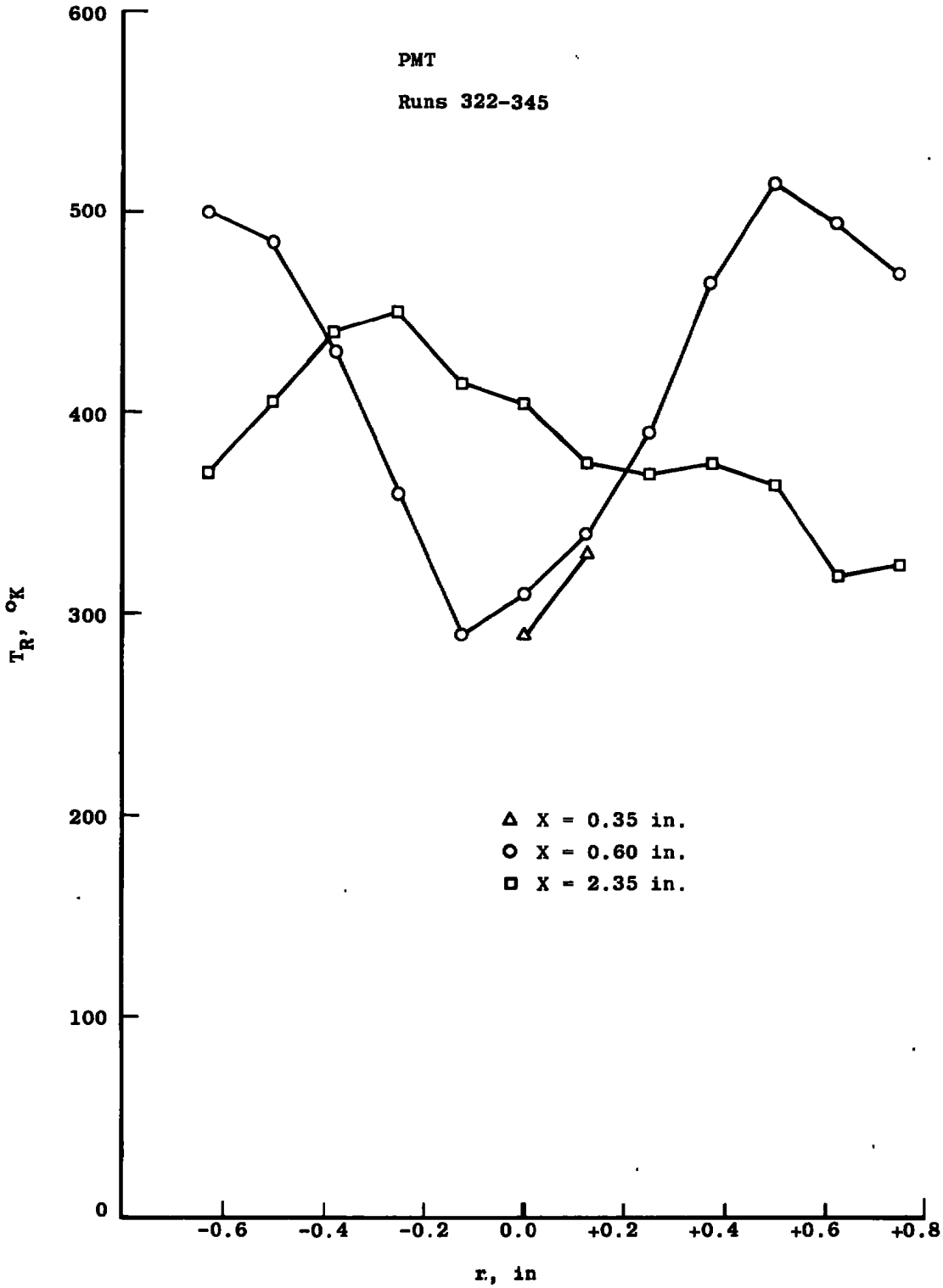

Figure 31. PMT radial profiles of rotational temperature in forward-flow region.

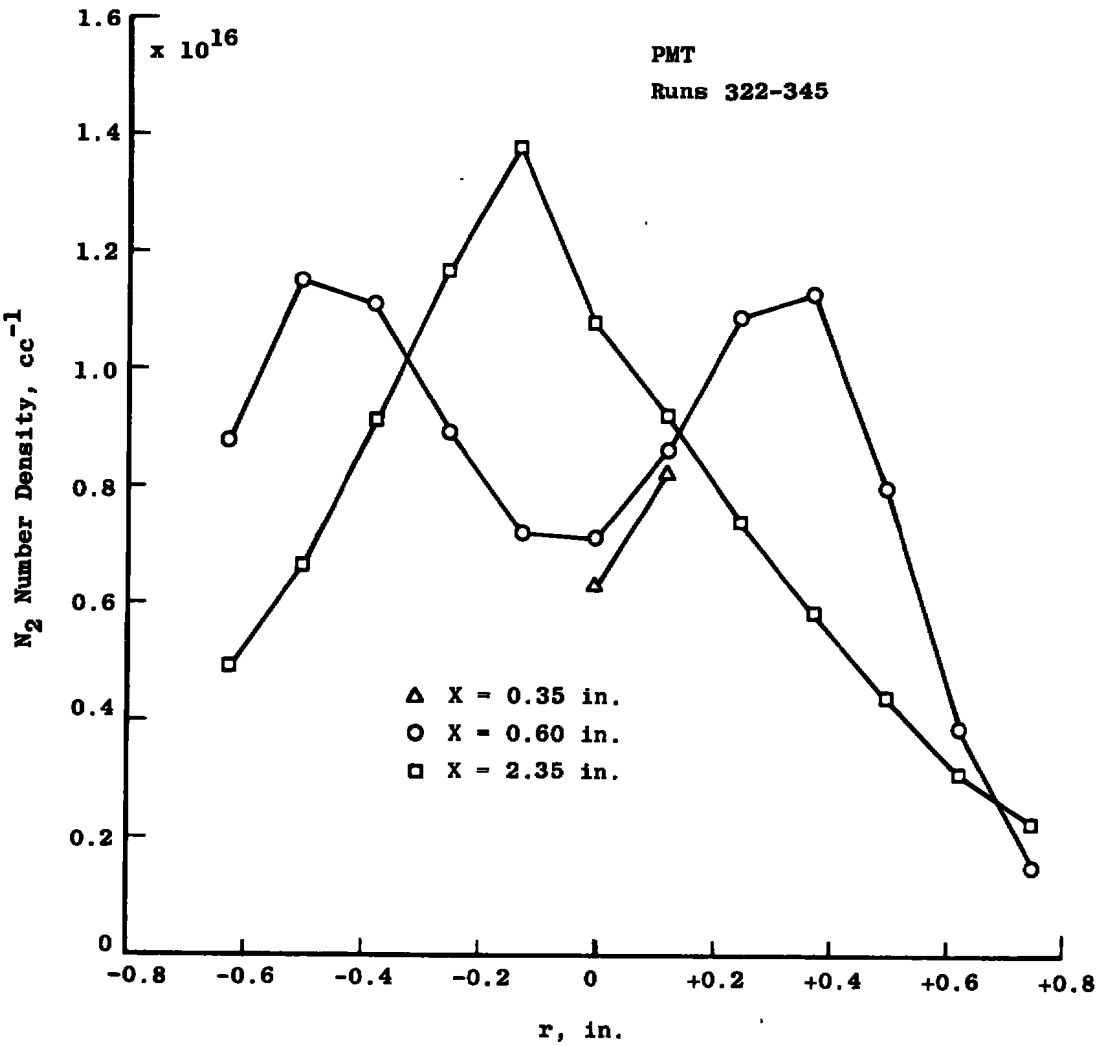

Figure 32. PMT radial profiles of nitrogen number density in forward-flow region.

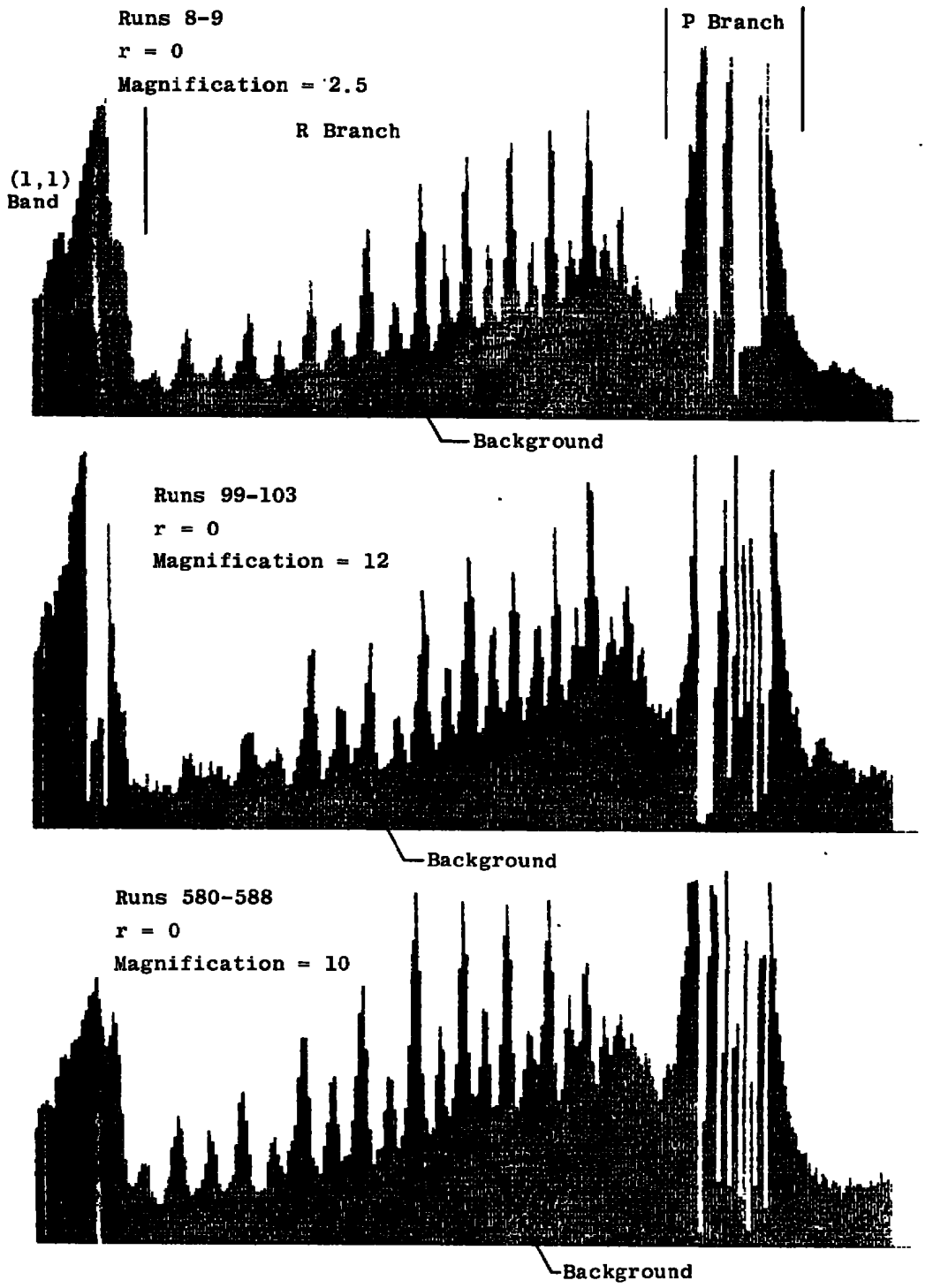

Figure 33. VICS resolved N_2^+ (1-) (0,0) spectra of engine.

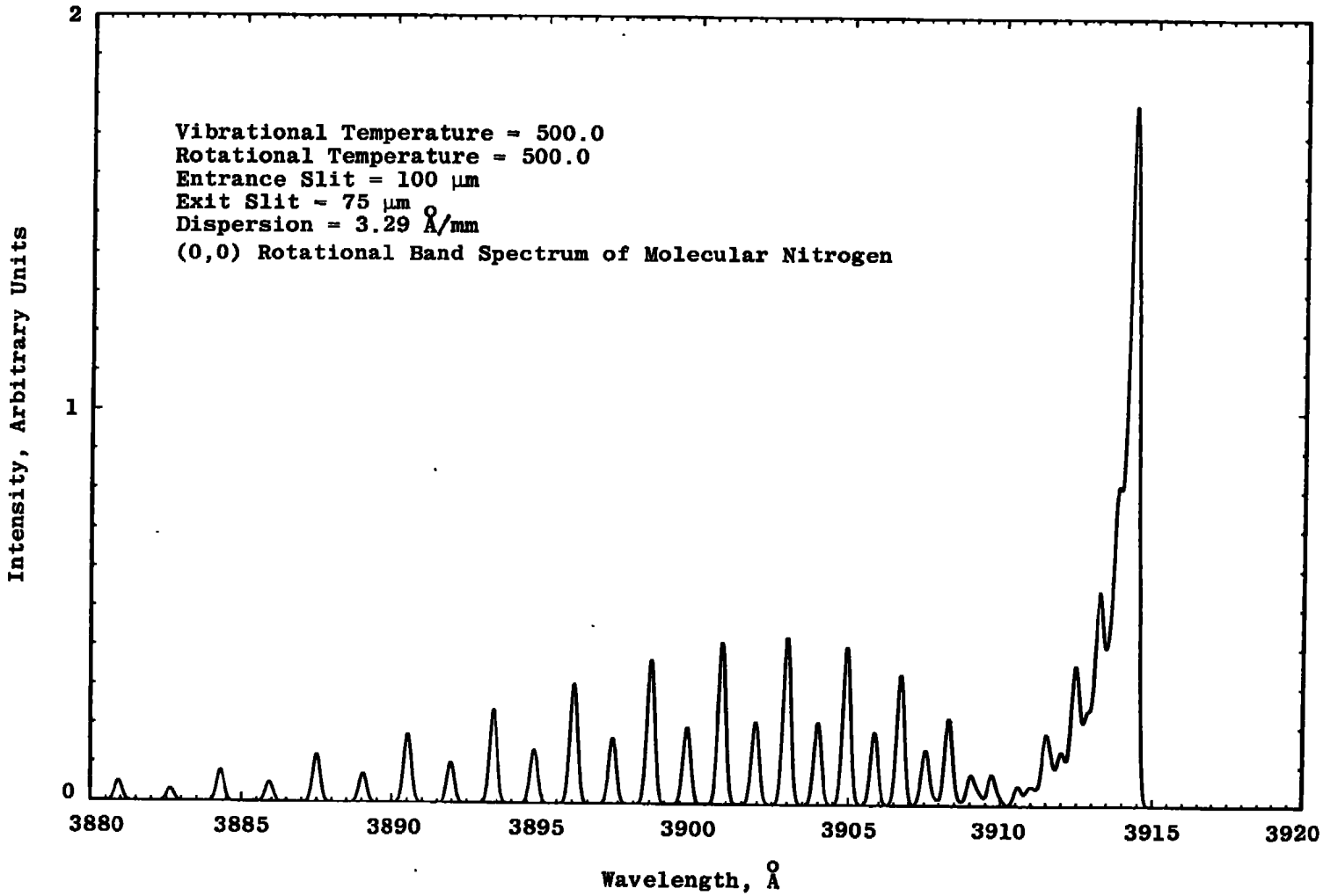

Figure 34. Computer-calculated resolved spectrum of N_2^+ (1-) (0,0) band.

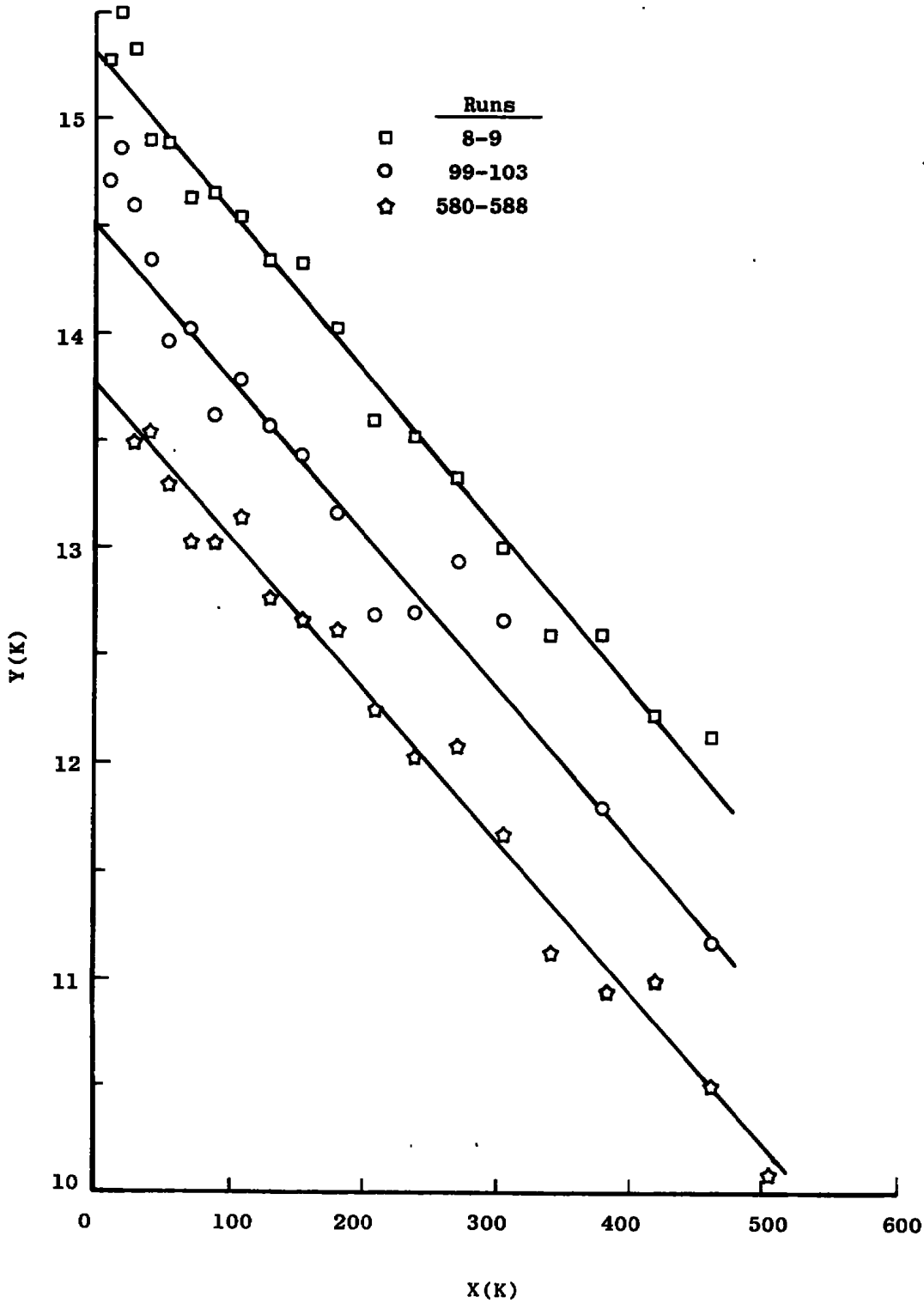

Figure 35. Boltzmann plots of the sample spectra.

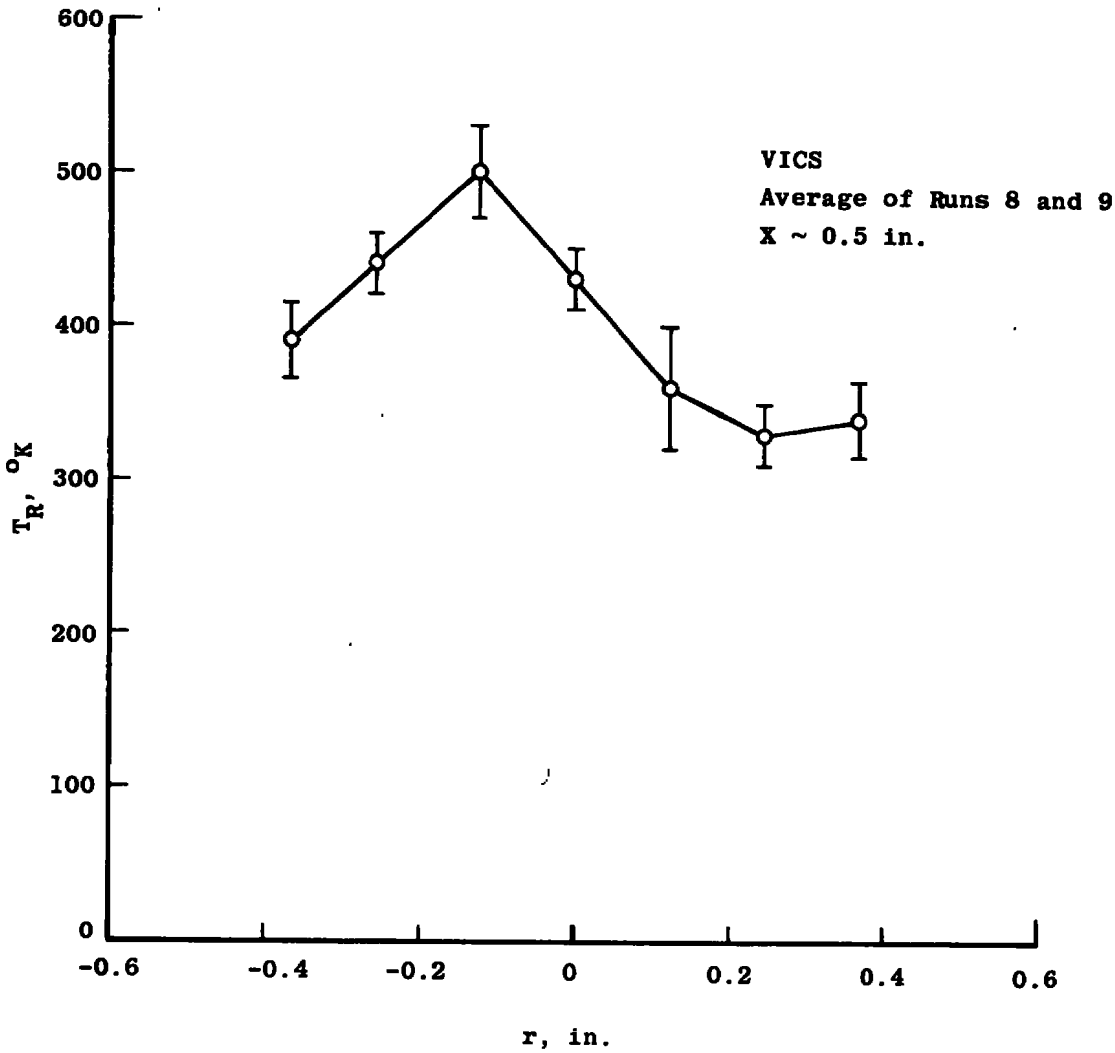

a. X ~ 0.5 in.

Figure 36. VICS radial profiles of rotational temperature in forward-flow region.

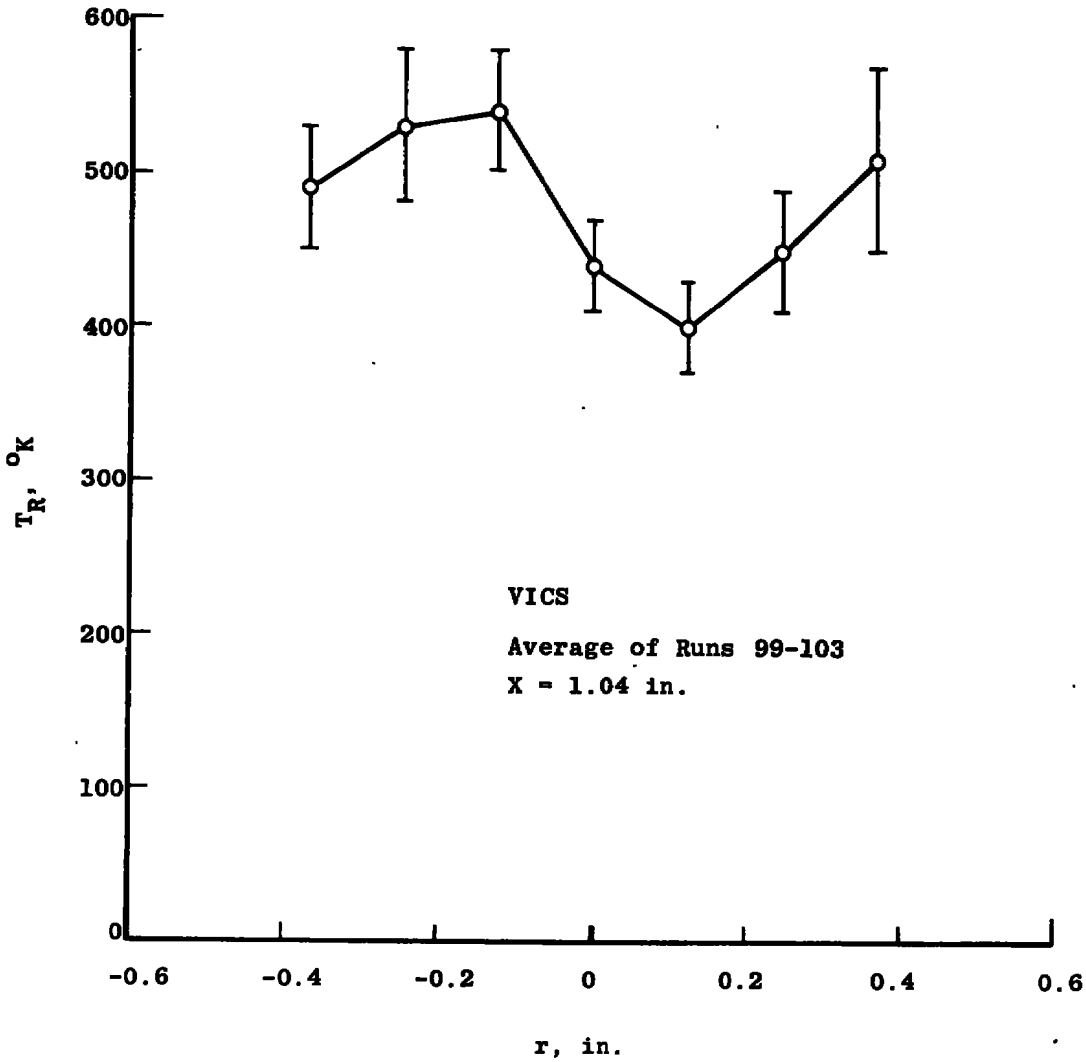

b. X = 1.04 in.

Figure 36. Continued.

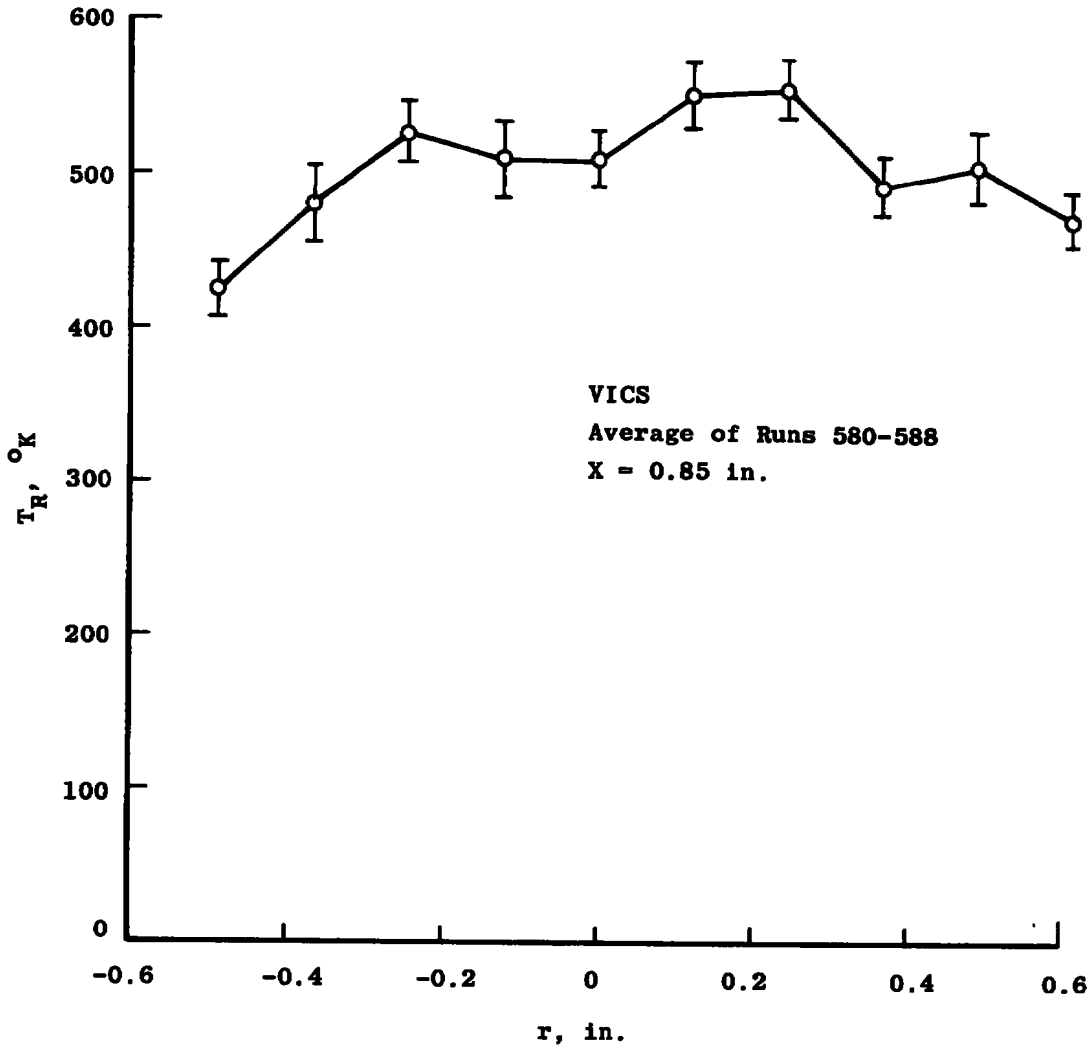

c. X = 0.85 in.

Figure 36. Concluded.

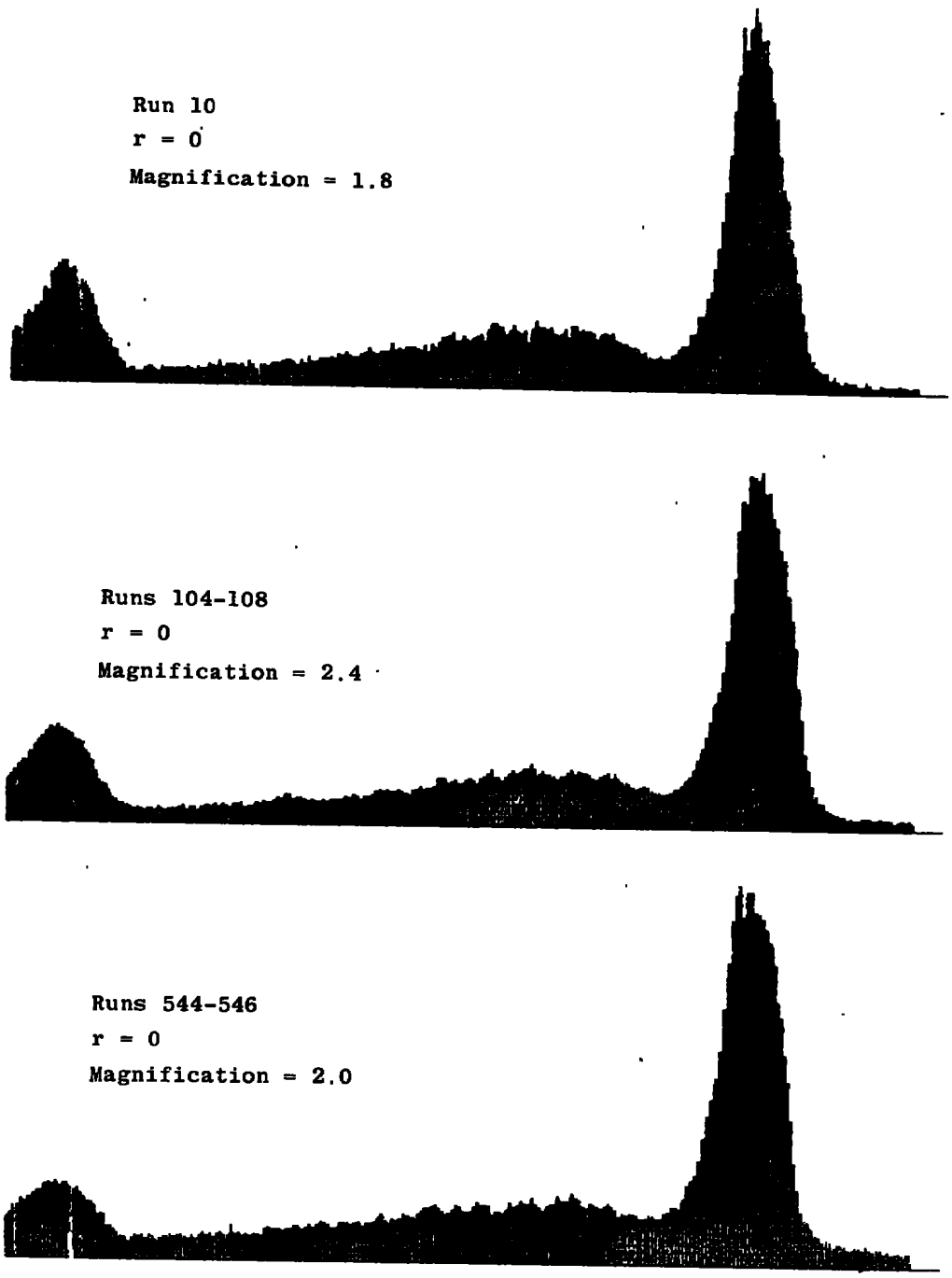

Figure 37. VICS unresolved N_2^+ (1-) (0,0) spectra of engine.

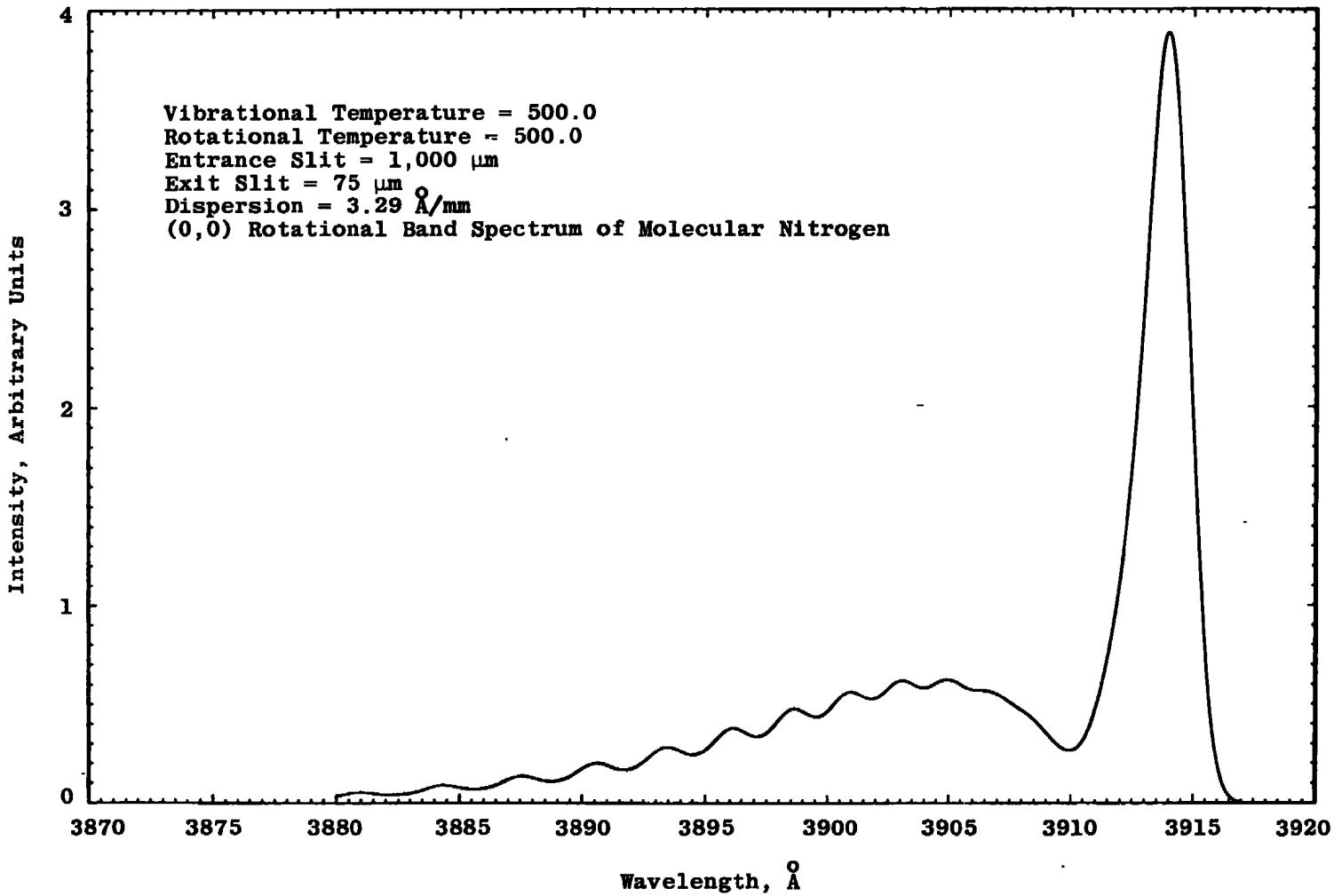

Figure 38. Computer-calculated unresolved spectrum of N_2^+ (1-) (0,0) band.

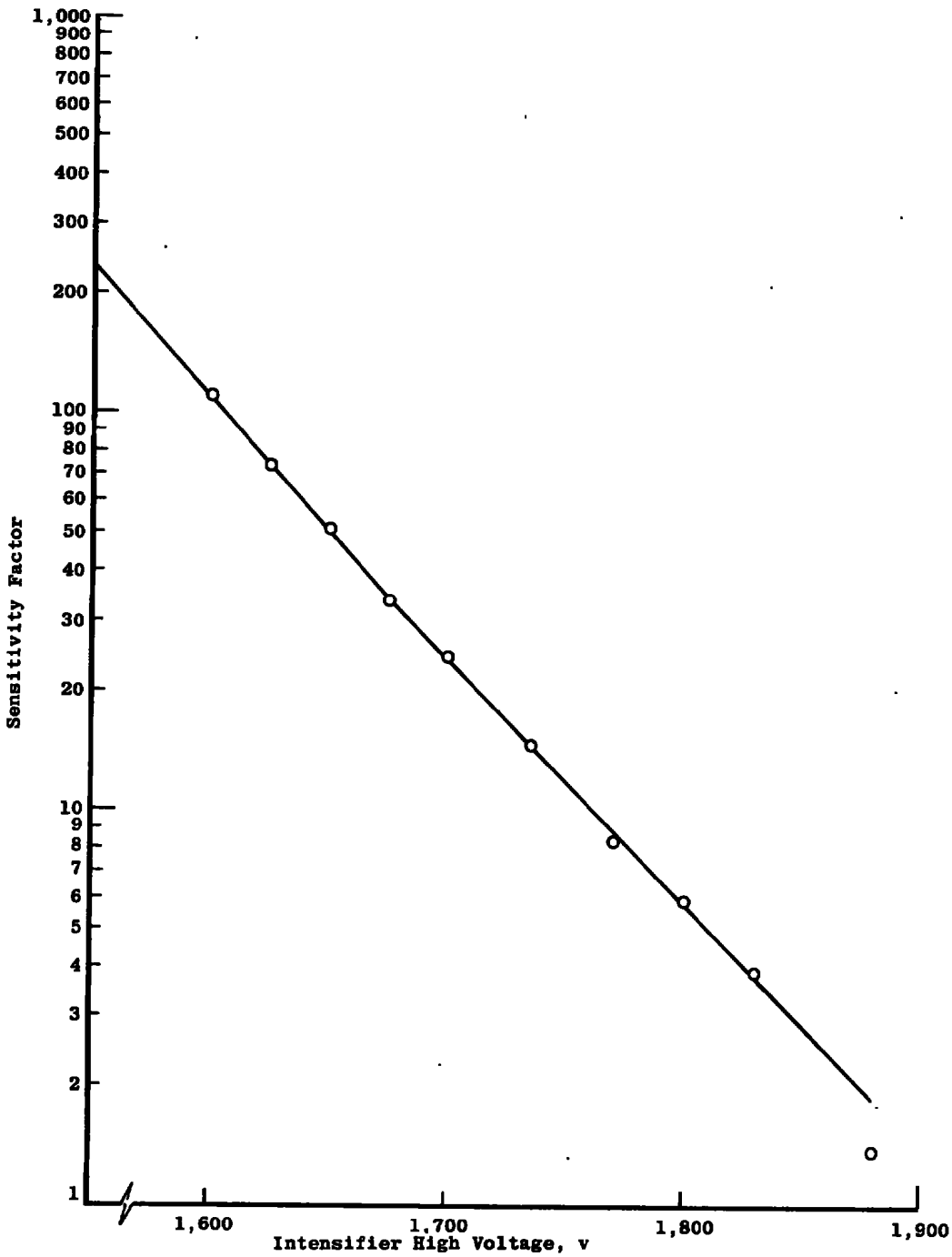

Figure 39. Intensifier high-voltage sensitivity factors.

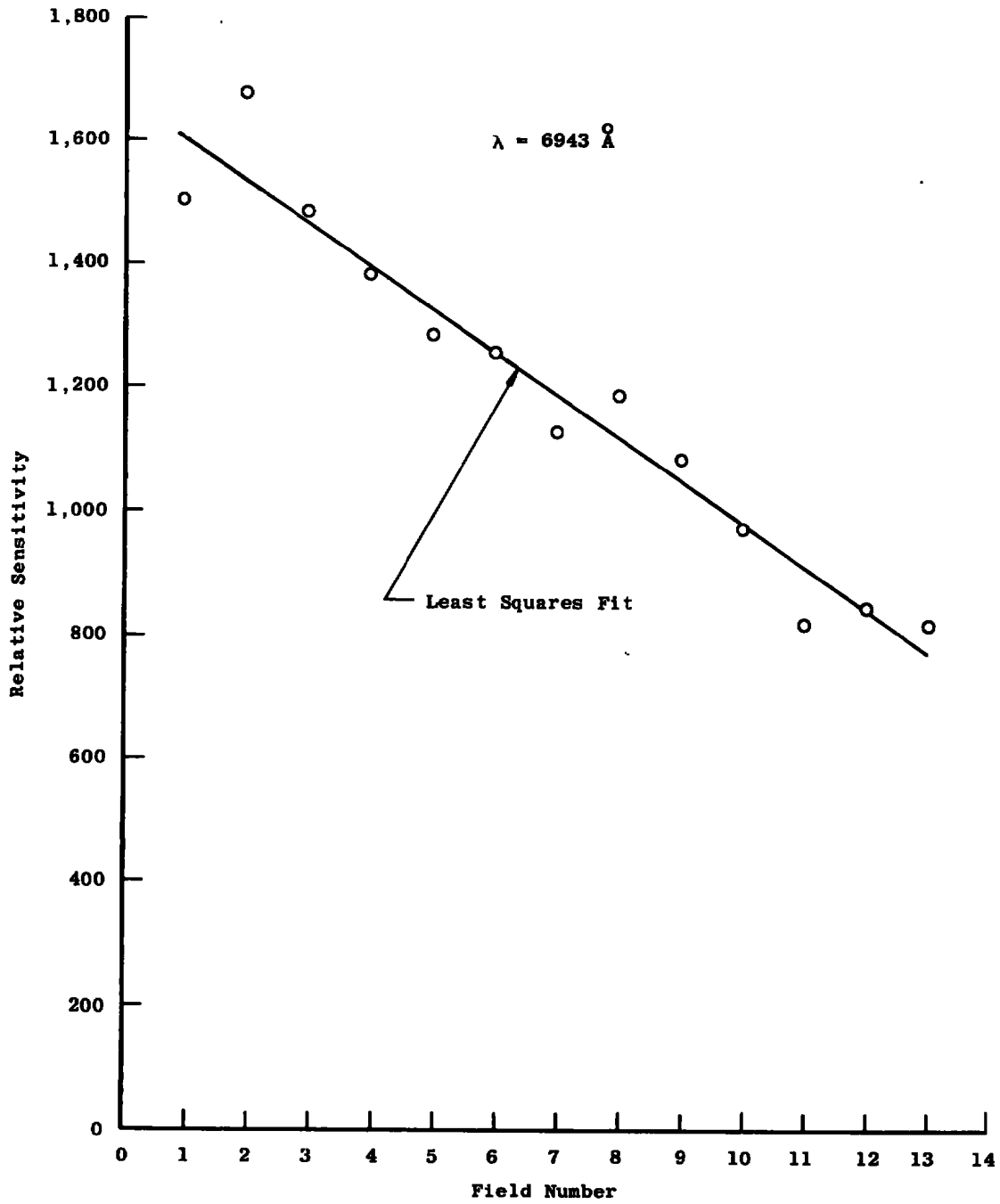

Figure 40. Relative sensitivity of intensifier fields.

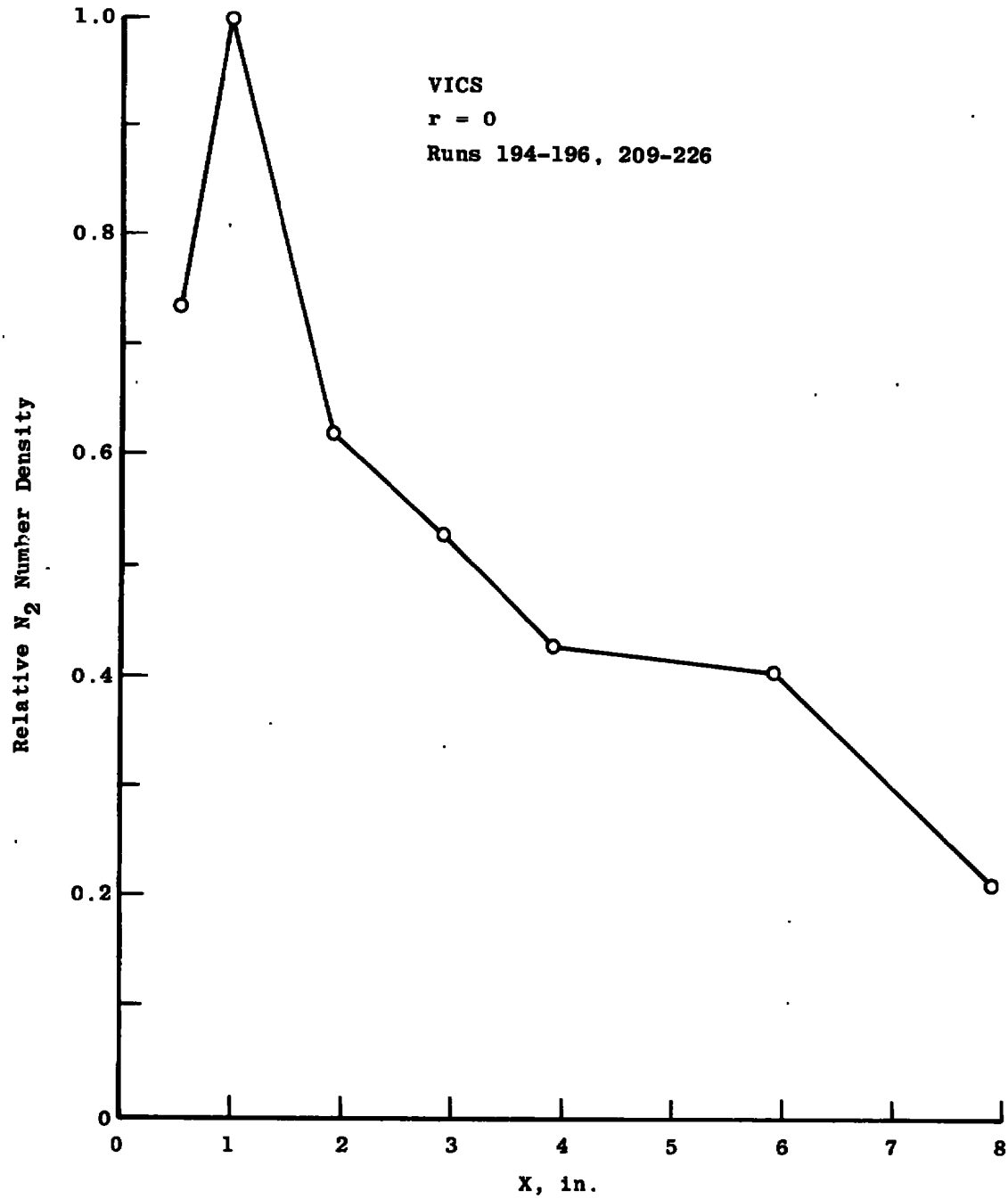

a. First determination

Figure 41. VICS axial centerline relative nitrogen number densities in forward-flow region.

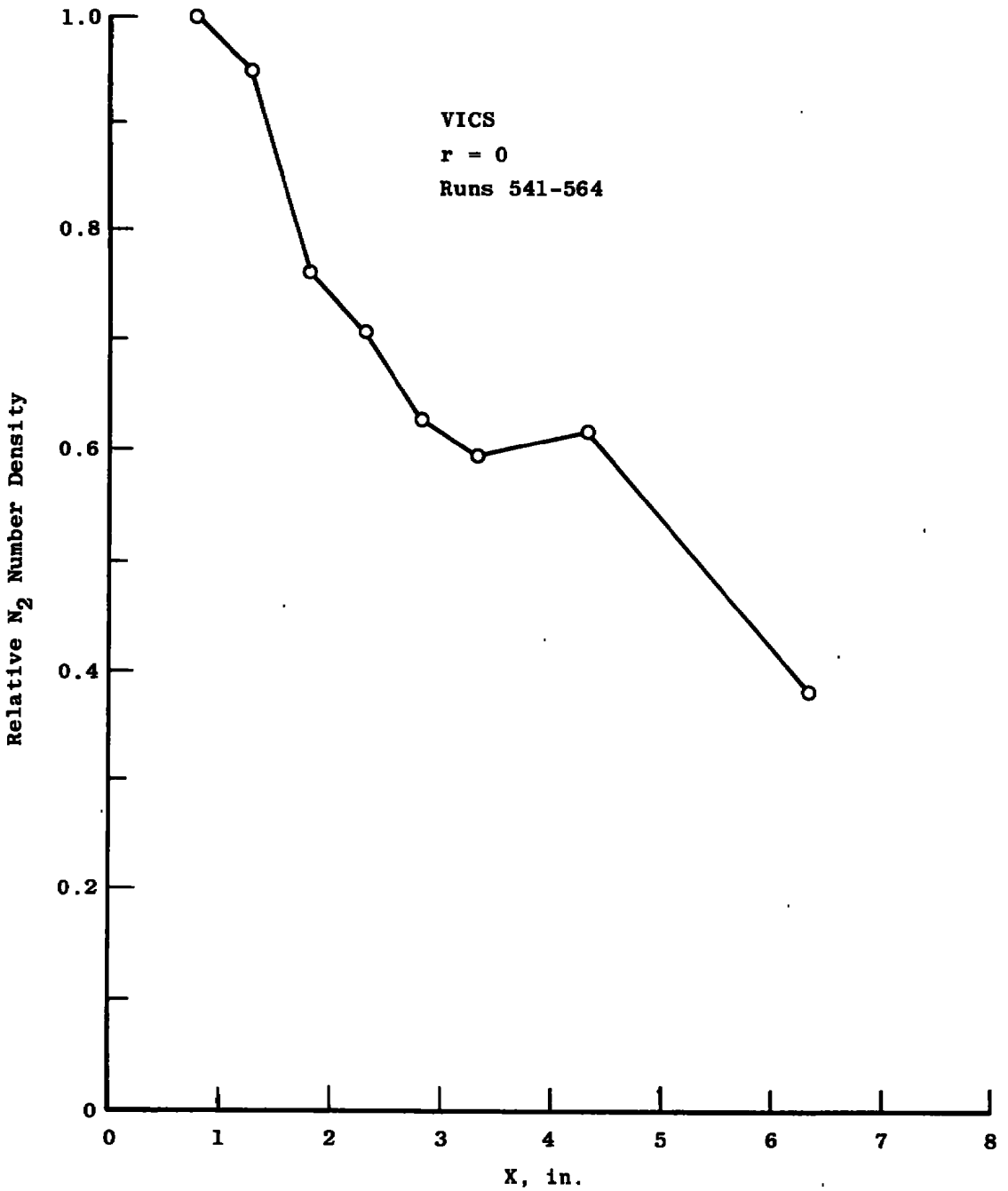

b. Second determination
Figure 41. Concluded.

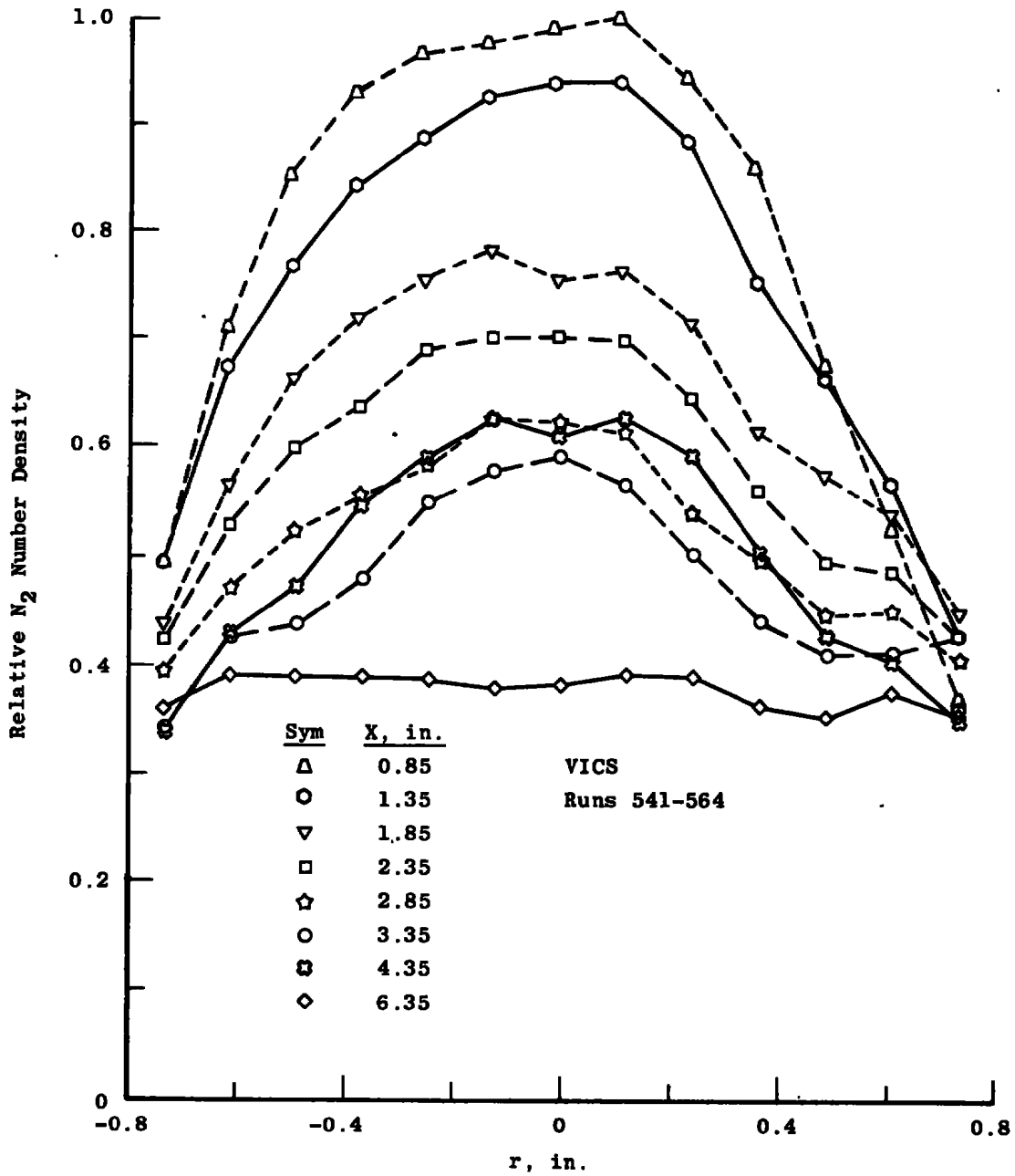

Figure 42. VICS radial profiles of relative nitrogen number densities in forward-flow region.

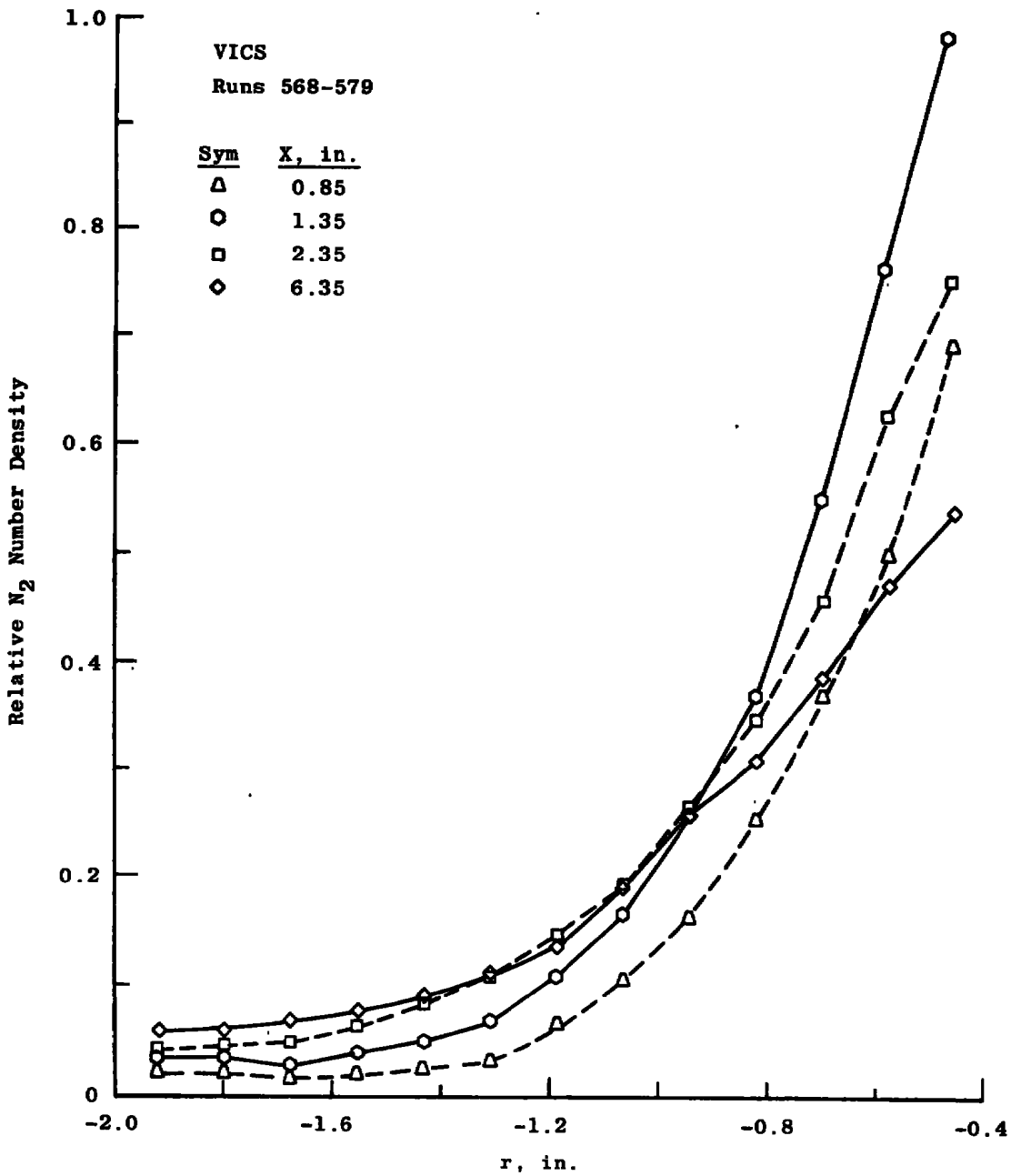

Figure 43. VICS radial profiles of relative nitrogen number densities at large radii in forward-flow region.

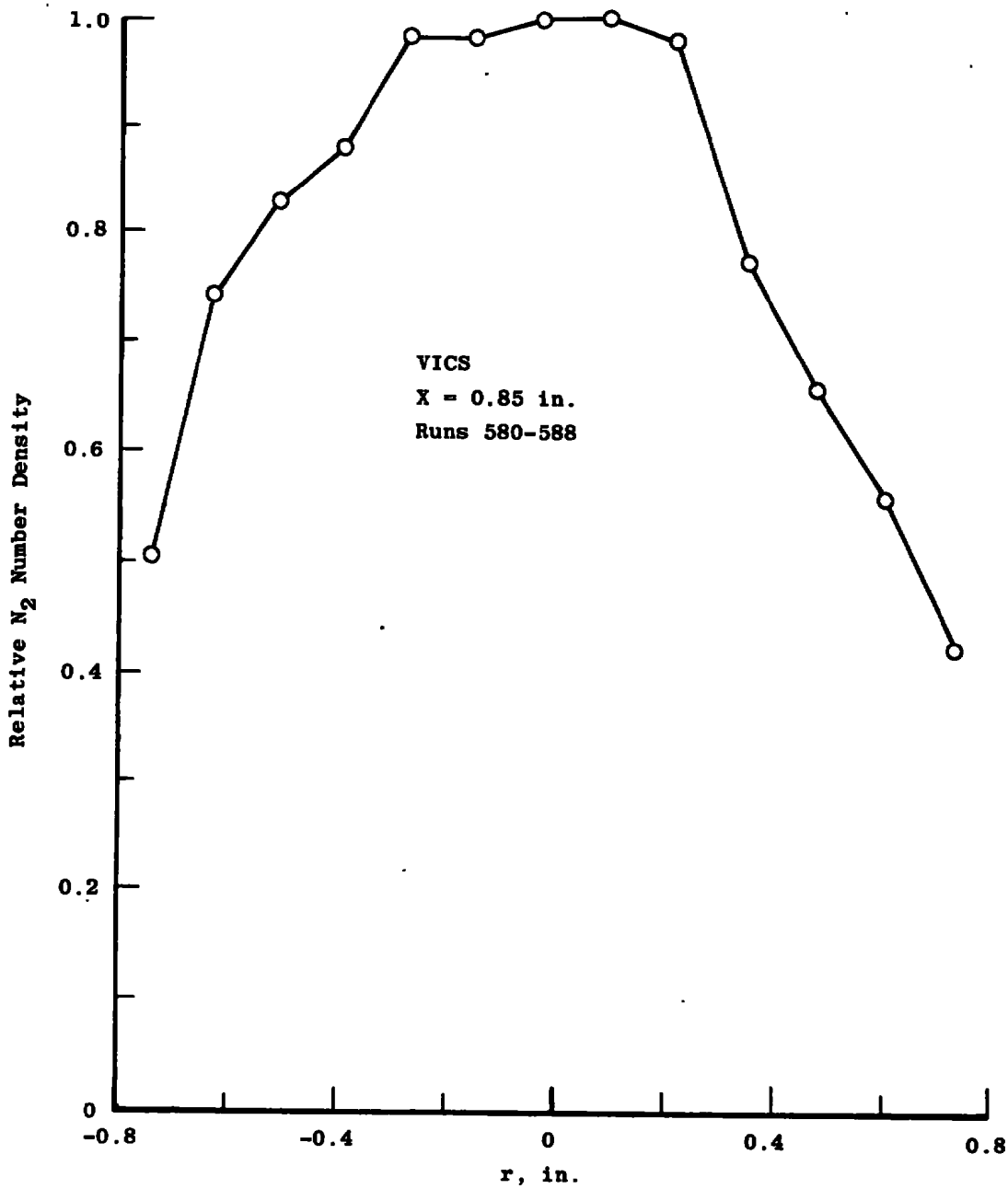

Figure 44. VICS resolved spectra radial profile of relative nitrogen number densities in forward-flow region.

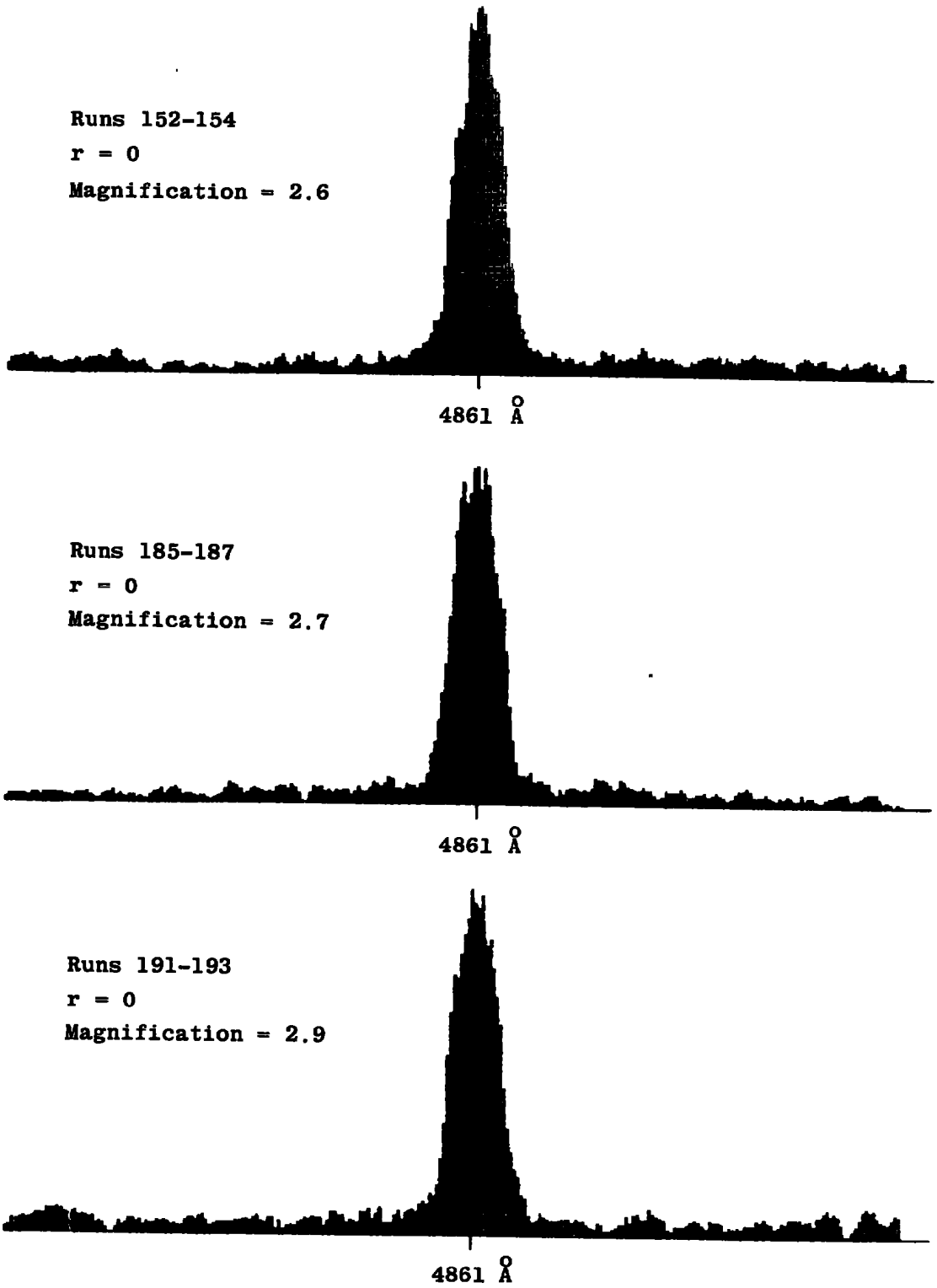

Figure 45. Atomic hydrogen Hβ line spectra.

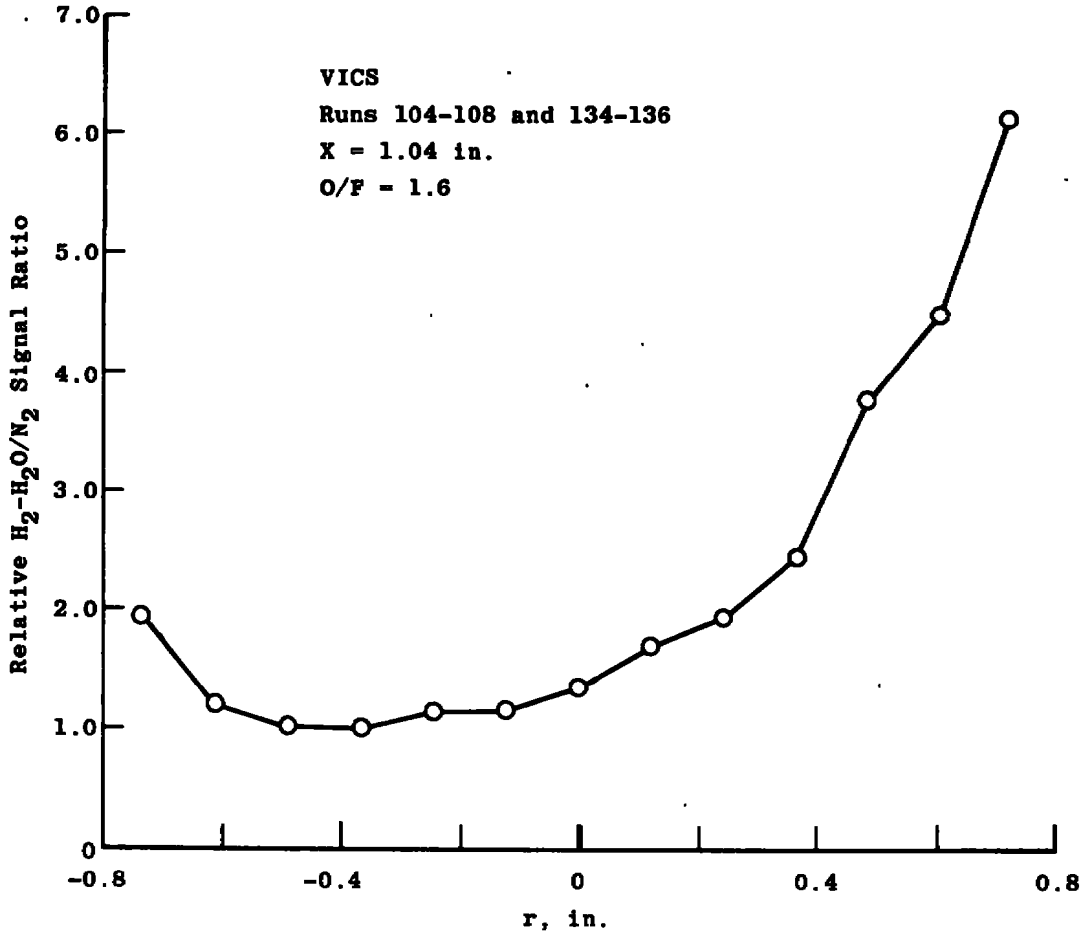

a. First determination

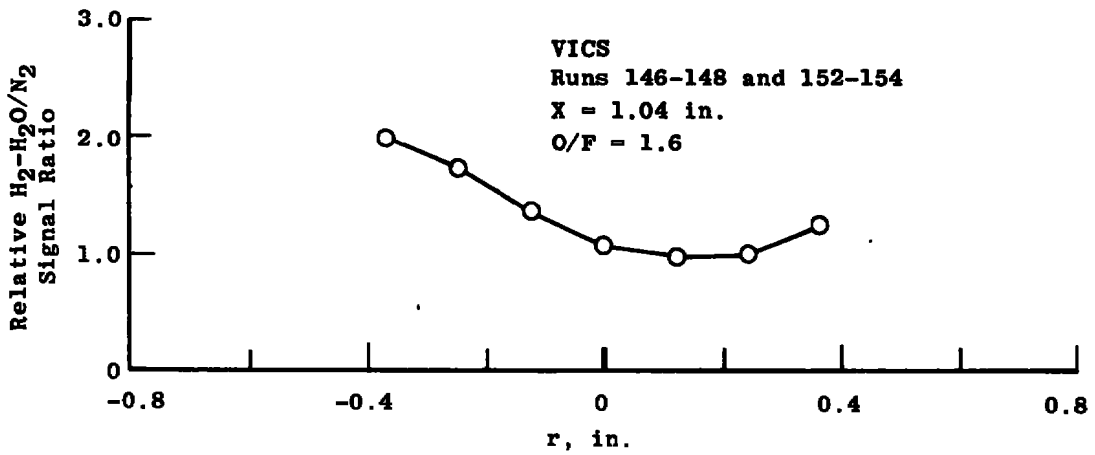

b. Second determination

Figure 46. VICS radial profiles of relative H_2 - H_2O/N_2 signal ratios in forward-flow region at O/F = 1.6.

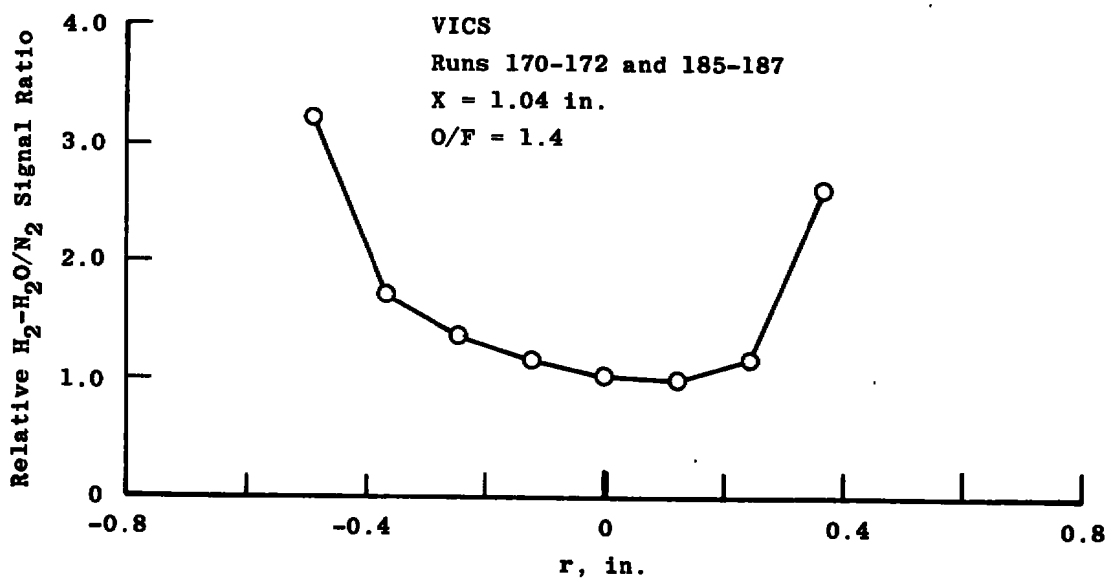

Figure 47. VICS radial profile of relative H_2 - H_2O/N_2 signal ratios in forward-flow region at O/F = 1.4.

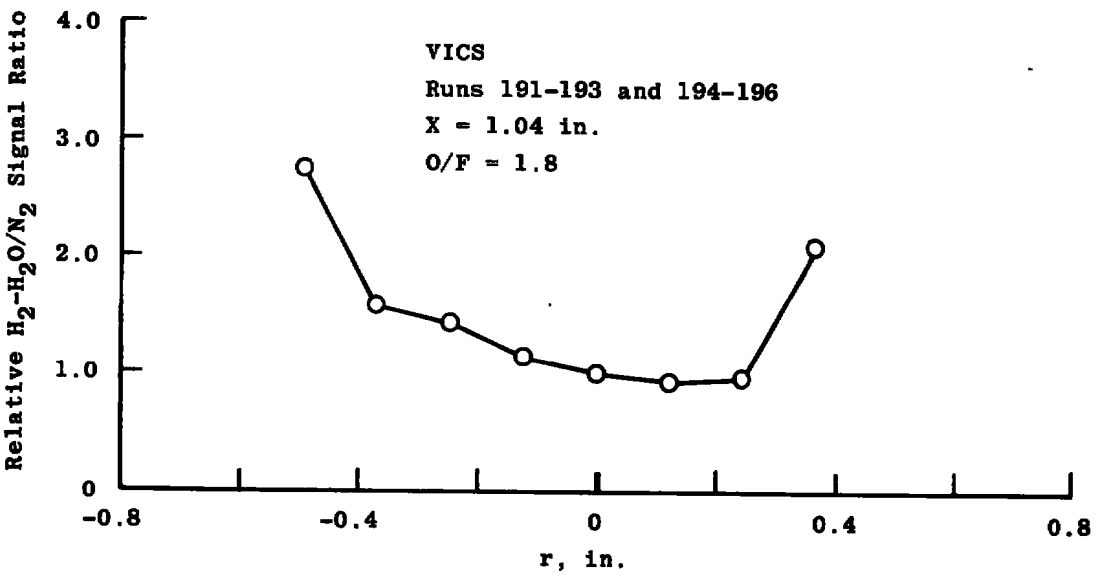

Figure 48. VICS radial profile of relative H_2 - H_2O/N_2 signal ratios in forward-flow region at O/F = 1.8.

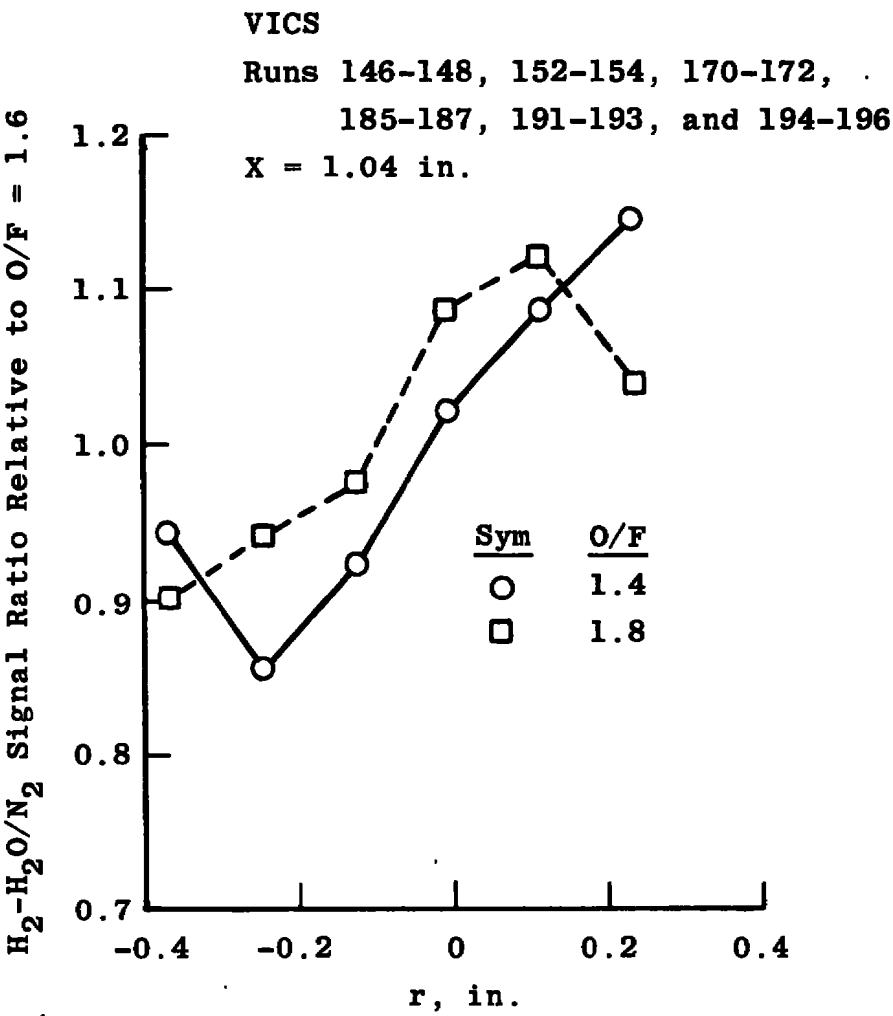

Figure 49. VICS radial profile of H_2 - H_2O/N_2 signal ratios relative to O/F = 1.6 in forward-flow region.

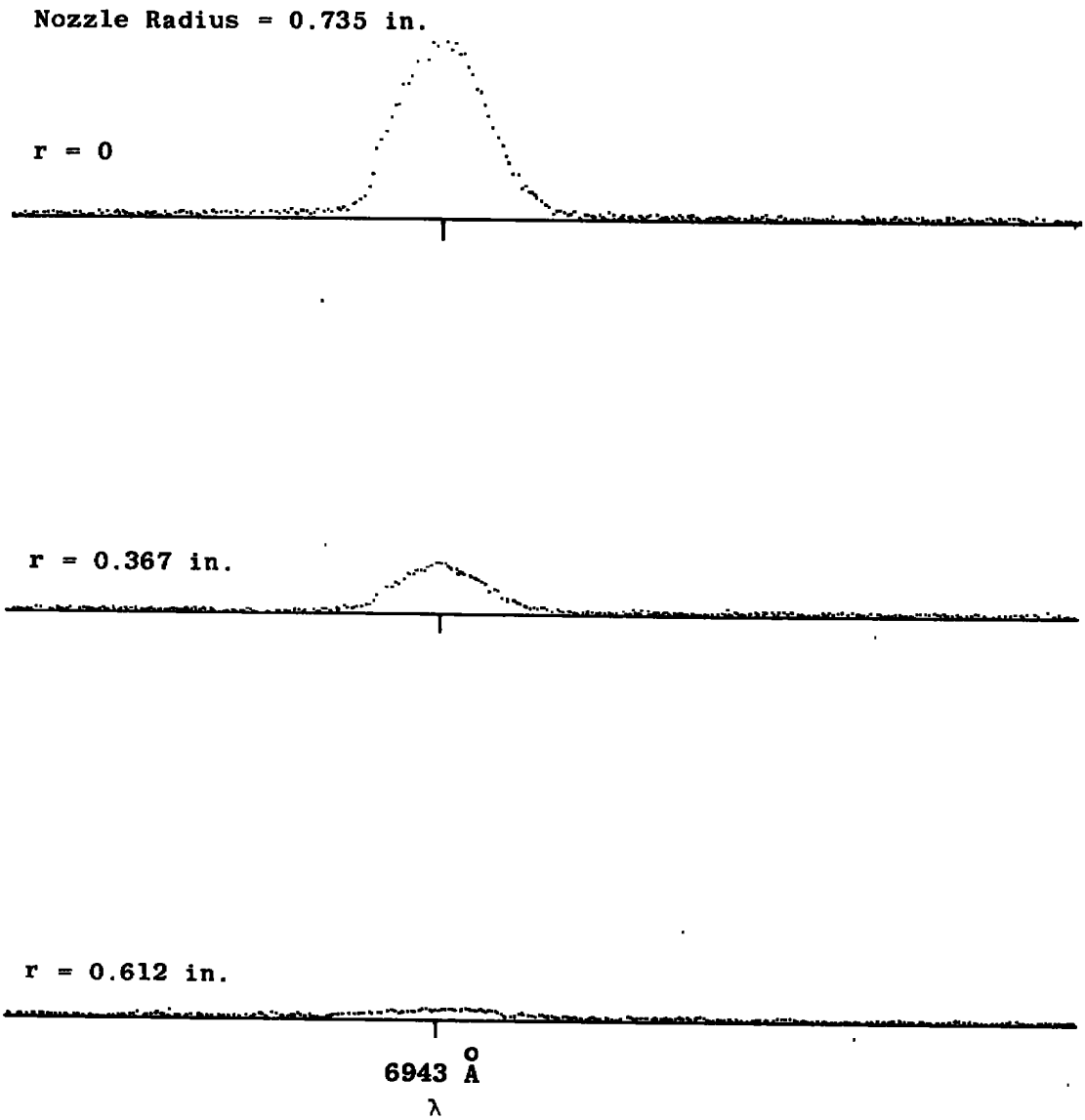

Figure 50. VICS laser scattering spectral intensity profile at three radial positions for a 100-msec engine pulse.

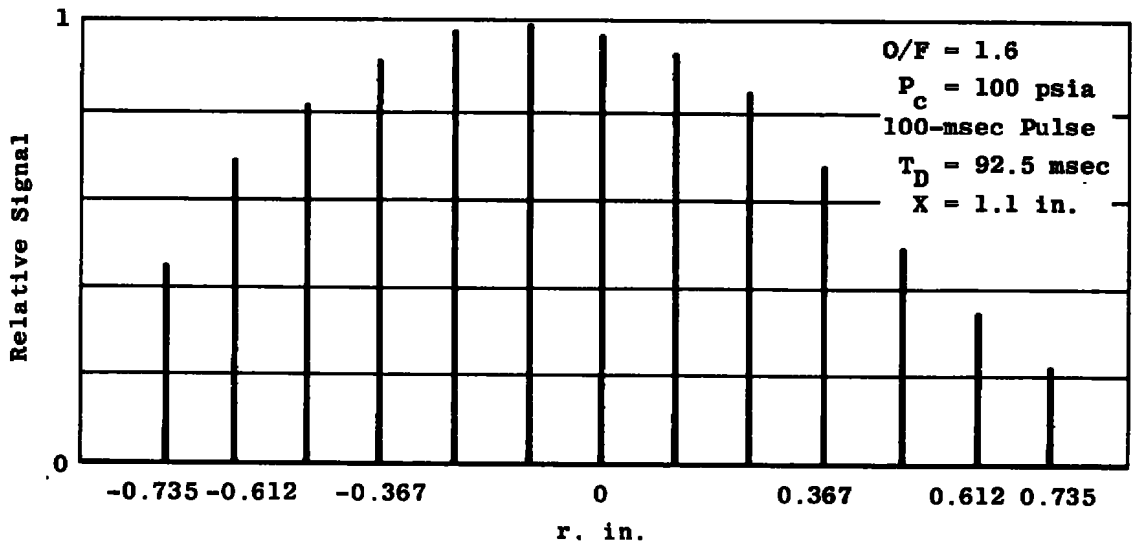

Figure 51. VICS laser scattering radial relative intensity profile before engine shutdown for a 100-msec engine pulse.

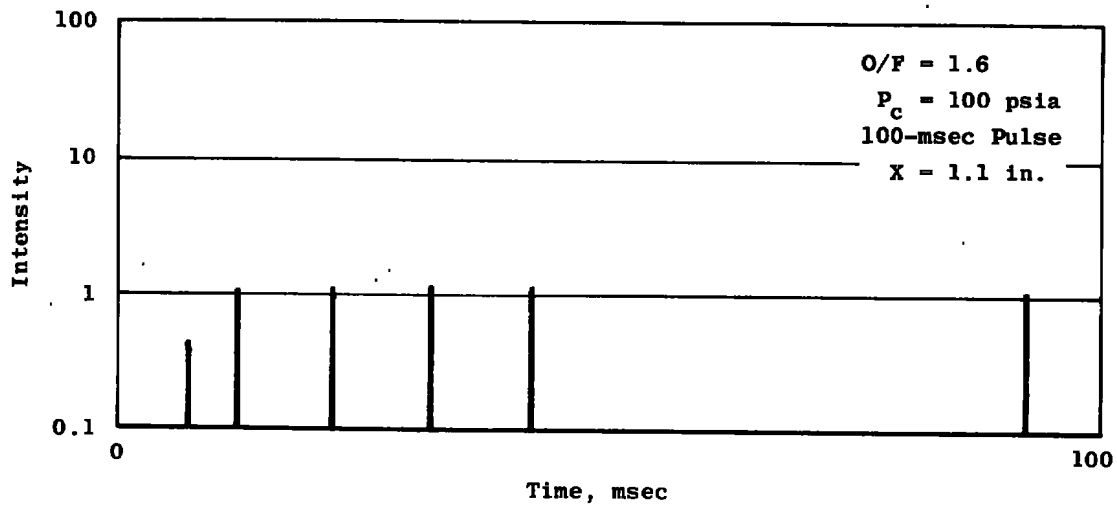

a. r = 0

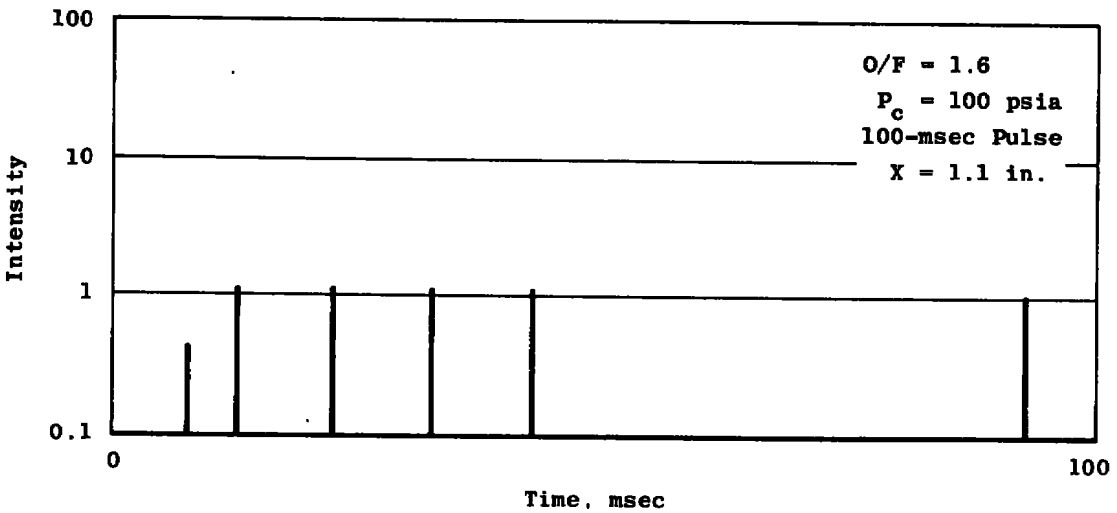

b. r = 0.1225 in.

Figure 52. VICS laser scattering temporal relative intensity profiles near axial centerline before engine shutdown for a 100 msec engine pulse.

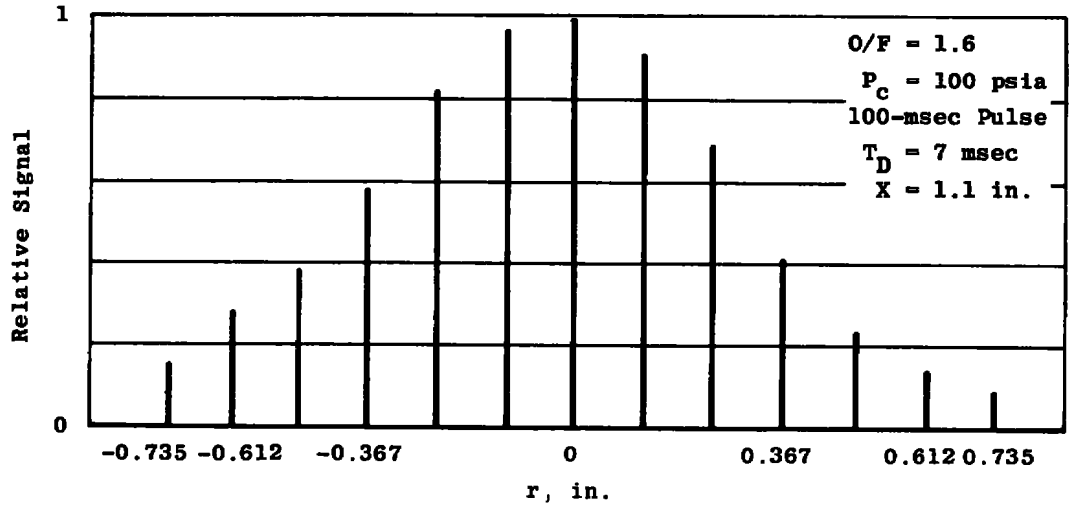

a. 7.0 msec

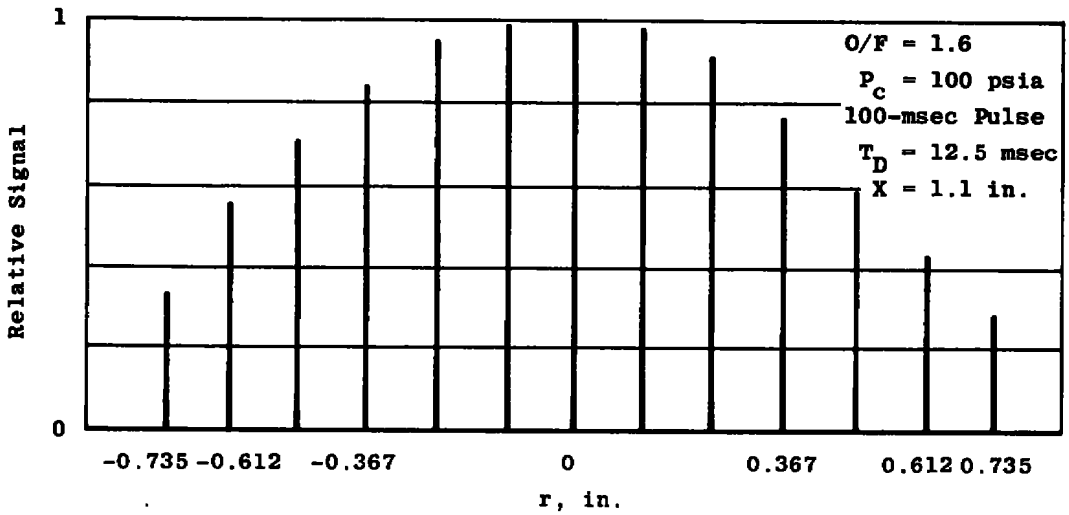

b. 12.5 msec

Figure 53. VICS laser scattering radial relative intensity profile at 7.0 and 12.5 msec after engine shutdown for a 100-msec engine pulse.

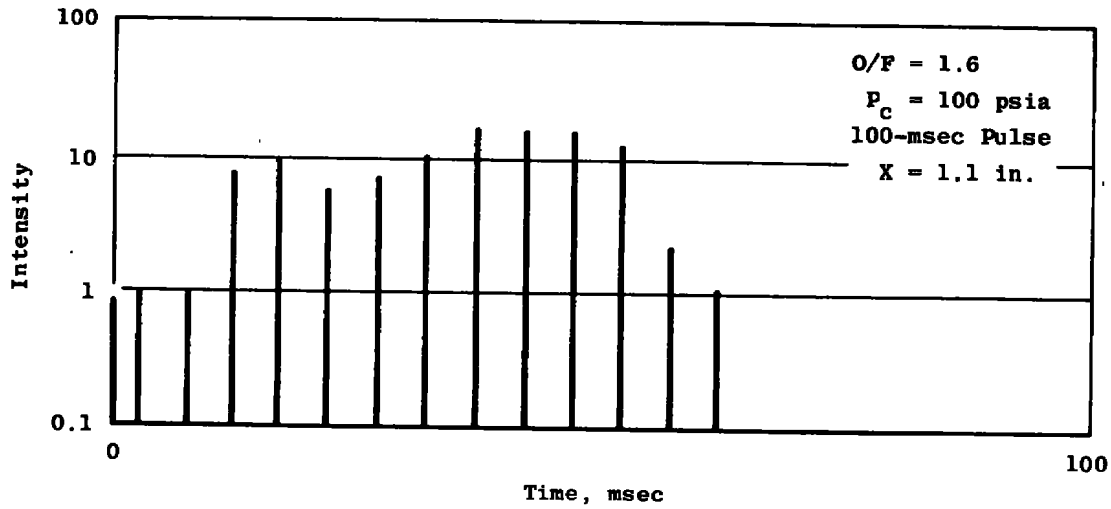

a. r = 0

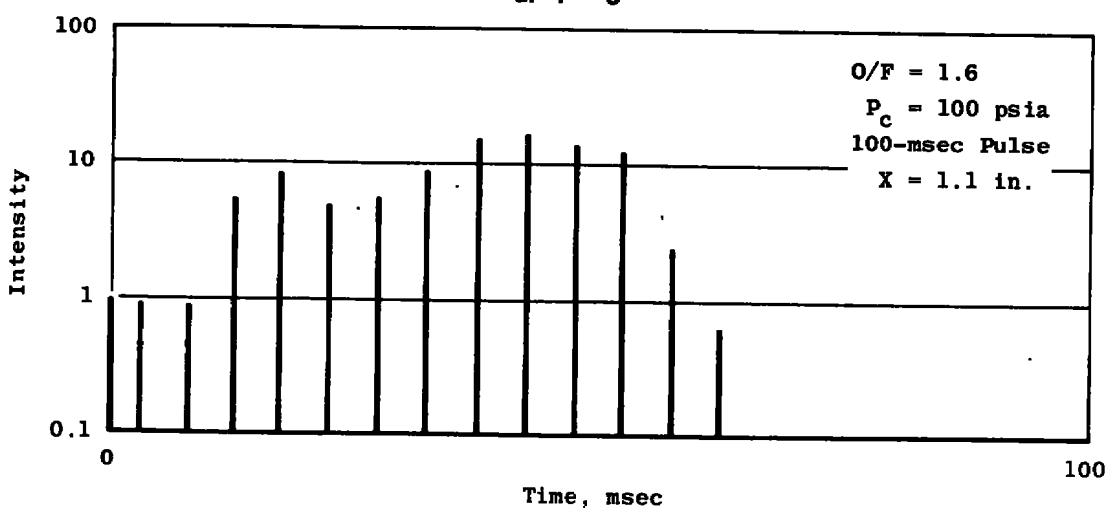

b. r = 0.1225 in.

Figure 54. VICS laser scattering temporal relative intensity profiles at five radial locations after engine shutdown for a 100-msec engine pulse.

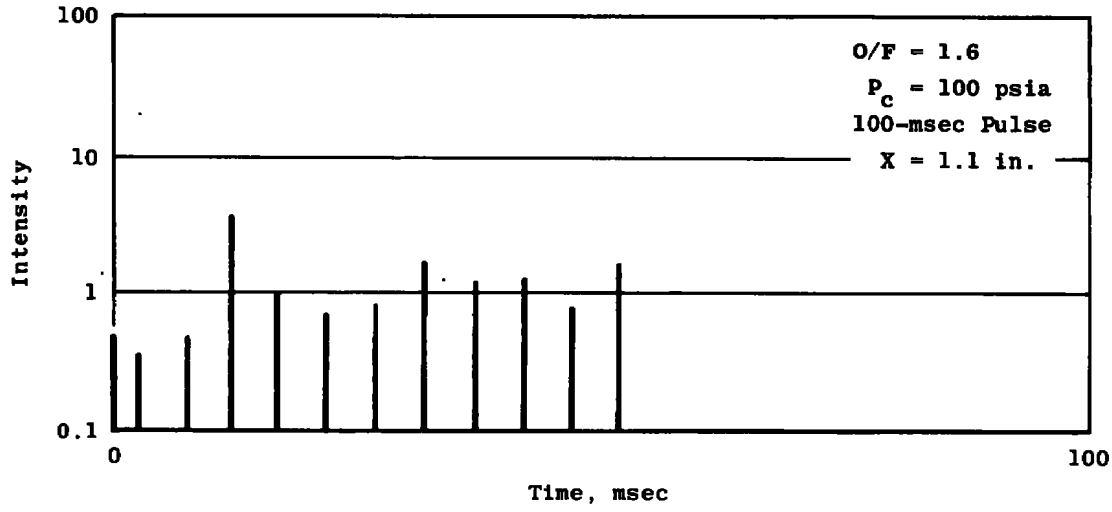

c. r = -0.735 in.

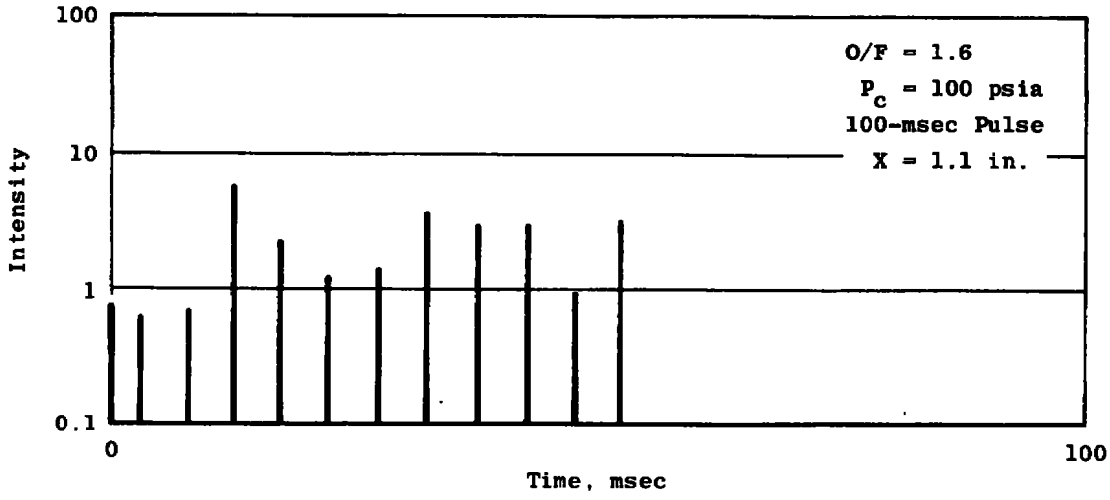

d. r = -0.6125 in.

Figure 54. Continued.

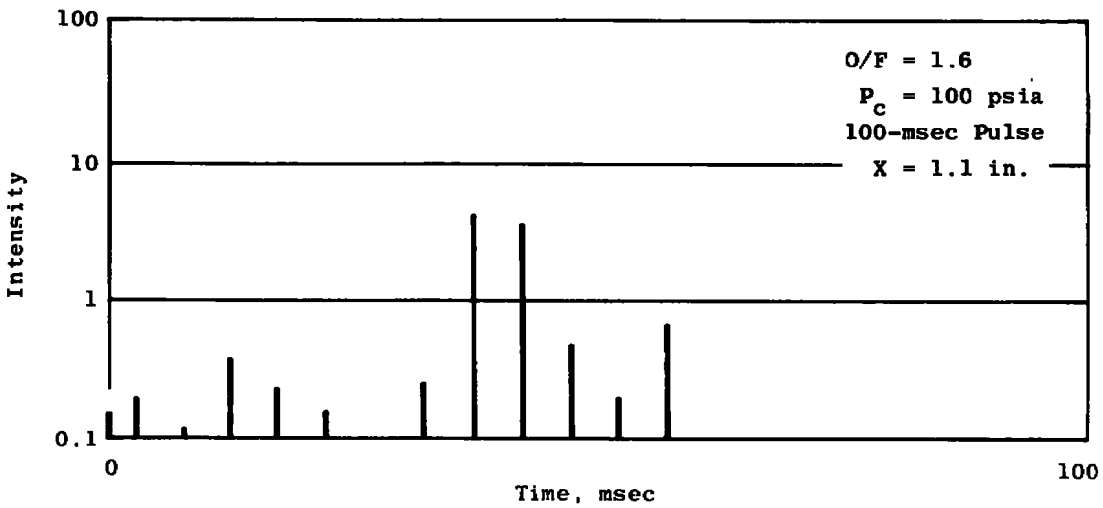

e. r = 0.6125 in.

Figure 54. Concluded.

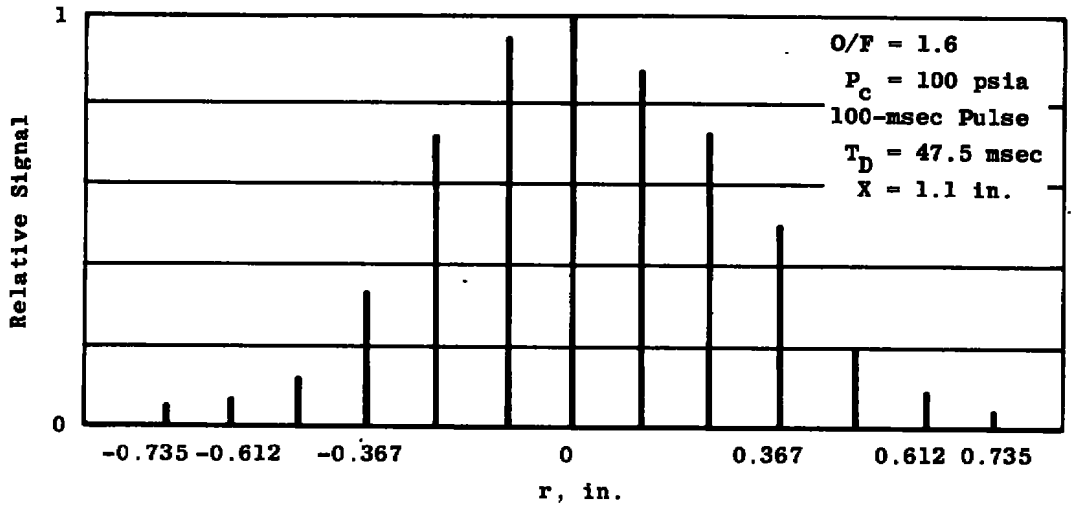

a. 47.5 msec

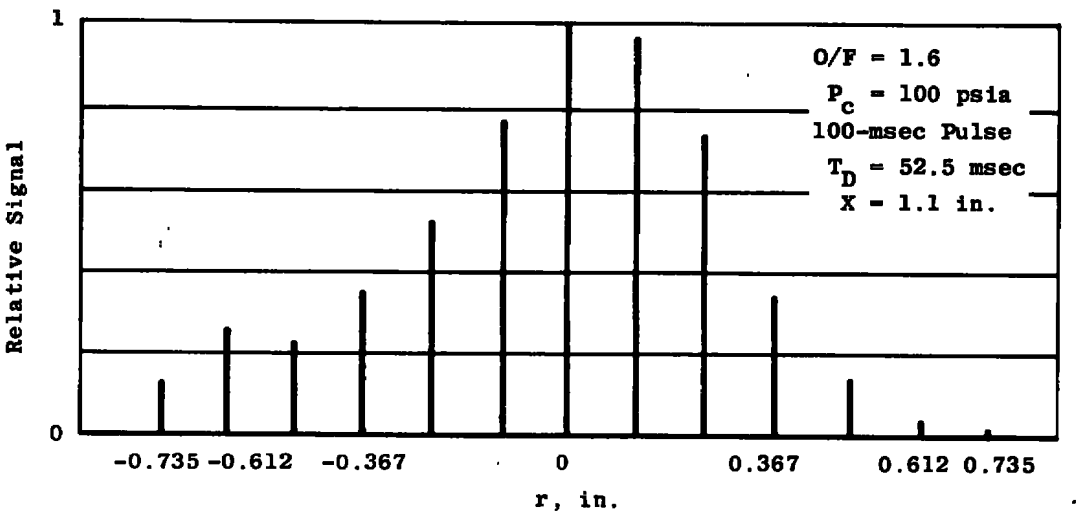

b. 52.5 msec

Figure 55. VICS laser scattering radial relative intensity profiles at engine shutdown and at times near the peak values for a 100-msec engine pulse.

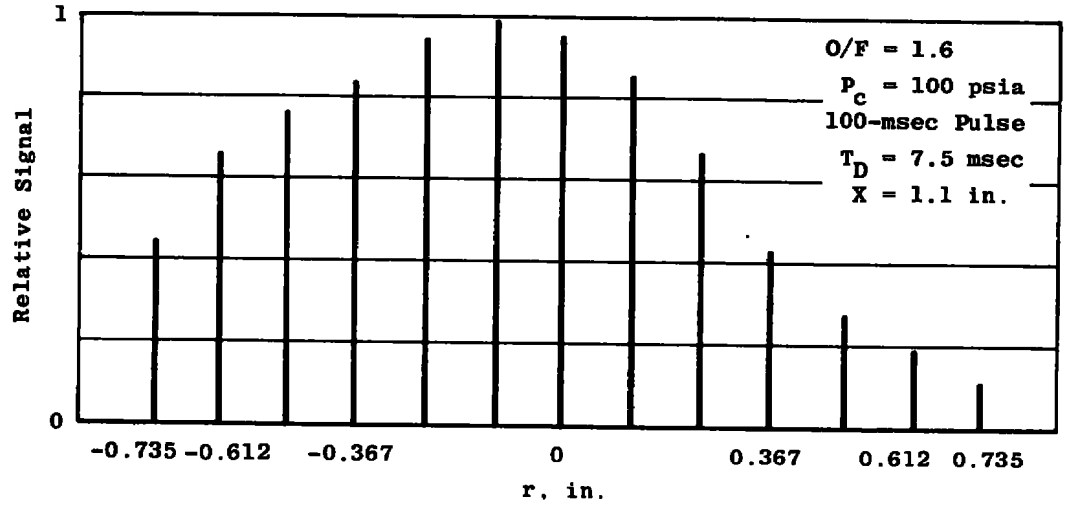

c. 7.5 msec

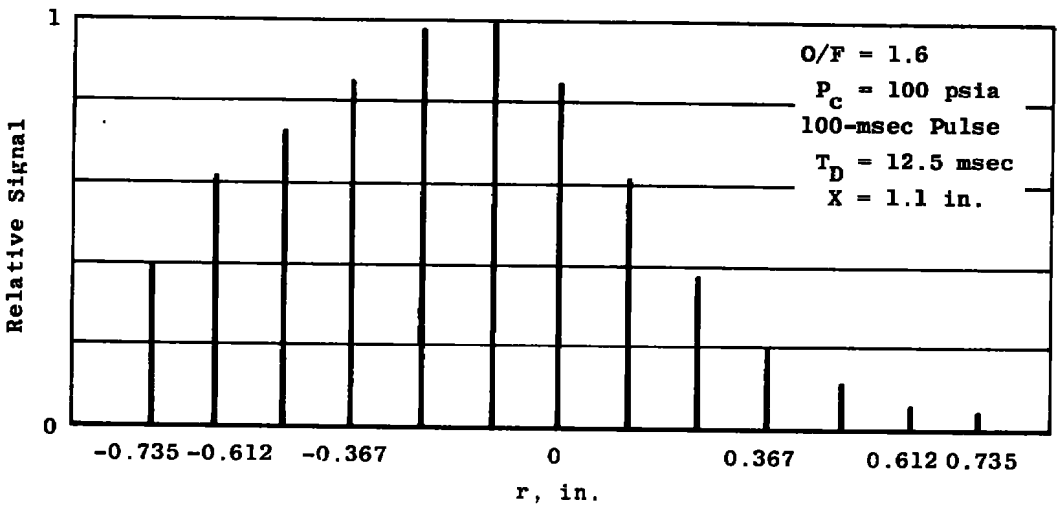

d. 12.5 msec

Figure 55. Continued.

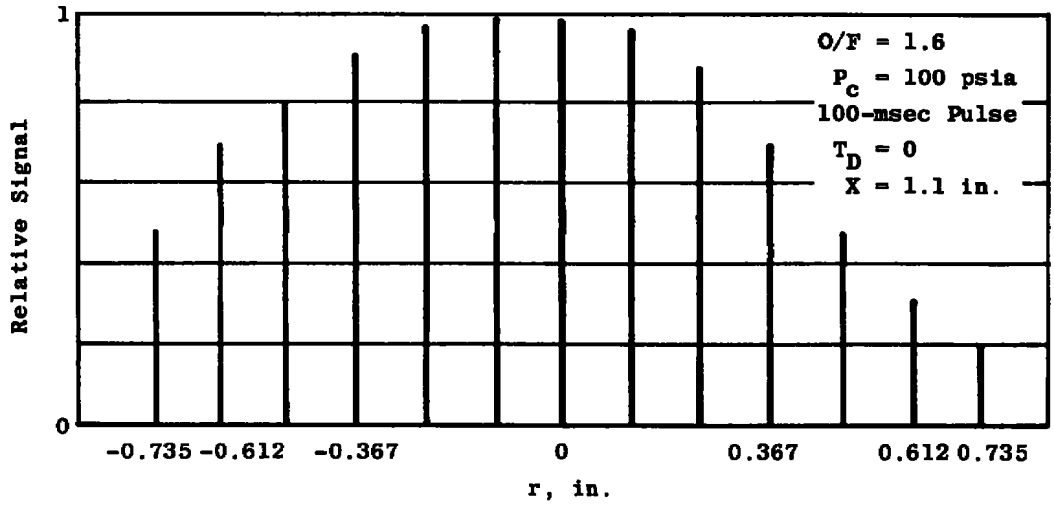

e. 0

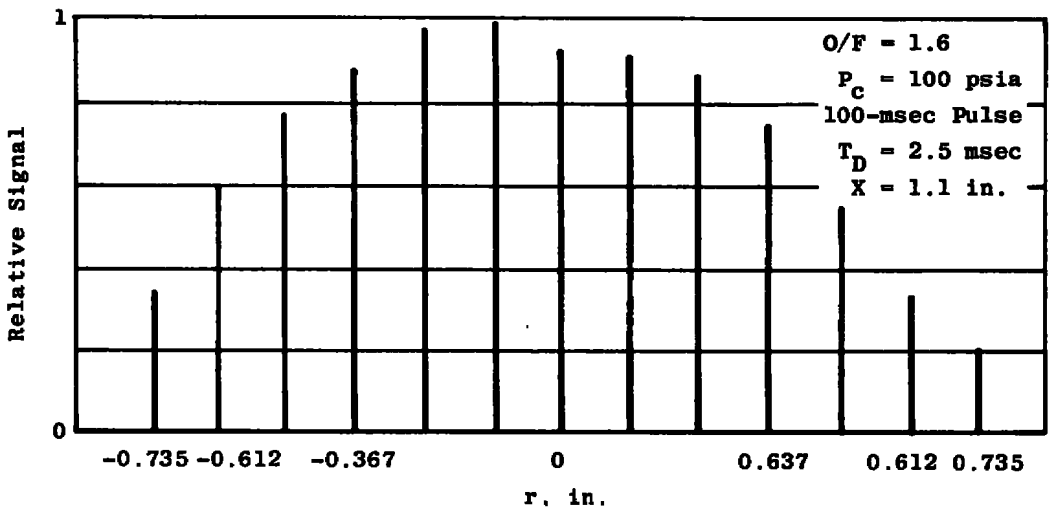

f. 2.5 msec

Figure 55. Concluded.

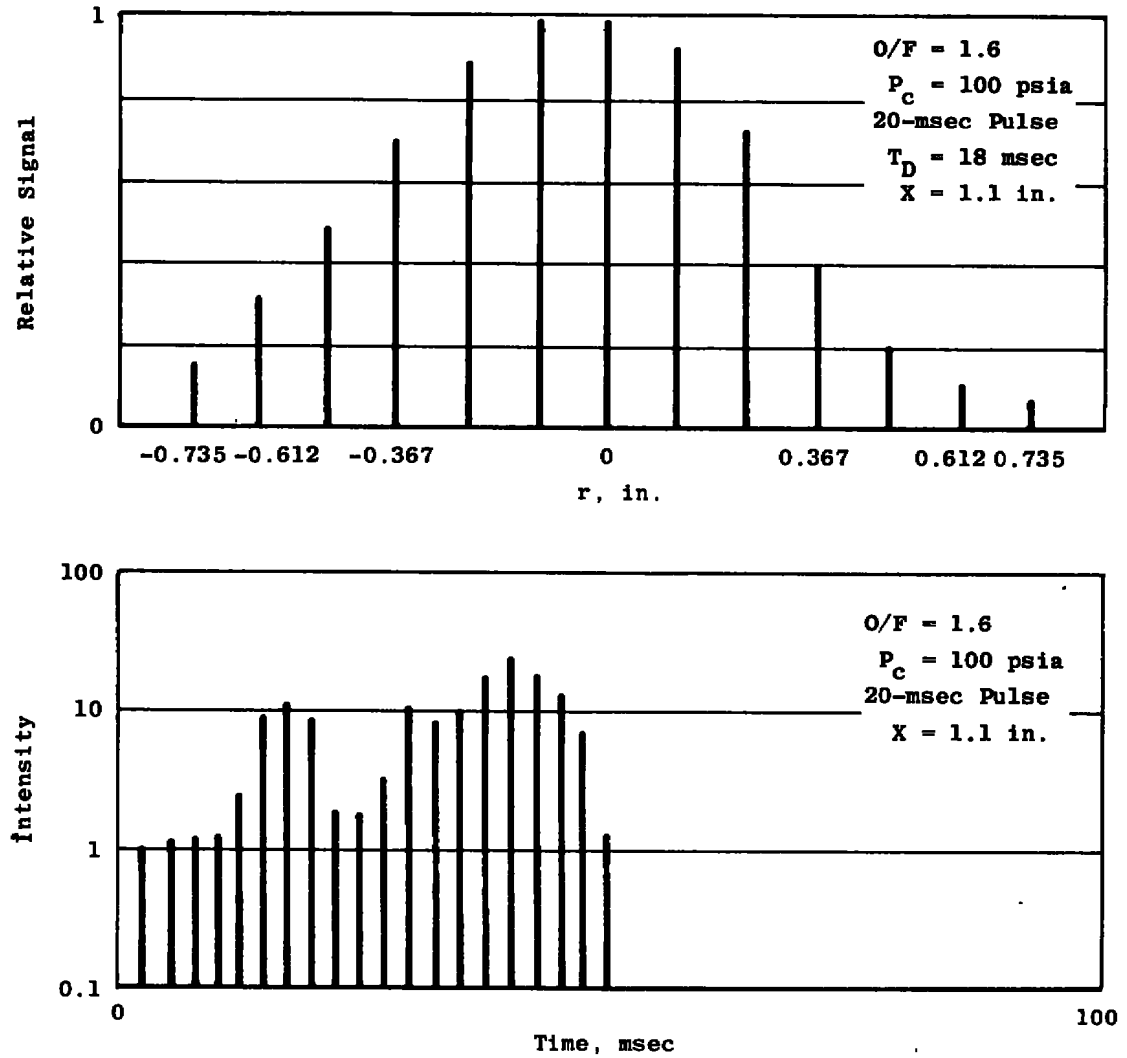

Figure 56. VICS laser scattering radial and temporal relative intensity profiles after engine shutdown for a 20-msec engine pulse.

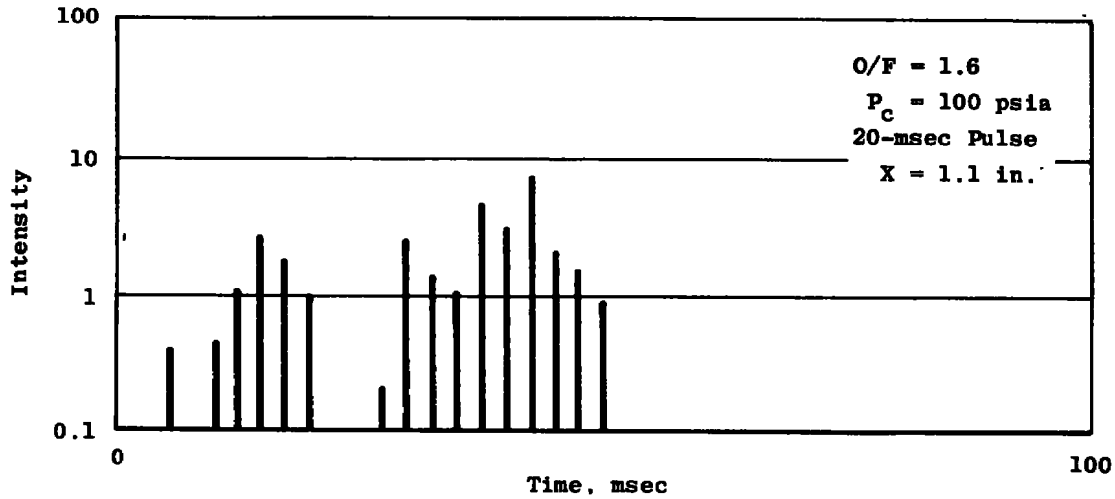

a. r = -0.735 in.

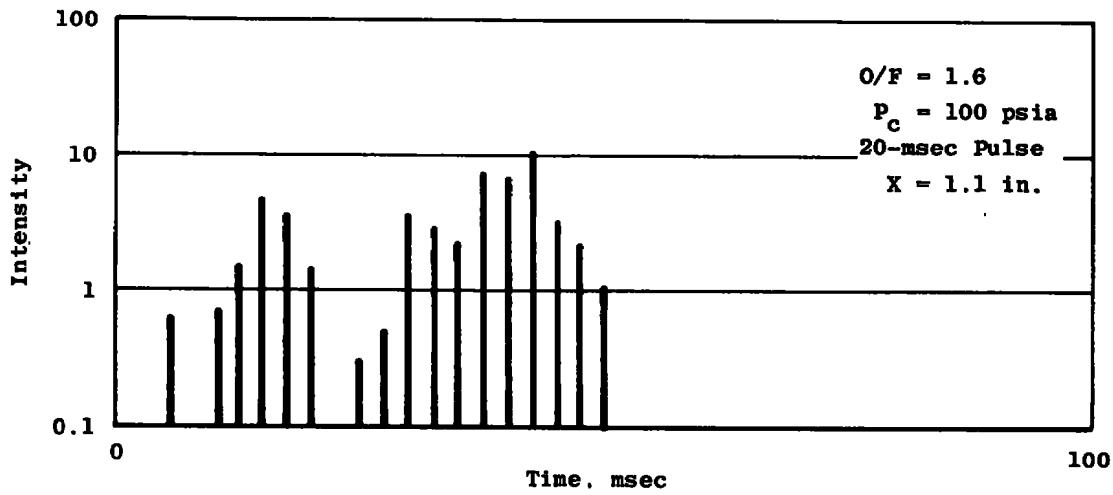

b. r = -0.6125 in.

Figure 57. VICS laser scattering temporal relative intensity profiles near the nozzle lips after engine shutdown for a 20-msec engine pulse.

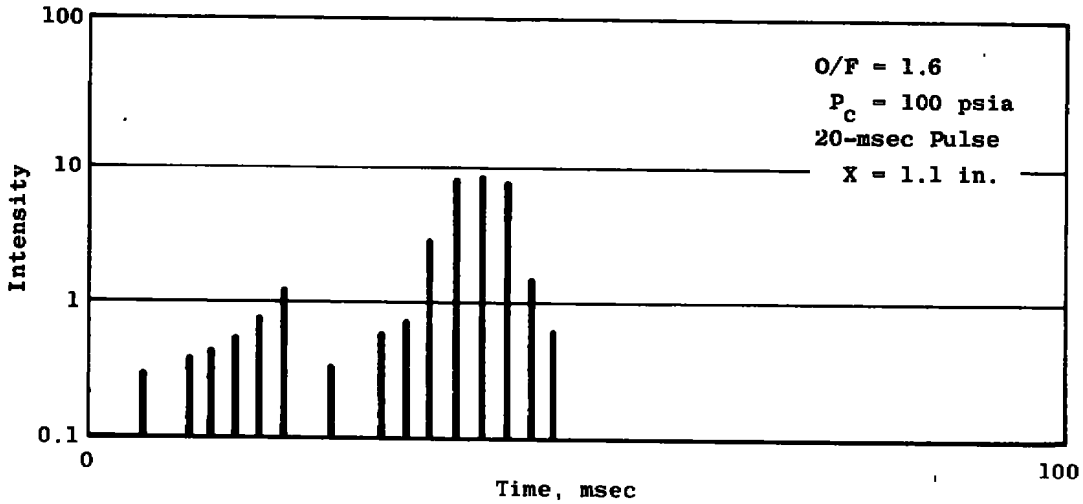

c. r = 0.735 in.

Figure 57. Concluded.

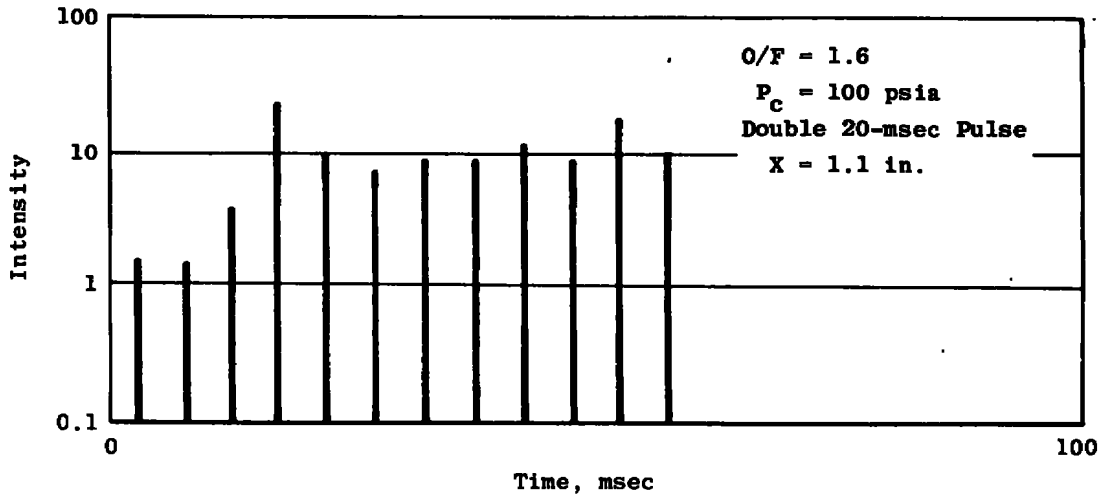

a. r = 0

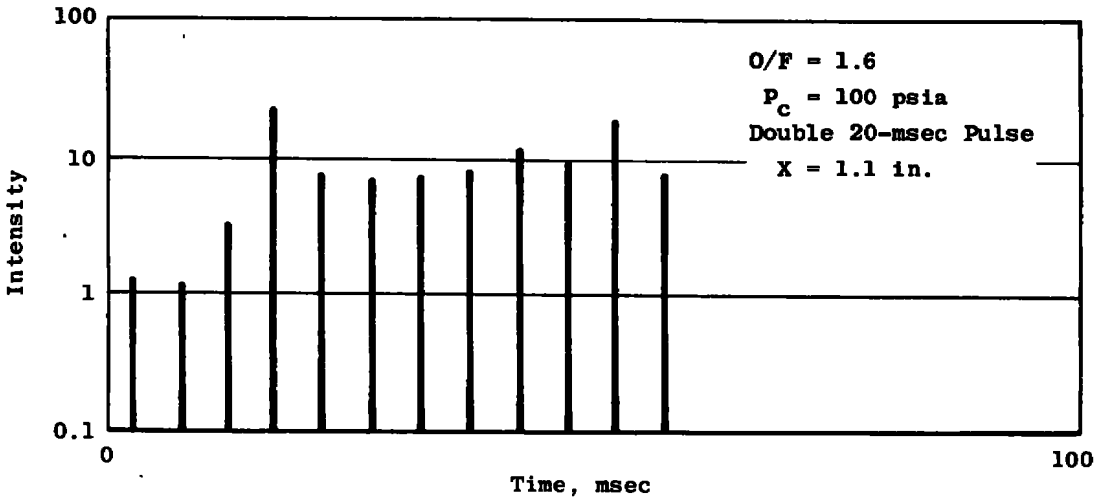

b. r = 0.1225 in.

Figure 58. VICS laser scattering temporal relative intensity profiles near axial centerline after engine shutdown for a double engine pulse.

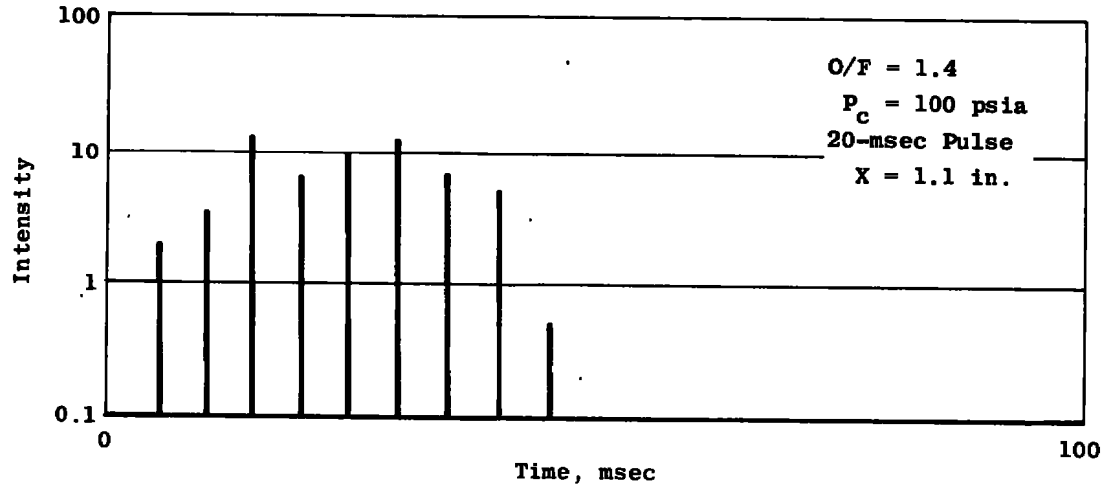

a. r = 0

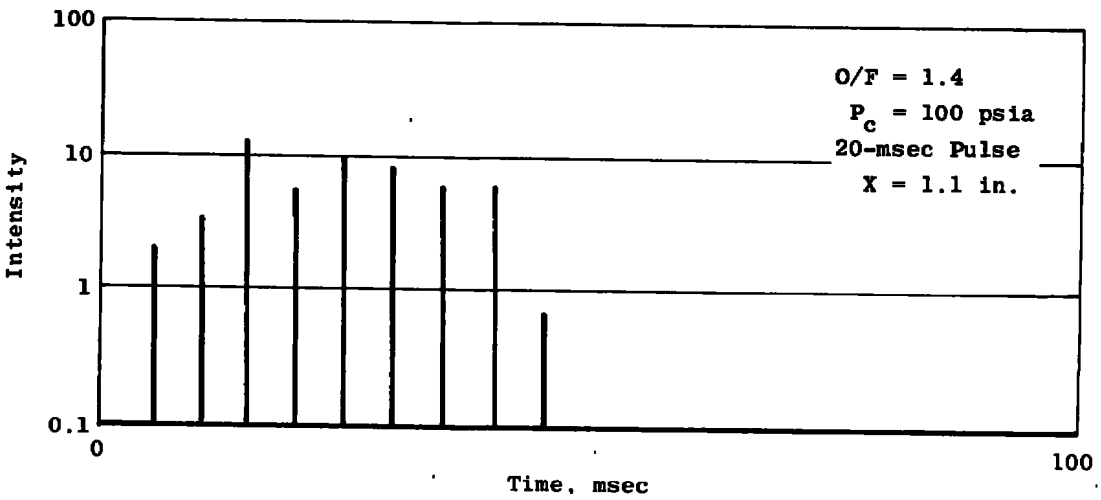

b. r = 0.1225 in.

Figure 59. VICS laser scattering temporal relative intensity profile near axial centerline after engine shutdown for a 20-msec engine pulse at O/F = 1.4 and 100 psia.

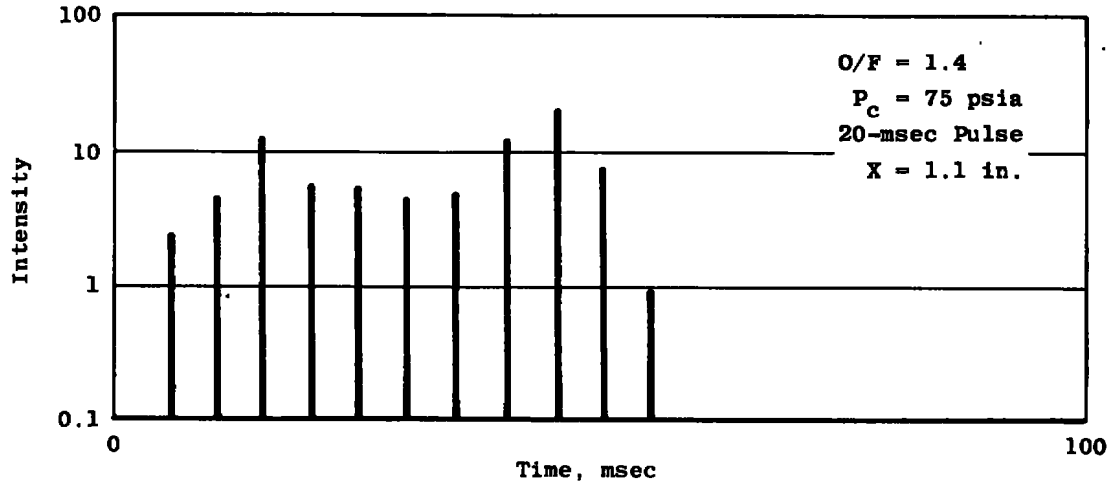

a. r = 0

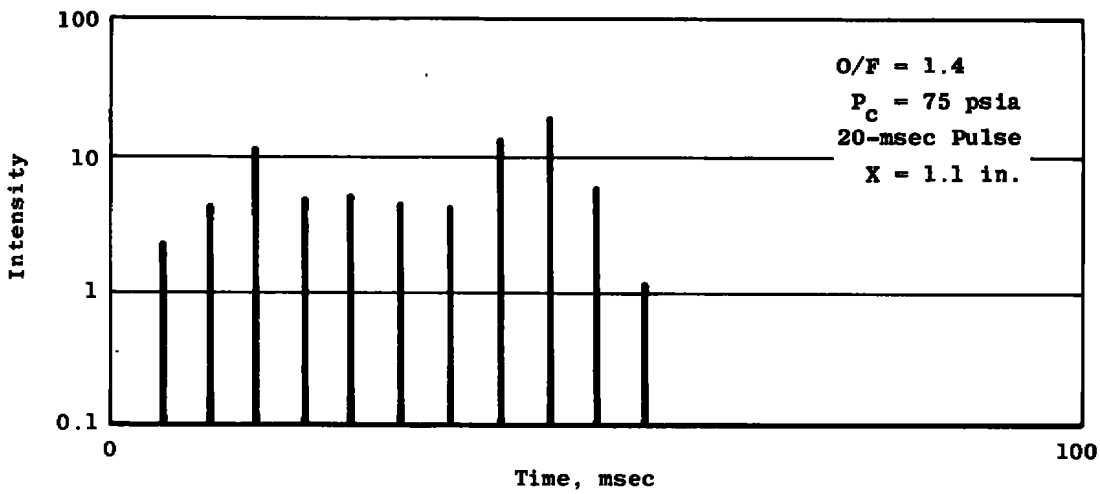

b. r = 0.1225 in.

Figure 60. VICS laser scattering temporal relative intensity profiles near axial centerline after engine shutdown for a 20-msec engine pulse at O/F = 1.4 and 75 psia.

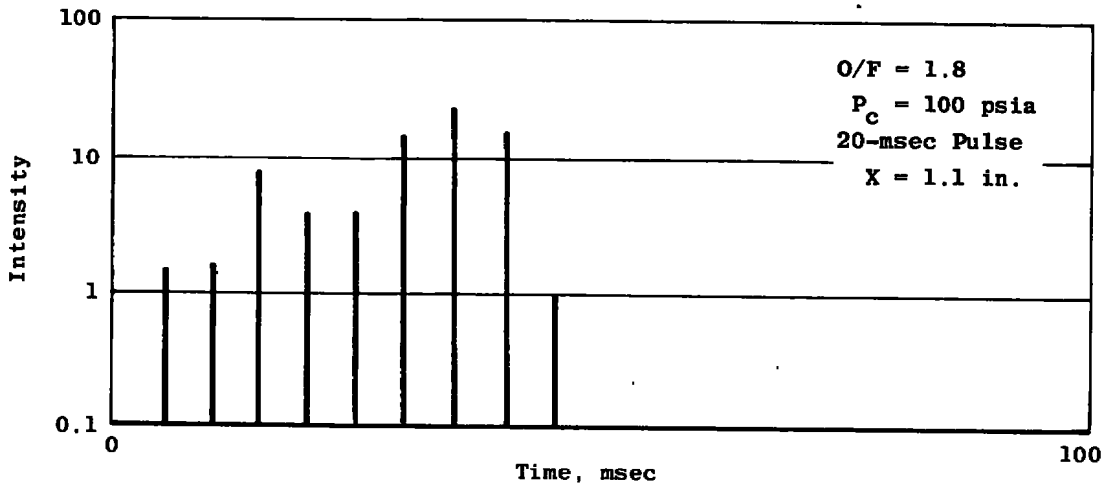

a. r = 0

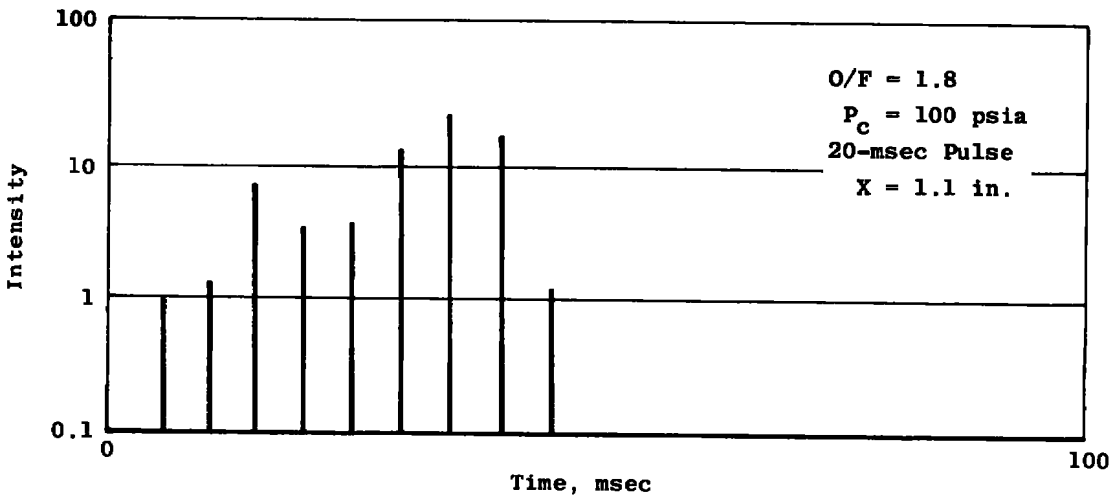

b. r = 0.1225 in.

Figure 61. VICS laser scattering temporal relative intensity profiles near axial centerline after engine shutdown for a 20-msec engine pulse at O/F = 1.8.

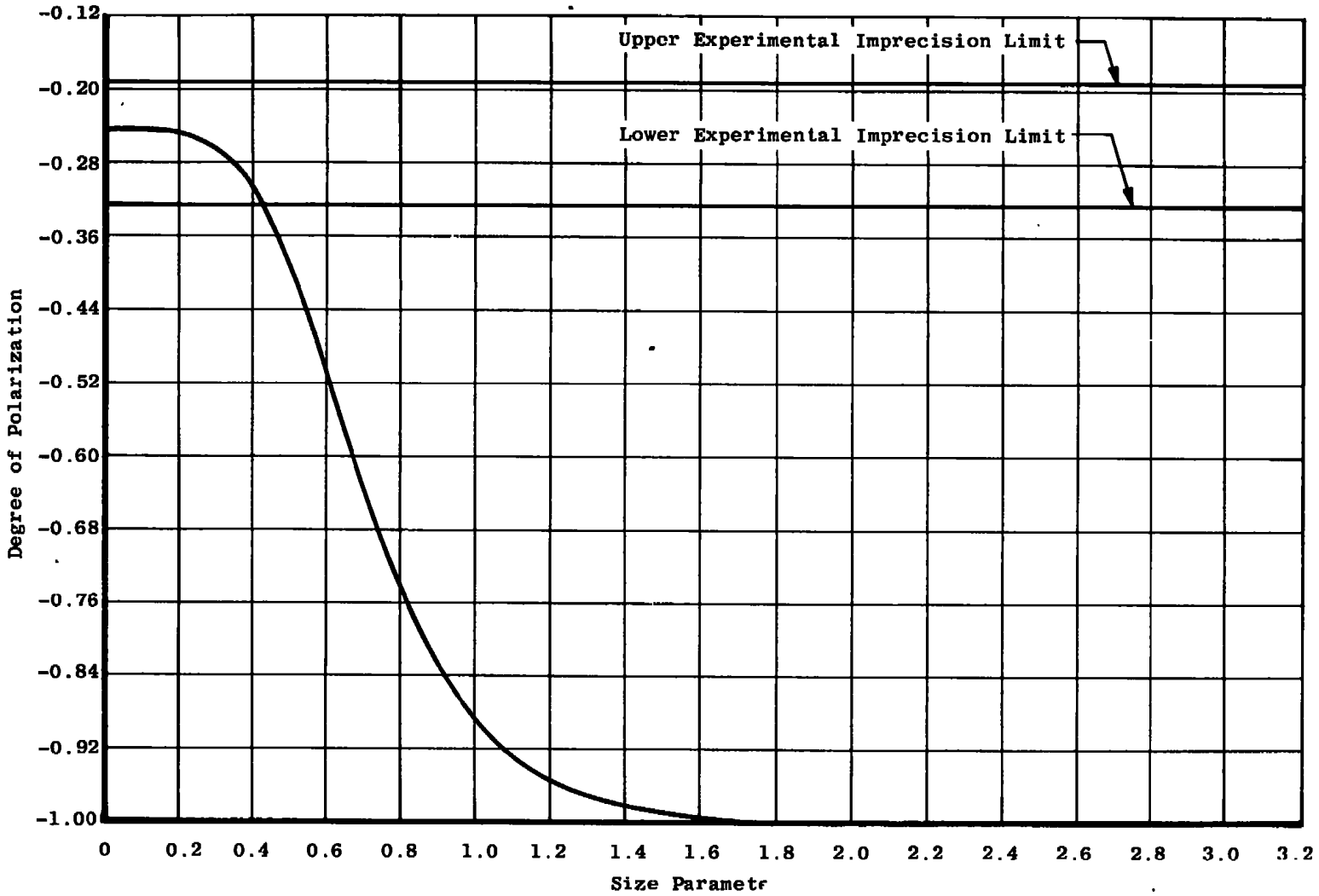

Figure 62. Size dependence of computed degree of polarization with superimposed experimental imprecision limits for data taken at 42.5 msec after shutdown.

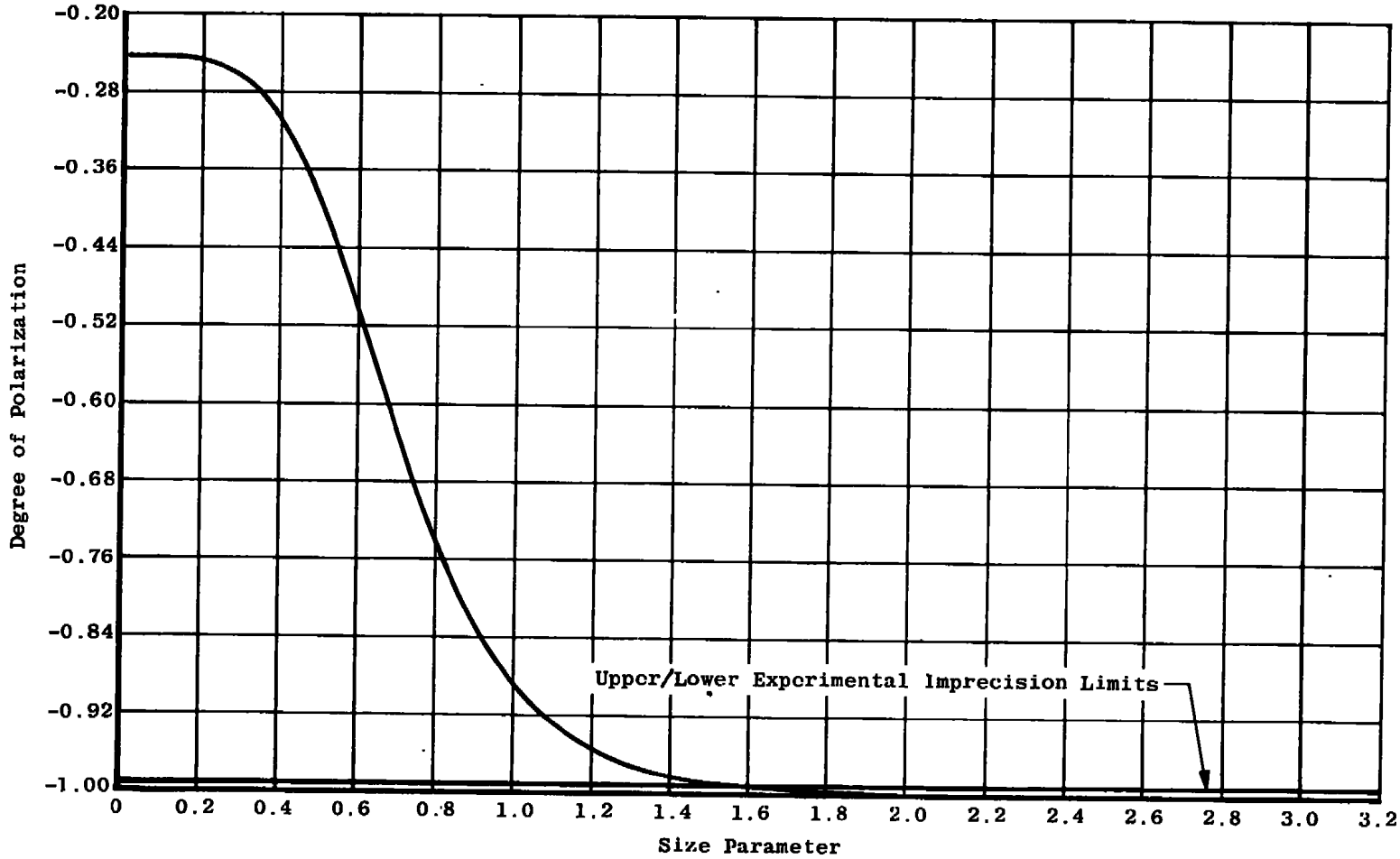

Figure 63. Size dependence of computed degree of polarization with superimposed experimental imprecision limits for data taken at 0.5 msec before shutdown.

NOMENCLATURE

Å	Angstrom unit, equal to 10^{-8} cm
A_e/A_t	Ratio of nozzle exit area to throat area
B	Bandshape factor, B_{cal}/B_{T_R}
B_{cal}	Relative intensity of N_2^+ band at sonic orifice T_R
B_{T_R}	Relative intensity of N_2^+ band at thruster T_R
C	Optical transmission and detection constant, wavelength dependent
C′	Measured count rate, counts/sec
C″	True count rate, counts/sec
C_{SO}	Sonic orifice calibration factor, counts/sec/cm^{-3}
CO^+ $A^2\Pi$	Excited electronic state of CO^+
$CO_2^+ X^2\Sigma$	Electronic ground state of CO^+
$CO_2^+ A^2\Pi$	Excited electronic state of CO_2^+
$CO_2^+ X^2\Pi$	Electronic ground state of CO_2^+
D	Diameter of spherical particle, cm
d	Effective width of electron beam at point of observation
E_B	Electron beam energy, kev
$\vec{E}_\parallel$, $\vec{E}_\perp$	Light wave electric vectors parallel and perpendicular to scattering plane, respectively
e^-_{py}, e^-_{sy}	Primary electron and secondary electron, respectively
f (x)	Particle size distribution normalized on interval $o \leq x \geq \infty$
g	Electronic ground state
h	Planck's constant
I	Electron beam current, ma
i j k l n t	Excited energy levels

k	Wave number of incident light equal to $2\pi/\lambda$, cm^{-1}
$k_{\alpha\mu}$ (i)	Quenching rate constant of level i of species α as a result of collisions with species μ, cm^3/sec/molecule
$\overline{k_7}$	Nitrogen quenching rate constant, cm^3/molecule
L	Length of electron beam observed, cm
L_i	Length of scattering volume viewed by the "i^{th}" detector
N_2 ($X^1\Sigma$)	Electronic ground state of N_2
N_2^+($X^2\Sigma$)	Electronic ground state of N_2^+
N_2^+($B^2\Sigma$)	Excited electronic state of N_2^+
n	True number density, cm^{-3}
N_i	Number density of aerosols in the scattering volume viewed by the "i^{th}" detector
n_T	Total number density, cm^{-3}
n_{NQ}	Number density of N_2 uncorrected for quenching, cm^{-3}
$n_\alpha(g)$	Number density of ground state g of species α, cm^{-3}
O/F	Oxidizer - fuel ratio
$P(\theta_i, \phi_i)$	Degree of polarization of the scattered light observed by the "i^{th}" detector
P_c	Engine combustion chamber pressure, psia
P_o	Sonic orifice reservoir pressure, psia
r	Radial distance from axial centerline, in.
$S_\alpha(ij)$	Photon emission rate for the i to j transition of species α, photons/sec
$S^o_\alpha(ij)$	Photon emission rate for the i to j transition of species α where collisional quenching is negligible, photons/sec
T_o	Sonic orifice reservoir temperature, °K
T_D	Location of data gate with respect to reference time, msec
T_R	Rotational temperature, °K

t	Time, sec
X(K),Y(K)	Parameters of rotational lines of quantum number K
X	Axial distance from nozzle exit plane, in.
x	Particle size parameter, equal to $\pi D/\lambda$
X/D	Axial distance from sonic orifice divided by orifice diameter
Y	Vertical distance from nozzle axial centerline, in.
$\beta_\alpha(ij)$	Branching factor for the i to j transition of species α
$\Delta\theta_i$	Range of scattering angles subtended by the "i^{th}" detector
$\Delta\phi_i$	Range of azimuths subtended by the "i^{th}" detector
$\Delta\Omega$	Solid angle subtended by the detector at the point of observation, sr
η	Index of refraction
θ_i	Polar scattering angle corresponding to the "i^{th}" detector location
θ_S	Electron beam sweep angle
λ	Wavelength
$\lambda_\alpha(ij)$	Wavelength for the i to j transition of species α, nm
ν	Light frequency, Hz
$\sigma_\alpha(gi)$	Excitation cross section from ground state g to exicted state i of species α, cm^2
τ_{DT}	Dead time of detector electronics, sec
$\tau_\alpha(i)$	Lifetime of excited state i of species α
$\Phi_j(\theta_i,\phi_i)$	Scattered light flux intercepted by the "i^{th}" detector with the "j^{th}" polarization state
ϕ_i	Azimuthal angle corresponding to the "i^{th}" detector location (measured from the direction of the incident laser electric field to the scattering plane)